ROADMAP • **OPEN ACCESS**

The Roadmap for runaway electron-induced plasma facing component damage in tokamaks

Plasma Physics and Controlled Fusion

OPEN ACCESS

RECEIVED
11 June 2025

REVISED
2 October 2025

ACCEPTED FOR PUBLICATION
6 November 2025

PUBLISHED
11 June 2026

ROADMAP

The Roadmap for runaway electron-induced plasma facing component damage in tokamaks

S Ratynskaia[1,*], M Hoelzl[2], E Nardon[3], P Aleynikov[2], F J Artola[4], V Bandaru[5], M Beidler[6], B Breizman[7], D del-Castillo-Negrete[7], M De Angeli[8], V Dimitriou[9], R Ding[10], J Eriksson[11], O Ficker[12], R S Granetz[13], E Hollmann[14], M Hoppe[1], M Houry[3], I Jepu[15], H R Koslowski[16], C Liu[17], J R Martin-Solis[18], G Pautasso[2], Y Peneliau[3], R A Pitts[4], G I Pokol[19], C Reux[3], U Sheikh[20], S A Silburn[15], T Tang[10], R A Tinguely[13], P Tolias[1], E Tomesova[12] and R Villari[21]

[1] KTH Royal Institute of Technology, Stockholm SE-100 44, Sweden
[2] Max Planck Institute for Plasma Physics, Garching b. M. and Greifswald, Germany
[3] CEA, IRFM, F-13108 Saint-Paul-lez-Durance, France
[4] ITER Organization, Saint Paul Lez Durance Cedex, France
[5] Department of Mechanical Engineering, Indian Institute of Technology Guwahati, Guwahati, Assam, India
[6] Fusion Energy Division, Oak Ridge National Laboratory, Oak Ridge, TN 37831, United States of America
[7] Institute for Fusion Studies, The University of Texas at Austin, Austin, TX, United States of America
[8] Institute for Plasma Science and Technology—CNR, Milan, Italy
[9] Institute of Plasma Physics and Lasers—IPPL, University Research and Innovation Centre, Hellenic Mediterranean University, Rethymno GR-74150, Greece
[10] Institute of Plasma Physics, HFIPS, Chinese Academy of Sciences, Hefei 230031, People's Republic of China
[11] Department of Physics and Astronomy, Uppsala University, SE-75237 Uppsala, Sweden
[12] Institute of Plasma Physics of the CAS, CZ-18200 Praha 8, Czech Republic
[13] Plasma Science and Fusion Center, Massachusetts Institute of Technology, Cambridge, MA, United States of America
[14] University of California—San Diego, San Diego, CA 92093, United States of America
[15] UKAEA, Culham Campus, Abingdon OX14 3DB, United Kingdom
[16] Forschungszentrum Jülich GmbH, Institute of Fusion Energy and Nuclear Waste Management—Plasma Physics, 52425 Jülich, Germany
[17] State Key Laboratory of Nuclear Physics and Technology, School of Physics, Peking University, Beijing 100871, People's Republic of China
[18] Universidad Carlos III de Madrid, Avenida de la Universidad 30, 28911 Madrid, Spain
[19] Department of Nuclear Techniques, Budapest University of Technology and Economics, 1111 Budapest, Hungary
[20] Swiss Plasma Center (SPC), Ecole Polytechnique Federale de Lausanne (EPFL), CH-1015 Lausanne, Switzerland
[21] ENEA, Department of Fusion and Technology for Nuclear Safety and Security, Frascati (Rome), Italy
[*] Author to whom any correspondence should be addressed.

E-mail: srat@kth.se, matthias.hoelzl@ipp.mpg.de and eric.nardon@cea.fr

Keywords: runaway electrons (REs), PFC damage, thermomechanical response of PFCs

Abstract

This Roadmap article addresses the critical and multifaceted challenge of plasma-facing component (PFC) damage caused by runaway electrons (REs) in tokamaks, a phenomenon that poses a significant threat to the viability and longevity of future fusion reactors such as ITER and DEMO. The dramatically increased RE production expected in future high-current tokamaks makes it very difficult to avoid or mitigate REs in such devices when a plasma discharge terminates abnormally. Preventing damage from the intense localized heat loads they can cause requires a holistic approach that considers plasma, REs and PFC damage. Despite decades of progress in understanding the physics of REs and the thermomechanical response of PFCs separately, their complex interplay remains poorly understood. This document aims to initiate a coordinated, interdisciplinary approach to bridge this gap by reviewing experimental evidence, advancing diagnostic capabilities, and improving modeling tools across different scales, dimensionalities, and fidelities. Key topics include RE beam formation and transport, damage mechanisms in both brittle and metallic PFCs, and observed effects in major facilities such as JET, DIII-D, WEST and EAST. The Roadmap emphasizes the urgency of predictive, high-fidelity modeling validated against well-diagnosed controlled experiments, particularly in the light of recent changes in ITER's wall material strategy and the growing importance of private sector fusion initiatives. The modeling gaps include calculations of the magnetic equilibrium, RE distribution function and background plasma properties at

the start of the beam termination, with a critical need to advance modeling of access conditions to benign terminations. This is to be followed by simulations of the termination itself which requires a self-consistent description of the 3D MHD fields together with the REs, which is now available thanks to recent developments. Finally, the damage assessment is enabled by modeling of the full thermo-mechanical response, encompassing the hydrodynamic and the deviatoric behavior, to RE impacts with characteristics as provided by the termination simulations. The full workflow is computationally heavy for scoping studies to assist design of future machines, calling for development of reduced or surrogate models. Each section of the Roadmap article is written to provide a concise overview of one area of this multidisciplinary subject, with an assessment of the status, a look at current and future challenges, and a brief summary. The ultimate goal of this initiative is to guide future mitigation strategies and design resilient components that can withstand the intense localized loads imposed by REs, thus ensuring the safe and sustainable operation of the next generation of fusion power plants.

Contents

1. Introduction

S Ratynskaia[1], M Hoelzl[2] and E Nardon[3]

[1] KTH Royal Institute of Technology, Stockholm SE-100 44, Sweden
[2] Max Planck Institute for Plasma Physics, Boltzmannstr. 2, 85748 Garching b. M, Germany
[3] IRFM, CEA Cadarache, F-13108 Saint-Paul-lez-Durance, France

Back in 2001, a comprehensive review on plasma–wall interactions by Gianfranco Federici and coworkers pointed out that [1]: 'Although in recent years significant progress has been made in characterizing runaway electrons (REs) generation, there are still uncertainties in the quantification of material damage'. More than twenty years later, the latter remains valid: RE induced damage on plasma facing components (PFCs) is still insufficiently understood. Meanwhile, the topics of RE generation & transport and thermomechanical PFC response have independently matured to a large degree. The ambition of the present Roadmap is to initiate a coordination between the practitioners in these two distinct topics that will lead to a deeper understanding of the complex physics and multi-faceted consequences of RE impacts on PFCs.

Importance and timeliness

Recent years have seen dramatic growth in privately funded fusion companies. Long-awaited breakthroughs concerning ignition (NIF-USA) [5] and fusion energy produced (JET-EUROfusion) [6] made headlines, attracting even more capital to an already multi-billion dollar industry [7]. Transition from experimental facilities to commercial power plants involves the upgrade from short pulses to long plasma operation, which is only viable if the vessel power handling capability is not compromised. In the most technologically mature magnetic confinement concept of tokamaks, the provision of PFCs with sufficient lifetime is one of the major technological obstacles to be overcome [8, 9]. This issue is central to the construction of the ITER reactor and the engineering design of the DEMO power plant. Besides enhanced energy efficiency and favorable plasma operations, extended PFC lifetime implies direct economic advantages (infrequent tile replacements) [10, 11] and fewer safety concerns (limited dust production) [12–14]. Consequently, frenetic R&D efforts have focused on the reliable modeling of PFC damage.

The PFC longevity and power handling capabilities are mainly threatened during unplanned transients such as edge-localized modes, vertical displacement events (VDEs) or major disruptions [10, 15]. Given that incident plasma particles (electrons, ions) have typical energies in the low keV range and thus a submicron depth range [16], such scenarios essentially imply surface heating. Dedicated EUROfusion and ITPA coordinated experimental activities [11, 17–22] have provided a wealth of empirical data on metallic PFC melting induced by surface heat loads, which have guided the development of self-consistent physics models based on thermoelectric magnetohydrodynamics (MHDs) within the shallow water approximation that enable high-fidelity simulations [23–30]. Successful validation against multiple tokamak experiments [15] has lent confidence in their predictive power [31–34].

Conversely, the understanding of the potentially most disastrous source of damage—the impact of REs on PFCs—remains in its infancy [10, 15]. The volumetric nature of the energy deposition of REs into matter [16] together with the fast timescales and high energy densities associated with RE impacts [35] result in complex PFC responses beyond incompressible hydrodynamics. Thus, the potentially catastrophic consequences of RE-induced PFC damage for tokamak operation include deep volumetric melting, in-vessel loss-of-coolant accidents [35], debris expulsion, as well as non-local cratering [15]. This has been evidenced in current tokamaks worldwide, which have reported explosive PFC events (see figure 1(top) and tables 1 and 2). REs will pose a more severe threat to future fusion devices such as ITER, where more stored magnetic energy will be available for conversion to RE energy, in particular via the powerful avalanche mechanism [36–38].

Unfortunately, the physics of RE-PFC interaction and its practical consequences are currently poorly explored, largely due to the absence of controlled experiments capable of providing sufficient input and empirical constraints for theoretical modeling [15] and due to the large extrapolation steps from contemporary devices to ITER and future fusion reactors [36–38].

The very recent ITER re-baselining, that foresees tungsten (W) as the plasma-facing material in both the divertor and the first wall, has brought the topic of RE-induced PFC damage to the forefront [10]. According to the modified research plan, the start of research operation (SRO) campaign will use inertially cooled temporary W panels [10, 39]. This will allow experience to be gained concerning the

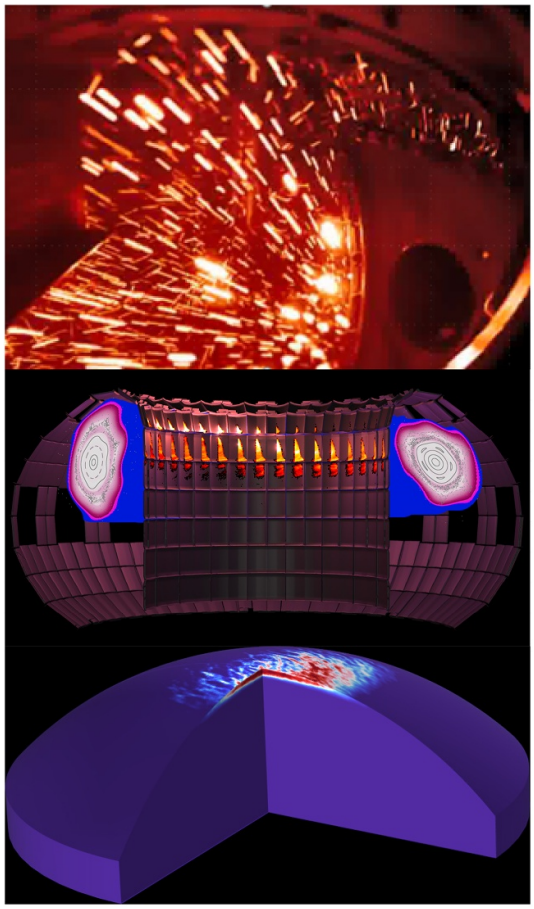

Figure 1. Top: visible camera image of the material ejected from a metal wall in Alcator C-Mod as a result of a RE beam impact on the plasma facing components. Courtesy of R. Granetz. Middle: JOREK simulation of a RE beam termination and the resulting load to plasma facing components during a RE beam termination in ITER [2, 3]. Courtesy of H. Bergström. Bottom: brittle failure calculations in a graphite PFC exposed to a strong RE beam [4]. Courtesy of T.Rizzi.

emergence, mitigation and avoidance of major disruptions and REs, without risking damage to the actively cooled costly W panels that will be installed for the DT campaigns. The ITER re-baselining further motivated ITPA and EUROfusion coordinated experimental activities. The first controlled experiments on RE-induced damage in instrumented graphite domes were recently performed in DIII-D [40] and the first controlled experiments on RE-induced damage in instrumented W tiles have been scheduled in the ASDEX Upgrade (AUG) and WEST tokamaks within the EUROfusion Tokamak Exploitation Work Package.

This is in resonance with recent achievements in the predictive and interpretative modeling of formation and transport of REs towards the vessel wall. In view of such simulation capabilities, a whole hierarchy of models has emerged with entirely different complexities, computational costs, and predictive capabilities. These range from fast lower dimensional models (e.g. [41, 42]) to the computationally much more expensive but also more self-consistent 3D global non-linear codes that can capture the complex mutual interaction between REs and large-scale plasma instabilities (e.g. [43, 44]). Results for an ITER RE beam termination are shown in figure 1(middle). RE Besides the spatial dimensionality, these models differ also in terms of their ability to resolve the phase-space distributions and RE wall deposition. Since RE induced material damage requires not only the deposition patterns, but also the energy and incidence angles of the incoming particles, predictive capabilities are boosted if all this information is available from high fidelity plasma and RE simulations for the calculation of wall heating and damage. Such integrated workflows are a key for a full understanding of the circumstances under which highly localized RE induced damage can occur, on one hand, or the much more desirable benign termination with broad deposition and an absence of pronounced hot-spots, on the other hand.

The dramatic increase in potential RE avalanche gain during disruptions between present devices and their future successors such as ITER or DEMO power plants leads to qualitative changes of the expected RE dynamics [45]. Indeed, while avoiding large RE beams is relatively easy in present machines (where one instead typically needs a dedicated ‘recipe’ to generate such beams), models suggest that in ITER

Table 1. Accidental RE-induced damage; brittle PFCs.

Device	Material/PFC type	RE-PFC interaction	Ejection of debris
JET	CFC, e.g. UDP	Only wetted areas known, hot spots ∼10 cm	Unclear
TCV	Carbon walls	No damage identified	Observations not yet linked to RE impact
COMPASS	Carbon and graphite, e.g. limiters, probes BN support structure	Strong erosion, cratering, surface and bulk cracks Strong erosion, BN fragments found	Yes Yes
TEXTOR	Graphite, e.g. limiter, probes, probe housing	Strong erosion, cracks	Unclear
Tora Supra	CFC walls	Black markings, no signs of major damage	Yes
WEST	BN inner wall and limiter tiles	Strong erosion	Yes

Table 2. Accidental RE-induced damage; metal PFCs.

Device	Material/PFC type	RE-PFC interaction	Ejection of debris
JET	Be UDP	Splashed melt pools over tile's apexes	Yes, possibly droplets
Alcator C-Mod	Mo wall tiles	Melt damage	Yes
FTU	Mo and TZM limiters	Severe melt damage, cratering on surrounding PFCs by high-speed debris impacts	Yes, $\sim 1\,\mathrm{km\,s^{-1}}$ fast solid debris
WEST	W divertor tiles W outer limiter tiles	Trailing edges melting, splashes Splashed molten pools	Yes Yes
EAST	W tiles of the main limiter	Splashed molten pools	Yes

and DEMO, multi-MA RE beams may be very difficult or even impossible to avoid in case of disruption at full plasma current [46]. Furthermore, a possibly strong re-avalanching may take place after a partial RE termination event and, consequently, repetitive cycles of re-formation and termination may arise in future high-current tokamaks. Predicting the consequences and optimizing the mitigation strategies in this context cannot rely on experiments alone, but requires a holistic predictive view onto the involved processes originating from theory and simulation. Such input is needed to constrain plasma operation in view of risk mitigation when ITER moves towards full-current operation, and it is essential for designing well targeted and dimensioned engineering solutions like sacrificial limiters, which are considered in order to protect the first wall from RE impacts in various future devices. The landscape of different simulation tools with very complementary capabilities is overall developing towards the ability of providing such input in the coming years, although there are still clear gaps in the present capabilities that will need to be addressed.

Thus, the conditions are mature and the timing is critical for major advances in the genuinely multi-physics problem of the PFC response to RE impacts by synergetic theoretical and experimental efforts.

Historical background

One of the first evidence of intense RE-PFC interaction was reported 50 years ago in connection to neutron measurements of the ion temperature in the TFR CEA tokamak [47]. In particular, large neutronic fluxes of non-thermonuclear origin were found to be correlated with the presence of REs in plasmas.

Figure 2. RE-induced damage of a stainless steel antenna from 1983 ASDEX experiments on lower hybrid heating [53, 54] due to $\geq$5 MeV electrons that also caused nuclear material activation. Courtesy of Dr F. Leuterer with permission.

Already existing measurements of the neutron yields from 10 to 30 MeV electron bombardment of high-Z solids [48], led to the interpretation of these fluxes as being photoneutrons. In fact, RE transport leads to the generation of high energy photons through bremsstrahlung which can be absorbed by nuclei that are subsequently de-excited by emitting neutrons. Two years later, direct observations of photoneutrons that emanated from a W limiter after RE incidence were reported in the Princeton PLT tokamak [49]. Later, the diagnostic based on photoneutron production upon RE-vessel interaction has been employed in the Frascati Tokamak (FT) [50], Joint European Torus (JET) [51] and Japan Torus-60 Upgrade [52].

Since then, the empirical database of RE-induced PFC damage in tokamaks with graphite (figure 1 shows modeling of a brittle failure resulting from an RE beam impact) and metallic composition has significantly expanded. Among early documentation of damage of metallic PFCs is the evidence from ASDEX experiments on lower hybrid heating. Upon extraction of the antenna, made of stainless steel with 8 mm walls, significant melting and melt splashing was found at the front-ends of the central waveguides, shown in figure 2. The interpretation that the observed damage is caused by high-energy RE impacts was proposed back in 1983 [53, 54]. In addition to instances of in-vessel component degradation of various degrees, there have also been reports of costly damage events, such as severe material loss from signal cables of soft x-ray (SXR) tomography arrays in Alcator C-Mod (see section 3), water leakage in Tore Supra [55] and the toroidal field coil quench in WEST [56]. The risk of forcing a device out of operation with possibly costly repairs is the prime reason for the fact that by far the majority of RE-induced PFC damage observations are a result of *accidental events*.

The lack of *controlled* RE-driven damage experiments has crucially impeded the development of RE-induced damage models. Only recently first controlled experiments have been carried out with graphite samples in DIII-D [40] followed by a prompt progress in modeling of RE-inflicted brittle failure of such material [4]. Meanwhile, the first controlled experiment on tungsten damage was conducted in WEST at the time of writing this Roadmap. The anticipation from this experiment diagnostics is that information on RE energy and pitch angle distributions shall be available along with the energy deposited in the tiles and ejecta details (timing of release and debris size and speed). Such data shall enable validation of both RE beam modeling and thermo-mechanical simulations of ductile at high temperature material with liquid phase, aiming at predictions of not only temperature response but also the expelled volume and ejecta characteristics.

Classification of possible impact scenarios

RE beam impacts are typically associated to their motion towards PFCs, which can be either intentional or due to a loss of position control. There then seems to exist two types of impact scenarios. In *scrape-off* impacts, magnetic surfaces are well preserved. This type can be subdivided into two variants depending on whether the beam remains axisymmetric or not. The impacted PFC area for *scrape-off* impacts is small and presumably determined by a combination of the beam trajectory, RE Larmor radius, orbit shifts, beam distortion and PFC geometry, but a good understanding remains to be developed. The timescale of *scrape-off* impacts is set by the speed at which the beam moves 'into' PFCs. On the other hand, in *stochastic* impacts, magnetic stochasticity develops as a consequence of plasma instabilities (often denoted as a burst of MHD activity). In this case, the amplitude and growth rate of the stochasticity may determine both the impact time scale and deposition area. The former may be much smaller and the latter much larger than for *scrape-off* impacts. Note that a given impact might combine the *scrape-off* and *stochastic* types. For instance, it may start as *scrape-off* and later turn into *stochastic*. Observations and modeling of some impacts e.g. on TEXTOR [35] or JET [57] suggest that they are of

the *scrape-off* type. *Scrape-off* impacts are also often the baseline assumption in predictions for future devices (see e.g. section 10). However, it is presently not fully clear what type of impacts take place in existing devices or are to be expected in future ones. This topic should be a focus of future work.

Benign terminations

An important experimental discovery from recent years is the possibility of benign RE beam terminations [58, 59]. Those are obtained through the injection of H or D into the beam, which recombines the background plasma and 'purges' it from its impurities, leading to fast and strongly *stochastic* impacts with no ensuing RE re-generation. Efforts are ongoing to better understand the physics at play.

Extrapolation and mitigation strategies

As will be detailed in sections 5–7 and 9–10, evading the formation of dangerous RE beams in large future tokamaks is predicted to be very difficult. The best hope in this area may be the RE mitigation coil (REMC) to be tested e.g. on SPARC. If dangerous RE beams cannot be avoided, the foreseen impact mitigation strategies rely on (i) benign terminations (e.g. in ITER) or (ii) sacrificial limiters (e.g. in European Demonstration (EU-DEMO)). However, access conditions to benign terminations might not be compatible with other disruption mitigation requirements, and there is also a higher risk of RE re-formation after a stochastic loss event in larger machines. On the other hand, sacrificial limiters are challenging to design. In this context, the exploration of alternative RE avoidance or mitigation techniques appears justified.

Structure of the roadmap

RE-induced PFC damage is a genuine multiphysics problem. The complete workflow for the modeling of material damage driven by RE incidence needs to address (i) the properties of the RE beam (current density profile, energy and pitch angle distribution) and its companion plasma (composition, density, temperature) before the impact, (ii) the transport of REs to the wall and the determination of their impact characteristics (location and momentum), (iii) the transport of the REs and the particle shower products inside the PFC until their complete thermalization, (iv) the thermomechanical response of the PFC to the combined RE volumetric load. This constitutes a highly complex modeling chain, with each block characterized by its own uncertainties and simplifying assumptions, that requires controlled well-diagnosed experiments for its validation. The synergy between modeling and experiments is imperative and is reflected in the structure of the present roadmap.

Experimental evidence is an essential element in the understanding of the physical mechanisms behind PFC damage. Sections 1–3 are surveying RE-induced PFC damage evidence in all major tokamaks, including devices which are no longer in operation, see tables 1 and 2. We point out that a consistent global picture of why RE beams and associated damage are seen in some machines or pulses and not in others is problematic to establish due to the *accidental* nature of the events. Some trends have however been identified, in particular concerning the propensity of poorly conditioned machines to generate REs during the plasma startup phase and, as aforementioned, the lack of RE beam formation in natural disruptions in most diverted/elongated machines (with the notable exception of JET during the carbon wall era [51, 60, 61]). These sections also highlight challenges in designing and conducting controlled experiments to provide sufficient empirical constraints to physics models, see table 3.

This is followed by section 4, which describes present and future diagnostic techniques that are capable of characterizing the incident REs (energies, pitch or impact angles) and the PFC response (e.g. temperature response, total energy received).

Generation and transport of REs before and during their impacts on the wall is a critical input to the modeling of PFC thermo-mechanical response. Sections 5–7 describe the tools available for this and their further developments. More precisely, section 5 concentrates on models that aim to characterize the RE beam properties prior to its termination, section 6 addresses reduced models for disruptions and beam terminations, and section 7 describes computationally expensive high fidelity models in which the 3D plasma dynamics is self-consistently coupled to the RE dynamics.

The modeling of PFC damage is described in section 8 focusing on the Monte Carlo (MC) simulation of the electromagnetic (EM) shower that is induced by relativistic electron passage into condensed matter and on the finite element modeling of the thermomechanical PFC response to the generated volumetric loads.

Table 3. First controlled RE-induced damage experiments.

Device/Year	Experimental details	Results
DIII-D 2022-2024	Graphite dome-shaped sacrificial limiters, with thermal couple & radiation detectors	Top of the limiter blown away, explosive release of debris
WEST April 2025	Inner limiter W tile with thermal couple	Melt splashing and release of debris
AUG	W sample, with thermal couple and radiation detectors	Upcoming

Section 9 is dedicated to PFC activation due to interaction with REs with incident energies above the kinematic threshold of photo-nuclear reactions.

The roadmap is concluded with discussions on future reactors, section 10 providing the perspective of ITER and section 11 the perspective of future large tokamaks planned around the world.

Note that all acronyms and abbreviations used in this article are listed in a table in the appendix.

Guest Editors

Svetlana Ratynskaia, Matthias Hoelzl and Eric Nardon.

2. RE-induced PFC damage in JET

I Jepu[1] *and C Reux*[2]

[1] UKAEA, Culham Campus, Abingdon, OX14 3DB, United Kingdom
[2] IRFM, CEA Cadarache, F-13108 Saint-Paul-lez-Durance, France

Status

In 40 years of operation, from 1983 until 2023, the JET [62, 63] tokamak has been pivotal in the advancement of fusion research, being the perfect testbed for different operation scenarios directly applicable to future fusion devices such as ITER and DEMO [64, 65]. During its lifetime, JET has operated with two main wall configurations as PFCs. Between 1985 and 2009, JET's PFCs were predominantly carbon fiber composite (CFC) (*JET-C*) [66], while from 2010 to 2023 JET's PFCs were upgraded to the metallic wall configuration, comprising beryllium (Be) in the main chamber and pure tungsten (W) and W-coated CFCs (W-CFC) in the divertor, also known as *JET-ILW* (JET with a W divertor and main chamber Be) [67–69].

JET-C era. During *JET-C* the PFCs were predominantly CFCs, and RE generation was frequently observed during major disruptions. Early studies showed that during carbon limiter disruptions, large RE currents, sometimes reaching 1 MA, were created, causing high photoneutron bursts and localized damage to PFCs [51, 61]. This wall material had several implications for RE physics. The low atomic number of carbon, decreased impurity radiation, which enabled high performance operations, but also altered the dynamics of the RE beam interaction with the wall. Under these conditions, experimental studies revealed that unmitigated plasma disruptions typically produced consistent RE avalanches [70]. The rapid current quench (CQ) phases that were induced by the significant radiation of carbon accelerated electrons via the Dreicer mechanism [71] and subsequent avalanche multiplication. In this regime, although REs were frequently produced, the high resistance of carbon to sublimation and erosion often led to damage that was more spread out, especially when compared to the severe damage observed on metallic surfaces. In several dedicated experiments [72], a series of major disruptions were triggered using either massive gas injection (MGI) or by a slow constant puff of impurity gas [73]. These experiments allowed the comparison of 'fast' versus 'slow' disruptions. Fast disruptions produced by rapid MGI were characterized by a steep CQ (typically on the order of 3–7 ms), leading to induced electric fields several hundred times larger than the Dreicer field. Such large fields could accelerate electrons rapidly. Up to 60%–70% of the pre-disruption plasma current could be carried by a beam of REs with energies reaching 10–15 MeV and currents on the order of 1 MA [73]. These quantitative measurements have been verified against diagnostic signals such as hard x-ray (HXR) emission, neutron bursts, and spectroscopic data. Complementary data from neutron diagnostics and fast visible cameras further constrained the RE density and current. Ultimately, the RE beam could reach the first wall and lead to severe damage.

Evidence of PFC damage in JET-C era. The most noticeable result of RE generation in the *JET-C* configuration was the formation of high-power levels of hard radiation, gamma rays, and some neutrons when the REs interact with the vessel walls. The SXR images in [74] show that REs interaction with the wall is confined to small areas with poloidal widths below 10 cm on the upper or lower vessel parts, depending on the direction of the vertical movement of the beam. Observation of discrete pulses (bursts) of HXR emission during the impact duration suggests that the runaway current channel itself is filamented [75]. In a comprehensive study described in [76], analyzing close to 20 000 JET pulses, RE detection was done by using the increasing neutron rate during CQs. This way, it was determined that for 8% of these pulses, REs were detected in limiter and divertor configuration. However, observations of the heat load during RE production, and consequently damage to the PFCs, were rarely documented. Figure 3 shows the first RE impact measured with a wide infrared (IR) camera reported in [76]. For this particular case, an RE current of 0.48 MA was produced. The entire recording consisted of two frames only. During the thermal quench (TQ), heating of the divertor and inner limiter is observed in the first frame of this recording, while in the second frame, taken 20 ms later, a temperature increase is noticed on the upper dump plates (UDPs), which consequently was attributed to the RE beam impact with the PFCs. Figures 3(a) and (b), show the two frames. In figure 3(a) the thermal radiation is presented on the inner limiter and lower inner divertor during the disruption that led to the RE generation, while figure 3(b) shows the IR image of the heated UDPs as a direct consequence of the interaction with the RE beam. Based on the IR imaging, it was assessed that

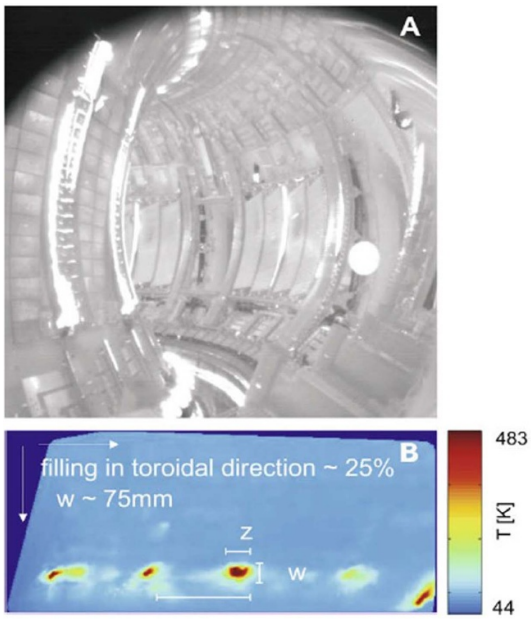

Figure 3. Heat load distribution during the disruption of JET pulse no. 68 782. Over-exposed overview frame for visualization (a) and temperature rise at the upper dump plate due to runaway impact (b). Reprinted from [76], Copyright (2009), with permission from Elsevier.

the temperature increase between the two frames was of 530 K, while the wetted surface area heated by the RE impact was found to be ∼0.3 m^2. It was noted that the inhomogeneous heat load might have been caused by a small tile misalignment, which can have a considerable effect at low angles of incidence.

Similar type of dump plate damage induced by REs was also discussed in [77]. In this work it was noted that for 17 JET pulses studied, the red localized spots, similar to those shown in figure 3(b), are footprints of the distinct impacts measured on UDPs, implying that the dump plate geometry defines the heat load distribution. In addition, it was reported that the temperature increase measured on the CFC tiles scales with the square of the RE current.

As a concluding remark, RE experiments in *JET-C* highlighted the potential of high RE currents and associated PFC damage including high temperature spots, localized erosion as well as dust generation. These effects, although far less obvious in a carbon wall environment as compared with a metallic wall configuration, were considered of high importance for the long-term integrity of the PFCs and plasma purity. The results in *JET-C* served as a benchmark for further RE studies [78, 79].

JET-ILW era. With the introduction of *JET-ILW* configuration, the RE formation changed significantly. Prior observations made by G. R. Harris in [80] had already highlighted the strong reduction of RE production in unmitigated beryllium limiters disruptions [81], attributing this to the lack of radiative collapse and development of long CQs. As reported in [82], only 2 out of 7000 *JET-ILW* pulses up to 2014 JET operations (ILW1 and ILW2) showed low-energy REs during a low density current ramp-up due to a failure of the gas introduction system. Compared to *JET-C*, *JET-ILW* disruptions showed a lower radiated energy fraction, resulting in a higher plasma temperature post TQ, which slowed CQs and therefore decreased the probability of RE beam formation [83, 84]. The study in [85] confirmed this mechanism by reducing the likelihood of avalanche RE generation during spontaneous disruptions triggered by slow argon injection. In this final wall configuration, the RE generation was achieved only through deliberate argon MGI, rather than during unmitigated plasma disruptions. When MGI was intentionally applied for disruption mitigation, RE beams of several 100's kA were produced [86]. The operational RE domain for MGI-induced disruptions was found to be similar to that in *JET-C*. JET experiments in the ILW era have employed advanced diagnostics, such as fast visible and IR cameras, HXR detectors, and spectroscopic techniques to capture the evolution of RE beams and their interaction with PFCs.

Evidence of PFC damage in JET-ILW era. With the installation of ILW in 2010, due to the lower melting point of beryllium covering the main chamber, a significant consideration was given to the operation

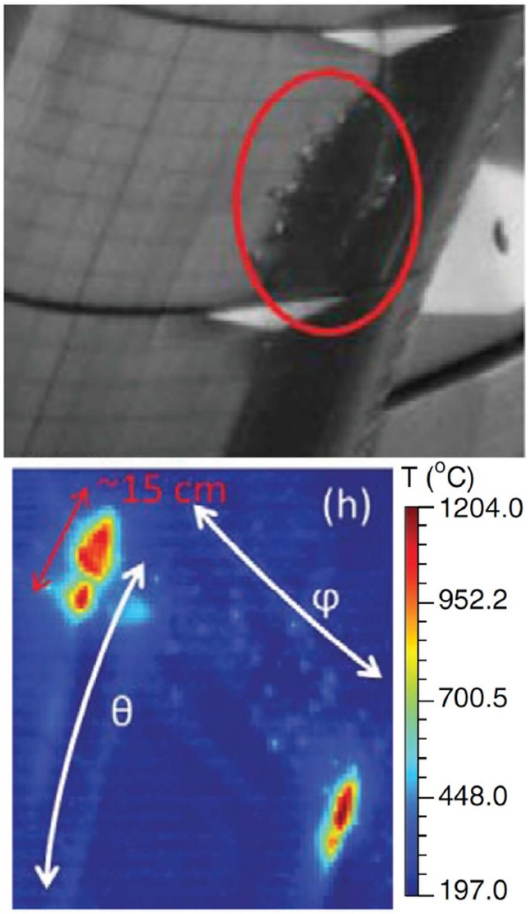

Figure 4. RE beam impacts on Be tiles; visual inspection of the damage and an IR image of the impact. Reproduced courtesy of IAEA. Figure from [82]. Copyright (2015) IAEA.

scenarios to avoid a significant PFC damage due to unmitigated plasma disruptions and RE impacts. The values of new tolerable heat flux factors (typically employed to quantify thresholds for material integrity by incorporating both the strength of a transient heat flux and its duration [87]) were more restrictive, with Be and W melting occurring at $\simeq$20 MJ $(m^2 s^{1/2})^{-1}$ and $\simeq$50 MJ $(m^2 s^{1/2})^{-1}$, respectively [72, 83].

Between 2010 when the ILW replaced the carbon configuration, and 2016, three main campaigns, also known as ILW1–ILW3, were run. Each of the campaigns had different operational purposes: ILW1 (2010–2012) focused mainly on the influence of the new wall on the plasma operation, material migration and fuel retention, ILW2 (2012–2014) focused on high power scenarios and disruption mitigation by MGI, while ILW3 (2014–2016) aimed at an increase of fusion performance (see [20] and references therein).

During ILW2, a comprehensive study on RE generation and mitigation was performed and fully described in [82, 86]. For this purpose, REs were induced using one disruption mitigation valve by delivering an argon MGI. First evidence of PFCs damage due to low RE currents was reported in [86] showing that the Be tile melting was unlikely below an RE current of 150 kA. In [82] it was reported that RE beam impacts on Be UDPs resulted in energy deposition over a depth of approximately 2 ± 1 mm, with only a portion of the beam's total energy being absorbed by an individual tile. Instead, a considerable fraction of the beam current continued and struck the next tile in the toroidal direction. Observations made using a wide angle IR camera similar to the one used in the JET-C case described in [76] confirmed that multiple hot spots on UDPs were visible for a given RE event. Toroidal symmetry, although not perfect, was found to be reasonably good in the short toroidal section viewed by the camera. The hot spots were found to cover a similar area of interaction as reported in [77].

It was found in [82] that the impact from long-lasting and less vertically unstable RE beams in a limiter configuration present a different scenario. The beam strikes the upper part of the JET inner wall

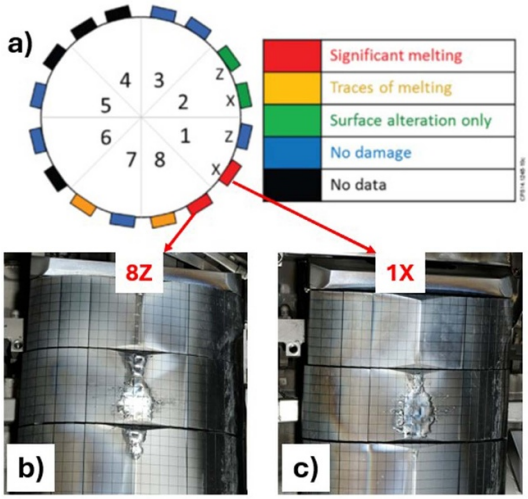

Figure 5. Map of RE-induced tile damage on the IWGL (a) and images of the two most affected tiles, (b) and (c). Reproduced courtesy of IAEA. Figure from [82]. Copyright (2015) IAEA.

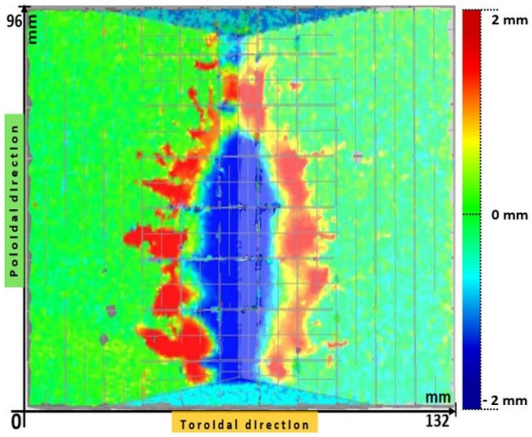

Figure 6. The 3D profiling reconstructed damage of Be tile (shown in figure 5(c)) affected by RE impacts. Reproduced from [88]. CC BY 4.0.)

guard limiter (IWGL) over an area of roughly 10 cm^2 per tile. A fast IR camera recorded a peak temperature of 1400 °C, which is above the melting point of Be (1287 °C). Following the RE impact, a significant material ejection was observed from the inner limiter, see figure 4. Be droplets observed from both inner limiters shown in figure 4 most likely have ended in the divertor area. Similar type of Be droplets, observed via IR cameras, were seen post unmitigated plasma disruptions events affecting the UDPs [20, 88]. Given the limited camera resolution and that these observed droplets are close to the pixel resolution limit, accurate estimations of droplet size and overall Be mass ejected are not feasible. Meanwhile, the metallic splashes and solidified droplets found on various wall components and in the divertor area were in the range from a few nm to 500 μm [20, 88–91] .

Localized melting was also confirmed by in-vessel visual inspections. Furthermore, a toroidal damage map presented in [82, 88] revealed the complexity of the observed RE-induced PFC modifications. The damage extended across several adjacent limiters along the toroidal direction before gradually fading, see figure 5(a). During the 2017 JET intervention, several components were exchanged. Among those removed was the central component of the 1XR18 IWGL tile, depicted in figure 5(c). The first damage assessment was carried out during the remote post-experimental inspection while results of the morphological and structural analysis of this tile were reported in [88].

The result of 3D profiling measurement performed on the removed tile is shown in figure 6 where 'zero' on the scale refers to the undamaged or 'reference' surface. Displaced and re-solidified Be melt can be seen as 1–2 mm high elevations, along with 1–2 mm deep 'valleys'. The estimated area below

the reference was $\sim$11 cm^2 while the area above the reference was close to 14 cm^2. The overall damage area was assessed to be $\approx$21% of the total surface area. The analysis confirmed that the REs caused significant but very localized damage featuring melt splashing and material ejection from the impact areas yet without major effects on the surrounding PFCs. Evidence of molten material bridging gaps between adjacent castellations but with no accumulation of the molten material into the gaps was also reported in [88]. The analysis of the topography and crystallographic structure in the damaged region revealed that the molten material re-solidified within a near surface, $\approx$330 μm thick, layer. This re-solidified region features a columnar grain structure with elongated grains oriented perpendicular to the surface, and the length of these grains typically matches the thickness of the re-solidified layer.

Later, post the 2017 intervention, campaigns continued to study the RE beams created during disruptions. The observed destructive patterns were similar to the previous campaigns, with no significant changes to the damage asymmetry map. Some limiters were badly affected, and some others completely unscathed, over the course of several tens of RE impacts. RE heat loads were significantly reduced with the discovery of the so-called 'benign termination' scenario in 2019 [58], with heat loads barely measurable when the method was used successfully (see Introduction for more details). Some damage was still recorded on limiters and divertors following explorations of the validity domain of the benign termination scenario.

Current and future challenges

During the final weeks of JET operation in November–December 2023, a series of dedicated experiments were conducted to examine the impact of RE beams on both the main chamber limiter tiles and the divertor. New damage evidence was found on the IWGL tiles. A high-resolution image survey conducted in the summer of 2024, following JET's final operational campaign, will generate an updated toroidal damage distribution map similar to those presented in [82, 88]. A single RE damage event, linked to a single purposely designed JET pulse, was identified in the last days of the operation, and its analysis will contribute to the toroidally resolved assessment of inner limiter damage due to RE impacts. Additionally, for the first time in JET operating in the ILW configuration, clear evidence of RE impact on the inner divertor was observed. Divertor impacts are visually very different from limiter impacts in the sense that they produce many more ejecta from the impact point. The nature of the ejecta is not completely clear as some of the affected areas are covered with deposits. It is therefore possible that they contain a mixture of molten W coatings, ablated deposits (mostly Be) [92] or C substrate. A toroidal distribution assessment for the divertor damage is planned, with the preliminary results indicating similar localized behavior and the absence of toroidal uniformity, consistent with the previously observed localized nature of RE impacts [82, 88]. In addition, future studies will assess the W coating removal due to such events, its implication for the integrity of the PFC along with fuel retention and release mechanism behavior.

Concluding remarks

RE damage to PFCs in JET has evolved considerably between the *JET-C* and *JET-ILW* eras. In the carbon-wall configuration, robust RE production during disruptions was observed, yet the carbon properties limited the severity of local damage. The resulting damage was less localized, with material losses distributed over larger areas, hence reducing the risk of major PFC failure. In contrast, the ILW configuration, comprising Be in the main chamber and W-based materials in the divertor, produced a different response to the RE production. While spontaneous RE generation was drastically reduced, triggered events via MGI was the way to produce high-current RE beams. These beams deposited energy in a highly localized manner, often resulting in intense, concentrated heat loads. This caused significant material displacement, and in some cases led to splashing of melt pools, with droplet ejection contributing to both PFC erosion and the overall dust inventory. The legacy of JET's comprehensive investigations in both configurations provides crucial information that will drive future design and operating methods for safely managing RE occurrences in next-generation fusion reactors. In particular, the benign termination scenario recently studied on JET [58] opens a hope for damage-free RE mitigation.

3. RE-induced damage of brittle in-vessel components

E Hollmann[1], U Sheikh[2], E Tomesova[3] and H R Koslowski[4]

[1]University of California—San Diego. San Diego, CA 92093, Unites States of America
[2]Swiss Plasma Center (SPC), Ecole Polytechnique Federale de Lausanne (EPFL), CH-1015 Lausanne, Switzerland
[3]Institute of Plasma Physics of the CAS, CZ-18200 Praha 8, Czech Republic
[4]Forschungszentrum Jülich GmbH, Institute of Fusion Energy and Nuclear Waste Management—Plasma Physics, 52425 Jülich, Germany

Status

DIII-D. Post-disruption RE experiments in DIII-D typically study RE formation and dynamics [93, 94]. During the experiments, inadvertent wall damage was occasionally observed; for example, in one experiment the outer midplane plunging probe was accidentally struck by a RE beam, leading to probe tip damage. More recently, experiments dedicated to studying RE-induced damage to brittle PFCs have been performed. These experiments have used domed ATJ graphite limiters with a peak height of 1 cm above the lower divertor floor, as shown in figure 7. These limiters have been intentionally struck with downward-moving high-current (≈600 kA) post-disruption RE beams. Significant shot-shot variation in limiter damage has been observed; this variation has been attributed to shot-shot variation of the toroidal phase of the dominant RE loss to the floor. In all cases, the RE final loss event (instability) causes rapid (<1 ms) loss of REs into the limiter head. The REs hitting the limiter are expected to have a wide range of kinetic energies, but with an average of order 2–4 MeV [40]. The initial in-plasma RE pitch angle (RE velocity vector relative to magnetic field vector) is thought to be fairly small, of order 0.1–0.2 on average; the experiments indicate that this may increase slightly (to perhaps 0.3–0.4) during the final loss process [40].

To-date RE graphite damage to the sacrificial limiters has been roughly grouped into three categories. At low RE fluences $q_0 < 100\,\mathrm{J\,cm^{-2}}$, no apparent change to the graphite is observed. At intermediate fluence $q_0 > 100\,\mathrm{J\,cm^{-2}}$, an apparent surface morphology or phase change is observed on the sample surface, with the graphite appearing darker on visual inspection. At high RE fluences $q_0 > 1000\,\mathrm{J\,cm^{-2}}$, an explosive destruction of graphite and dust release is observed. The heat fluences are estimated from thermocouple and IR imaging data. The destruction depth is of order 1 mm, comparable to the RE surface penetration depth. The observed destroyed volume agrees with modeling of carbon bond failure in the graphite volume [4]. Modeling is continuing to understand the observed dynamics of explosive dust release. For example, the dust appears to be released approximately 1 ms after RE impact at velocities in the range 100–150 $\mathrm{m\,s^{-1}}$ [40]. Example images of dust release and limiter damage are shown in figure 7.
TCV. The TCV tokamak, a carbon-walled machine capable of generating RE beams exceeding 250 kA [95, 96], has been the focus of extensive research on RE generation mechanisms, transport, and mitigation strategies. Despite numerous experiments and high-current RE events, no direct damage to PFCs has been observed [96–98]. Explosive dust releases have been periodically observed on visible and IR cameras, however, no systematic study has been conducted to link them to RE impact. IR measurements indicate that surface temperature increases from RE impacts on TCV typically range from 50 to 100 K, corresponding to heat fluxes on the order of 0.1–1 $\mathrm{MW\,m^{-2}}$ with a total energy in the order of 10 kJ [96, 98].

The only documented case of RE-induced damage occurred not on a PFC but on a diagnostic component-the Cherenkov probe. It was associated with two consecutive pulses featuring a large RE seed population (expected to be over 50% of the pre-TQ current based on LUKE simulations [97, 99]) and a thermal companion plasma with an electron temperature of approximately 1 keV [100]. During the current ramp-up to the prescribed 250 kA flattop, plasma control was lost, resulting in a VDE. Consequently, the RE beam and plasma column shifted upwards, directly impacting the protruding Cherenkov probe, which extended approximately 1 cm beyond the front surface of the adjacent tiles. This exposure to the high-energy RE beam caused the localized melting visible in figure 8(bottom), contrasting with the probe's pre-installation condition shown in figure 8(top). The outer diameter of the graphite head is 30 mm and the inner diameter of the metal detector assembly is 14 mm. The melting is predominantly observed on the spacer plates (distinguished by the front flat surfaces), which are made from TZM, a molybdenum-based alloy with 0.50% titanium, 0.08% zirconium and 0.03% carbon. The detectors themselves, distinguished by the rounded front surfaces, are made from CVD diamond with a Ti/Pt/Au interlayer 1.3 μm thick, and 0, 25 or 53 μm of molybdenum as a variable energy filter.

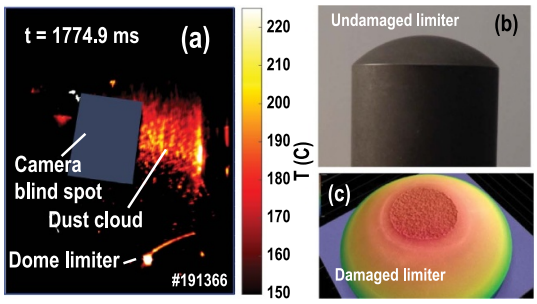

Figure 7. RE damage to sacrificial graphite limiter in DIII-D showing: IR image of resulting dust cloud (a), visible image of undamaged graphite limiter (b) , and confocal microscope image of damaged limiter (c). (a) and (b) Reproduced from [40]. © IOP Publishing Ltd All rights reserved. (c) Reproduced from [4]. CC BY 4.0.

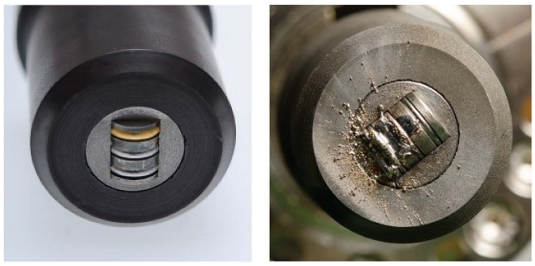

Figure 8. Cherenkov probe on TCV before (left) and after (right) RE impact during a VDE of a 250 kA current plasma with significant RE population. Melting observed on the molybdenum-based alloy spacer plates.

COMPASS. COMPASS [101] was a medium size tokamak with graphite and carbon PFCs and main experimental focus on RE studies. Following massive material injection triggered disruptions, RE currents reached up to 150 kA. Average RE kinetic energies up to ≈10 MeV were estimated, corresponding to a total kinetic energy of ≈5 kJ for 3×10^{15} REs. Most damage events occurred during dedicated RE campaigns, with typical RE impacts either on the calorimetry probe used as the protection LFS limiter [102] or on HFS midplane limiter tiles. Exceptions occurred when beam termination coincided with VDEs or plasma positioning failures.

Damage to the recessed roof-shaped (RR) [104] inner wall graphite limiter, which protruded into the vessel by 4 mm (see [103]) is shown in figure 9(a). Two footprints corresponding to two distinct RE beam positions can be seen. The material loss exceeds 0.2 cm^3. The upper footprint exhibits marks of significant thermal stress and intense ablation, with repeated heating cycles leading to a network of surface and bulk material cracks. The lower, darker footprint experienced shorter RE exposure. The surrounding region's texture suggests material re-deposition. Over 80 RE impacts to the high field side generated graphite dust release. An example is shown in figure 9(b): here, a 60 kA RE beam with RE kinetic energy $\langle E \rangle \approx 12$ MeV struck the center post. Fast IR cameras recorded heat fluxes reaching several GW m^{-2}, corresponding to several kJ of deposited RE beam kinetic energy.

Figure 9(c) presents an optical microscope image of RE-induced damage on a carbon Langmuir probe located on the calorimetry head [102]. The probe, subjected to about 200 RE impacts, exhibited coalesced cracks resulting in material detachment over a large area, visible as a gray, slightly blurred region without craters. The remaining surface features craters approximately 100–200 μm in diameter and up to 100 μm deep. Energy dispersive x-ray spectroscopy (EDS) analysis confirmed silicon sublimation, indicating probe surface temperatures of at least 1200 °C.

U-probe [105] carbon pin damage shown in figure 9(d) was probably inflicted in a single RE event. In contrast, the U-probe body, composed of boron nitride (white area), experienced multiple RE impacts. Debris ejection were detected by visible cameras and boron nitride fragments (of various sizes,

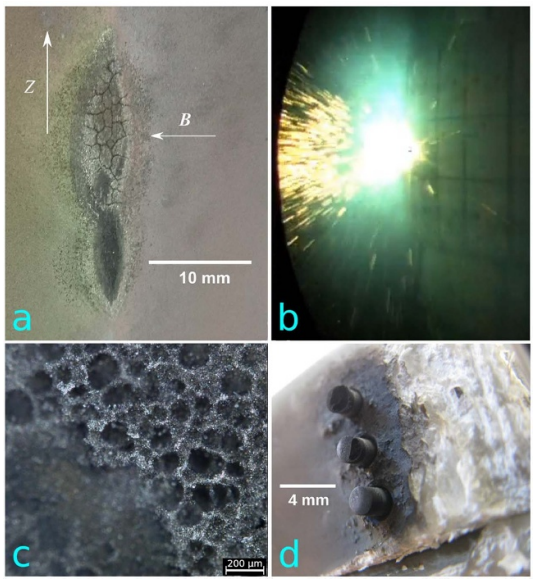

Figure 9. Examples of RE-induced damage of components from COMPASS. Damage to the recessed roof-shaped (RR) graphite limiter (a). Reproduced from [103]. © IOP Publishing Ltd All rights reserved. Debris release during RE termination at the graphite RR tile in discharge 14494 (b). Craters on a carbon Langmuir probe (c). Reprinted from [102], with the permission of AIP Publishing. Carbon U-probe, mounted in a boron nitride support structure (seen as white), after an RE impact (d).

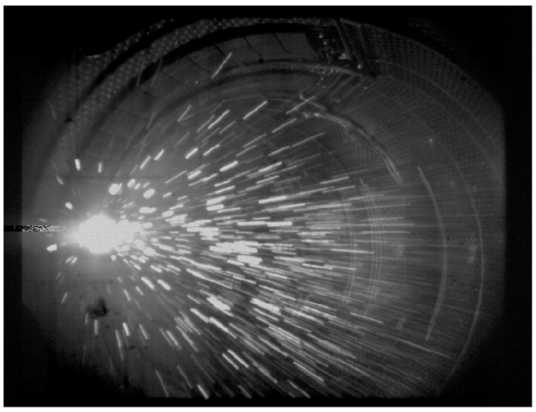

Figure 10. Runaway electron impact on Tore Supra carbon limiter. Courtesy of C. Reux.

up to a few mm large) were later found throughout the lower section of the corresponding port and in the divertor region.

Tore Supra / WEST. Tore Supra was known for extensive RE production and seconds-long RE beams. The carbon-fiber composite wall absorbed most RE impacts, usually leading to dust release, as shown in figure 10. No quantitative analysis of the amount of ablated material was performed at the time. Visually, most of the affected tiles were left with black markings only and no other sign of major damage.

Tore Supra was later upgraded to WEST [106], with tungsten PFCs. Between 2020 and 2024, the 4 central rows of the inner wall and the 5 central rows of the outer limiter were replaced by boron nitride tiles to facilitate operation in the tungsten environment. These tiles were hit by up to ∼10 RE beams during dedicated experiments. As with the carbon impacts in Tore Supra, dust ejection was observed after the impacts. The tiles were damaged (see figure 11), with a visibly cracked surface similar to that of tree bark [107]. A thickness of 1 mm of material was lost for the most badly damaged tile. Plasma operation was only moderately affected following impacts, with a hot spot probably resulting from the uneven surface of the tile when the plasma was put in contact with the damage. The hot spot disappeared after a few experimental sessions, most probably eroded by plasma thermal loads. The RE damage was found to be toroidally asymmetric, with one of the inner limiters badly damaged, three others moderately damaged and the last two nearly unscathed [107]. This is similar to observations made on JET (see section 1). The cause of this asymmetry remains unknown. Several hypotheses have been

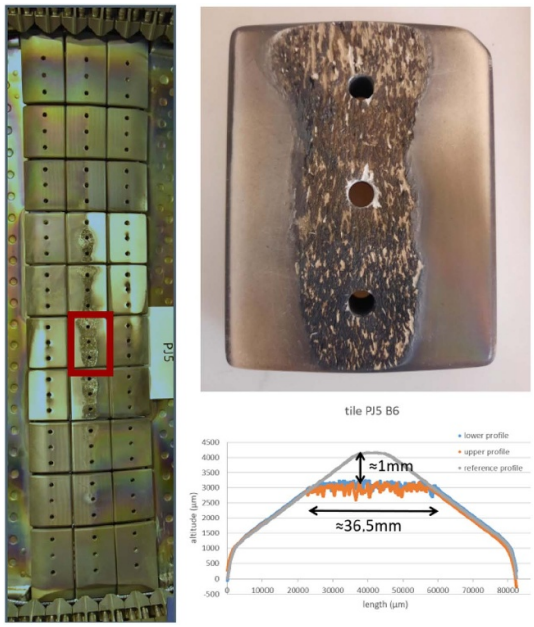

Figure 11. WEST inner limiter PJ5 damaged by multiple RE impacts, along with a zoom-in of the worse damaged tile B6 and its profilometry showing 1 mm deep material loss. Courtesy of M. Diez.

brought forward, including tile misalignments or the intrinsic 3D nature of the RE beam, but no conclusion has been reached yet.

TEXTOR. The TEXTOR tokamak [108] was a limiter machine with circular plasma cross section. The first wall was made of INCONEL and the ALT-II toroidal belt limiter [109] equipped with carbon tiles and three movable poloidal limiters (top, bottom and outboard) covered with EK98 graphite were utilized to control the plasma boundary and protect the first wall. The first reported observations of RE damage to PFCs date back to the 1980s [110]. One graphite 'tooth' of the poloidal limiter at the outboard midplane was found to show erosion craters with a depth of approximately 1 mm. The surface of the limiter tooth showed a cracking pattern parallel to the surface. The damage was attributed to REs formed in low-density plasmas and during disruptions.

RE damage was also observed to a scintillator probe in TEXTOR. The probe consisted of ten YSO scintillator crystals shielded by tungsten layers of various thicknesses. The entire probe was covered with 5 mm of graphite [111]. Inspection after about 30 RE measurements showed that the REs penetrated the graphite and deposited their energy on the inner part of the probe. Surprisingly, strong melting of stainless steel parts inside the probe was observed which has been attributed to energy deposition by the REs inside the stainless steel interior of the probe after passage through the graphite housing [112].

In addition, RE damage to a heat load probe was observed in TEXTOR. This probe had a bulk from epoxy resin with embedded copper particles which was contained in a graphite housing [112]. The probe was designed to provide heat load information by post-mortem analysis of resin melt regions. However, the heating was stronger than expected and the graphite housing cracked and the resin evaporated. Nevertheless, detailed analysis allowed an estimate of the mean RE kinetic energy in the range 8–16 MeV to be made [112].

Finally, RE damage to a calorimeter probe was observed in TEXTOR. The calorimeter probe consisted of a thick piece of graphite along with a thinner piece of molybdenum forming the bulk, and a CFC shield on the surface to protect the interior from the plasma. Both elements had thermocouples inserted to allow a temperature measurement [113]. The probe showed quite severe damage when inspected after RE experiments. The CFC and graphite components were strongly eroded and had mass losses of up to 5 percent, while the molybdenum was partly molten but had lost only less than 1 percent of its mass.

Current and future challenges

A variety of experimental challenges exist in the study of RE-induced damage of brittle in-vessel components. Foremost among these challenges is obtaining good data on incoming RE characteristics.

Modeling of RE damage ideally begins with good data on the RE kinetic energy, pitch angle, and heat flux time history. These are hard to measure, however, as described in section 4; and, in most instances, the characteristics of the impacting REs are not well-known. Nevertheless, recent analytical developments and advanced surface analysis techniques are beginning to offer promising opportunities to extract meaningful insights even from past, incompletely documented events of RE-induced cumulative damage. In dedicated experiments, progress is being made in diagnosing the characteristics of REs impacting instrumented in-vessel components. For example, calibrated fast thermocouples are being used to better quantify RE heat fluence, and embedded dosimeters are being implemented to help constrain incoming RE energy and pitch angle.

Concluding remarks

The study of brittle PFC RE impact is important for predicting possible RE damage to future brittle in-vessel components and for validation of physics models, which may be extended to metallic components. Across many machines, a clear hierarchy of damage is observed, ranging from no observable damage at low heat fluences, to surface morphology changes at medium heat fluences, to explosive dust release at high heat fluences. A wealth of information is available in present experiments, and future work will attempt to provide more quantitative measurements of brittle surface damage to provide better constraints on RE impact damage modeling. This work is expected to benefit RE damage modeling on W by first allowing model validation in the simpler no-melt-flow situation.

4. RE-induced damage of metal PFCs

M De Angeli[1], R Granetz[2], C Reux[3] and T Tang[4]

[1]Institute for Plasma Science and Technology—CNR, Milan, Italy
[2]MIT PSFC, Cambridge, MA, United States of America
[3] IRFM, CEA Cadarache, F-13108 Saint-Paul-lez-Durance, France
[4]Institute of Plasma Physics, Chinese Academy of Science, Hefei, People's Republic of China

Status

*Alcator C-Mod.*Regarding REs in Alcator C-Mod, a distinguishing feature was that despite having relatively high, up to 2.0 MA, plasma current, disruptions *never* generated relativistic RE beams or RE plateaus. A possible explanation for this implicated C-Mod's relatively small size [114]. Nevertheless, REs occasionally occurred during plasma startup, sometimes continuing through ramp-up and into flattop, or continuing into disruptions (but not generated by those disruptions), so damaging events did occur. RE beams could also be generated during the discharge flattop by purposely reducing the density, so-called 'quiescent REs'. This prescription allowed for controlled studies of synchrotron emission [115], and E_{crit} [116], the minimum electric field required for electrons to runaway.

Alcator C-Mod's molybdenum tile first wall saw its share of melt damage over its lifetime due to RE impacts. C-Mod's first wall was not actively cooled, so there was no risk of coolant release, just melt damage, which had little or no effect on tokamak operations. However, the worst RE event did not involve the tiles on the first wall, but rather the signal cables of C-Mod's SXR tomography arrays, see figure 12. These cables had a robust stainless steel cladding, and were located in an area that was thought to be protected from plasma contact. An unusual plasma discharge occurred, which was dominated by REs right from the beginning of the startup, and it is likely that all 0.6 MA of plasma current was being carried by REs. The plasma disrupted without warning, and a visible camera viewing the opposite side of the machine from the SXR arrays recorded a huge spray of glowing hot molten droplets emerging from behind the central column. Half the channels in one of the SXR arrays instantly went dead at that moment. But even worse, it took several days of discharge cleaning and plasma attempts before normal plasma operation was re-established.

FT Upgrade (FTU). FTU was a full metallic, cryogenic, high-magnetic-field tokamak with molybdenum-based alloy (TZM) external poloidal and internal toroidal limiters [117]. Generation of highly energetic RE beams was often observed during both start-up/steady state phases and disruptions. Typical values of RE energies and currents in FTU were 15–35 MeV and 150–230 kA respectively [118], with incident angles (corresponding to the B field) of about 0°–20° depending on the toroidal profile of the tiles.

The most common terminal location for RE beams, generated during the start-up phase and accelerated in the stationary phase, was the midplane of the poloidal limiter, because of their outward orbit drift. Such events cause the so-called *primary localized damage* of PFCs by REs in FTU. The interaction between RE beams and the poloidal limiter is often, but not always, followed by an explosion-like event caused by the energetic RE beams dissipating their energy deeply inside the tiles bulk. In fact, the thermal shock caused by the RE energy dissipation drives material explosions leading to the ejection of fast solid dust [4, 119]. The ejected dust, of $\sim$70 μm of diameter and moving with velocities of $\sim 800\,\mathrm{m\,s^{-1}}$, hits the toroidal limiter tiles located across the vessel, almost in front of the poloidal limiter, resulting in the *secondary non-localized damage* [119]. Figure 13 shows an example of an explosive event, with release of fast debris (image (a)), along with damage induced to the poloidal and toroidal limiter TZM tiles, accumulated over several experimental campaigns.

The observed primary localized damage of poloidal tiles, exemplified in figures 13(b) and (c), include: (i) deep melting and material loss up to $\sim$6 mm deep; (ii) de-attachments of several millimeters (up to 7 mm) thick layers; (iii) generation of millimeters long intergranular cracks on the surface and in the bulk of tiles; and (iv) recrystallization and degradation of mechanical properties of the bulk material (i.e. hardness, measured by microhardness tests along cross-section profiles of some tiles). On the other hand, the secondary non-localized damage found on toroidal tiles, see figures 13(d) and (e), concern: (i) formation of craters, $\sim$100 μm of diameter and $\sim$10 μm in depth, due to fast dust impacts; (ii) cracks in the PFCs bulk; (iii) removal and migration of pre-existing co-deposited material present around the crater locations.

Figure 12. C-Mod SXR signal cables damaged by a RE strike. Several cubic centimeters of steel, copper, Teflon, and fiberglass were blasted out of the SXR signal cables.

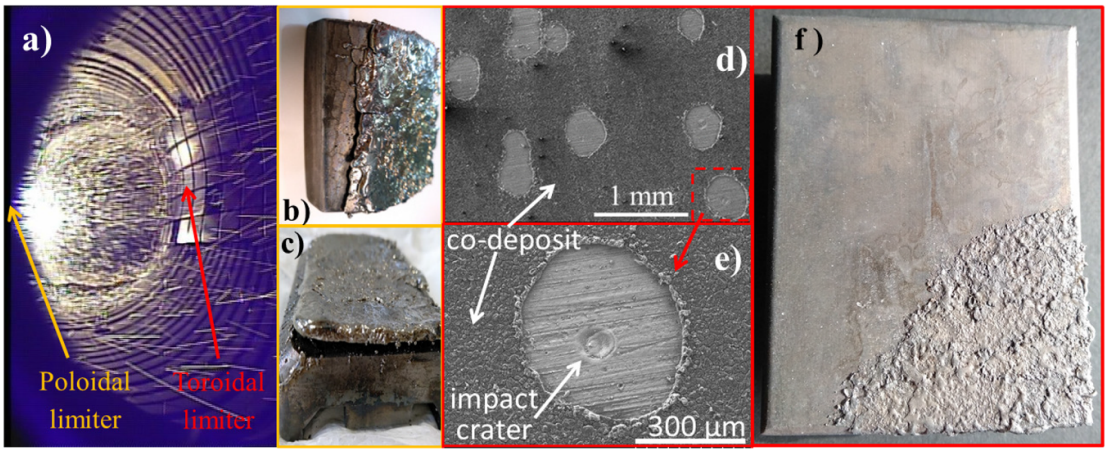

Figure 13. Example of an RE-induced explosion event in FTU. Debris trajectories recorded by VIS camera during shot 37 761 (a). Damaged Mo-based tiles from the poloidal limiter showing several mm deep melting and layer de-attachment damage, (b)–(c). SEM images of craters, found on tiles from the TZM toroidal limiter, caused by fast debris impacts, (d)–(e). Reproduced from [119]. CC BY 4.0. Example of a toroidal TZM tile damaged by RE beam terminating on the inward side showing ∼1 mm deep melting (f).

In the case of RE beams generated during disruptions in FTU, the beams tend to terminate on the inward side of the vacuum vessel [120] because the current decay is too fast to be followed by the vertical field, hitting the toroidal limiter tiles. Contrary to the outward RE beam trajectories, in this case the RE beams, having no preferential terminal point, could impact the toroidal limiter at any toroidal location. The resulting damage, about 1 mm deep and with no signs of layer de-attachment, shown in figure 13(f), is less destructive than that of poloidal tiles subjected to outward beams (compare with figures 13(b) and (c)).

FTU also had experimental campaigns with liquid tin contained in W capillary porous structures [121] wet by a layer between about 10 and 100 μm of liquid tin. These W meshes, extracted from the machine in 2019 after being exposed to hundreds of plasma discharges and to several RE beams, came out intact. Currently the work on identification of discharges that contained RE populations which could strike the meshes is ongoing though reaching an unambiguous conclusion on whether the RE beams fell on the liquid metal limiter does not appear feasible.

In general, it should be emphasized that the severe damages of the poloidal limiter tiles had almost no significant effect on tokamak operations and the damaged tiles could be replaced at the end of experimental campaigns or even during campaigns, since the poloidal limiter was removable without breaking the vacuum. Moreover, the limiter tiles in FTU were not actively cooled, thus excluding the risk of coolant accidents.

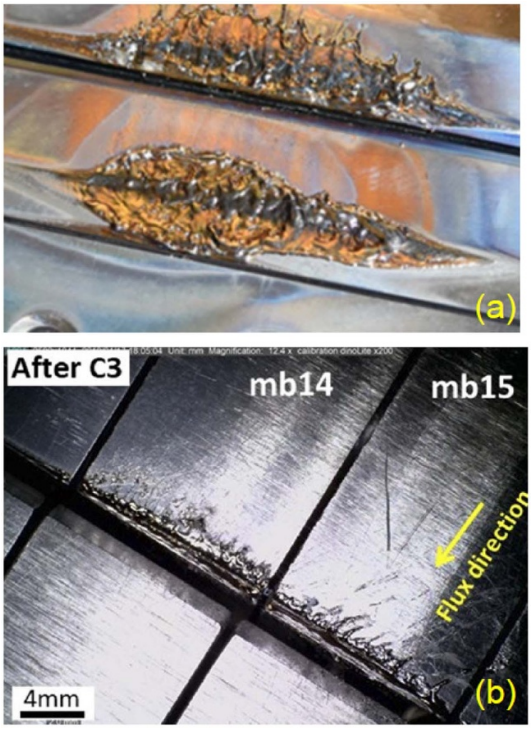

Figure 14. RE-induced damage of W tiles of WEST outer limiter (a). Courtesy of M. Diez. The trailing edge of W monoblocks on the WEST divertor hit by REs, observations after the C3 campaign (b). Reproduced from [123].

WEST. WEST is a long-pulse full tungsten machine [106]. It started out with W-coated CFC, but gradually moved to bulk W components, including an ITER technology divertor. Aside from the divertor, WEST has 18 ribs of inner wall limiters (6 groups of 3 ribs in each sector) and one outer limiter, toroidally localized. WEST, especially in its early phase with poor machine conditions, tended to generate significant amounts of REs at startup. Many of these were not controlled in the first year of operation and terminated on the inner or outer limiters [122] The W coatings hit by REs were quickly ablated, especially on the outer limiter, which is the sole point of interaction between REs and the outer wall. Post-mortem inspections of the outer limiter showed molten coatings sprayed and re-deposited around the interaction point, spread over 12 tiles, over a length of more than 50 cm in the poloidal direction [123]. The carbon substrate below the damaged tungsten coating was sometimes visible. Surprisingly, the inner limiter damage was less dramatic, with no large traces of extensive molten coating, but black markings. No systematic study of the impact features were conducted because most of the tiles accumulated dozens of impacts. The outer limiter itself suffered from about 64 impacts in that early phase, with one leading to the quench of a superconducting coil through gamma/neutron heating generated by the RE beam impact [56, 122, 124]. Ejecta from the impact point were seen on almost every impact, with some particles large enough to bounce several times on the lower divertor or the baffle before cooling down. The damaged limiters did not prevent the operation of the tokamaks, and if they had a deleterious effect on operations, then it must have been a very slow and mild degradation because it went unnoticed.

A few more impacts were recorded on the outer limiter after its transition to bulk tungsten [107]. Splashed molten pools on the limiter W tiles are depicted in figure 14(a). The WEST divertor took much fewer visible hits since the beginning of WEST operations. A single impact was recorded in the first phase of WEST operations [123] from 2017 to 2020. The tungsten tile, shown in figure 14(b), reached melting temperatures on its trailing edge, as expected from the RE beam geometry. About five RE impacts were recorded on the divertor in the C7 campaign, again on trailing edges [125] and with strong toroidal asymmetries, similar to what is shown in section 2 addressing damage to brittle PFCs on WEST. In all cases, clear traces of displaced liquid tungsten are visible in the post-mortem analysis over a radial length of about 3.5 cm [107], but did not cause significant operational problems. Most of these impacts were not noticed during operations.

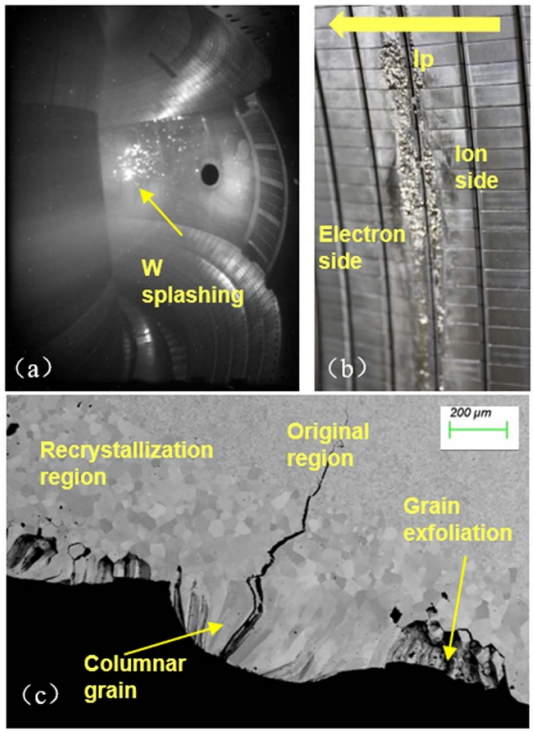

Figure 15. RE-induced damages in EAST main limiter. (a) Hot spot and W splashing viewed by CCD camera; (b) surface morphology of melting main limiter and (c) cross section morphology of the melting region.

EAST. EAST is a fully superconducting tokamak with actively water-cooled tungsten–copper (W/Cu) PFCs for both the divertors and main limiter [126]. As the closest PFC to the plasma at the low field side, the main limiter serves for absorbing and exhausting heat flux from the scrape-off layer to protect diagnostics and antennas during plasma operation. Consequently, interactions between plasma and main limiter occur frequently, predominately induced by REs during the beginning of each EAST campaign, particularly when REs are lost in disruptions. One of the examples is presented in figure 15, showing RE-induced tungsten splashing during disruption, as monitored by CCD camera, along with the resulting surface morphology of the molten tungsten limiter.

In EAST, RE currents have been typically measured in the range of 100–200 kA, with maximum energy reaching approximately 14 MeV. The sudden spike in HXR signal coincides with a sharp increase in temperature of the main limiter. Simultaneously, a hot spot appears, which eventually leads to W splashing, suggesting damages on the main limiter are predominately induced by REs. The splashed W material is ejected in all directions, reaching speeds of several tens $\mathrm{m\,s^{-1}}$ [127].

Significant melting of the main limiter is found after 2023 EAST autumn experimental campaign, as seen in figures 15(b) and (c). Both damages were found on ion side and electron side, as noted in the direction of plasma current and in opposite direction in figure 15, however, more severe melting on electron side further confirmed that damages are predominately caused by REs. Cross-section morphology analysis reveals three distinct grain layers from the molten surface to deep region: columnar grain, recrystallization region and original grain respectively. The depth of columnar grain typically ranges from 100 to 300 μm, and the depth of the recrystallization region is of comparable depth. The grain distribution suggests a sharp temperature gradient, from the surface (>3695 K) to the bottom of recrystallization region (>1473 K), within several micrometer's region impacted by REs. The presence of columnar grain indicates near-surface melting of tungsten, as material tends to form columnar grain when transient heat fluxes are high enough to induce melting [127].

Other machines. Other noticeable machines equipped with metal PFCs are AUG and KSTAR. In over a decade of dedicated RE beam experiments [96, 128, 129], and several cases of unintentional RE beams, so far the AUG team has not found any clear evidence of significant RE damages of PFCs. Nevertheless, a dedicated investigation on RE-material interaction is planned.

KSTAR replaced the carbon tiles in their lower divertor with tungsten tiles in 2023, and to date they have completed two plasma campaigns with the tungsten lower divertor. No damage due to REs has been observed so far, and in fact, REs are rarely seen, even during disruptions. This lack of disruption-generated REs is reminiscent of the experience on Alcator C-Mod, as mentioned previously.

Current and future challenges

Although present-day metal machines are able to continue operating after one or more RE strikes, future machines such as ITER, ARC, or DEMO will have active cooling structures buried in their PFCs, which could potentially be compromised by an RE impacts causing deep energy deposition. This could have major implications, such as forcing reactor operations to cease until repairs are made. This is a strong motivation to better understand the phenomena involved in the interaction of REs with metallic materials in order to characterize the impact geometry, i.e. in terms of the incident angle, toroidal symmetry, deposition area and especially energy deposition depth. This also exemplifies the need to investigate and develop methods to robustly avoid or mitigate RE, such as the passive REMC that will be installed in SPARC [130].

In dedicated investigations on the interaction of REs with PFCs, the main challenge is twofold. First, generation of controlled RE beams with known parameters is needed in order to provide input for the modeling of the energy deposition. Second, the beam should strike a precisely predicted point where an instrumented tile (a tile with embedded detectors) is located to enable measurements of various loading characteristics. In fact, the main concern in carrying out such activities in tokamaks is the safety issue related to the risk of damage from uncontrolled RE beams striking undesired locations.

Another issue, less harmful but still deserving further investigation is secondary non-localized damage in the surrounding PFCs due to the impacts of fast debris released upon explosive RE beam-PFCs interaction events, and the related dust generation problems.

Further RE experiments are planned on AUG and WEST tokamaks, mostly centered on RE mitigation through the benign termination scenario [58] but also first dedicated RE-induced damaged exposure will take place in 2025. In particular, one of the WEST inner bumper tiles has been equipped with thermocouples to better diagnose the deposited energy. In AUG, the upcoming experiment will have an instrumented W sample which will be exposed by using the mid-plane manipulator system.

Concluding remarks

It is known that the generation of RE beams and their frequency depend on plasma configuration and size [38] and an infrequent generation of RE beams is common in present-day tokamaks, with the exception of startup REs being often observed in poorly conditioned machines. This trend is confirmed by the described metal machines. All metal tokamaks in this section have shown impacts reaching melting temperatures with splashing as seen from post-mortem analysis. High speed ejecta have also been observed on some of them, with secondary damage. Toroidally and poloidally localized impact damage is also a common feature of all observations.

Generally speaking, the positive lesson learned from metal machines is that the damage to metallic components by RE does not inhibit tokamak operation as long as no coolant is released. The situation may be different on larger machines with higher currents. RE beams could still cause major operation problems if they hit recessed components such as signal cables.

Overall, studies on RE-metal interaction are in their infancy and are ongoing on several machines. These investigations are needed to predict and prevent serious damage in future devices, which could stop their normal operation in case of severe damage.

5. RE diagnostics

O Ficker[1], E Hollmann[2], U Sheikh[3] and S A Silburn[4]
[1] Institute of Plasma Physics of the Czech Academy of Sciences, Prague, Czech Republic
[2] Center for Energy Research, University of California—San Diego, United States of America
[3] Swiss Plasma Center, École Polytechnique Fédérale de Lausanne, Switzerland
[4] UKAEA, Culham Campus, Abingdon, OX14 3DB, United Kingdom

Status

The RE diagnostics is a wide area of research at the intersection of high temperature plasma diagnostics and diagnostics of relativistic particle effects. Various methods are employed to diagnose the properties, mainly energy distribution, pitch angle and (current) density of REs in the tokamak. As the RE diagnostics in general were covered in recent overview publications [38, 131] this section is focused on the means of RE *impact* diagnostics—red boxes in figure 16. Summary of such diagnostics in different machines is provided in table A1 in Appendix A.

IR thermography. IR imaging is a valuable diagnostic for measuring the spatial structure of heat loads on PFCs [132–134], and is widely available on many tokamaks. For RE studies, IR imaging has also found use for study of in-plasma RE beam structure through measurement of synchrotron emission [135–138], and this application is being considered during the design process of IR diagnostics for near-future devices such as SPARC [139]. IR imaging of PFC surface temperature excursions following RE-wall impacts was first reported from JET, where it showed that RE impact on the upper dump plate appeared to preferentially heat tile leading edges [76]. Similar IR imaging of RE impacts have since been obtained in other tokamaks including TCV [96], AUG [96], DIII-D [140] and COMPASS [102]. Fitting of interpretative models to the measured time-dependent PFC surface temperatures has been used to estimate the energy deposition densities in RE-wall impact events, allowing quantification and characterization of the relative severity of impacts [137, 141]. The ability to directly observe the spatial distribution and, more recently, also to quantify the heat deposition, has enabled the observation across several devices that RE beams accompanied by a hydorgenic background plasma tend to have a significantly (several times) larger poloidal wetted area than RE beams accompanied by high-Z (heavy impurity), with correspondingly lower heat deposition density [40, 96, 122]. IR imaging provides not only accurate information on position of hot-spots due to RE-wall interaction but is also capable of detecting heated material ejected from the impact site with more sensitivity than visible cameras (at lower temperature). It thus serves as a useful diagnostics to relate findings from post-mortem analysis of PFCs and wall inspections with specific RE-wall impact events as well as to study the large scale structure and symmetry of impacts. In principle, the measured surface temperature spatial and temporal distributions can be useful to benchmark RE-wall impact modeling, however uncertainties in the interpretation of the IR imaging, as described below, make detailed comparisons challenging.

An overview of challenges involved in interpretation of IR images of RE-wall impacts was presented previously [38]. Well-known challenges for quantitative analysis of IR imaging even for steady-state plasmas include surface morphology [142], reflections [143] and volumetric emission of IR light by the plasma, all of which are exacerbated during RE experiments. Surface morphology role becomes particularly important for strong impact events where surface changes, e.g. by very rapid melting and resolidification of metal PFCs, might be significant. This introduces large uncertainties in the wall surface profile and emissivity evolving on the same timescale as the desired measurement, potentially distorting the time history of the measured temperature. Application of multi-wavelength IR imaging [138, 144, 145] may be able to help address this challenge, however such systems are not yet common on existing devices and likely will still suffer uncertainties in such a complex measurement environment. Synchrotron emission, while enabling other diagnostic techniques as referenced above, is an additional very strong source of contaminating volumetric emission and associated reflections when considering wall temperature measurements. For example during recent RE experiments on JET, the radiance in the 3–3.5 μm wavelength band when directly viewing the synchrotron emission was typically several times the radiance emitted by a Be surface at its melting point, making the surface temperature measurements barely possible. To some extent, this can be mitigated due to the imaging nature of the diagnostic, identifying suitable lines of sight in the image which can be used as a measure of the unwanted signal to be subtracted, and by comparing the time variation of different image regions to separate contributions to the IR signal from different effects, as was done in [137, 141]. The significantly higher dynamic range requirements resulting from these constraints are met by the current IR cameras digitized at 14-bits.

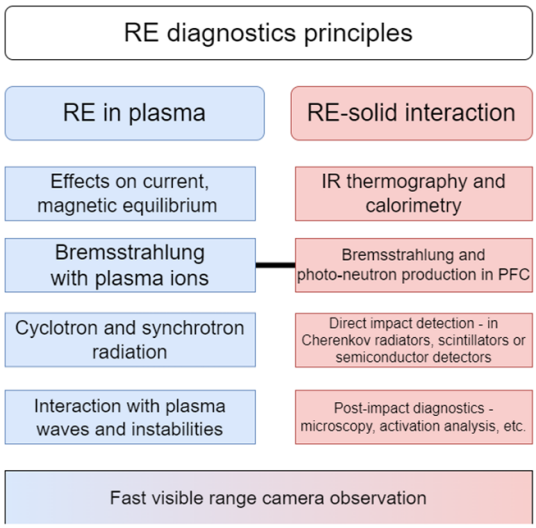

Figure 16. The RE diagnostics classification. Principles highlighted in red are covered in this section.

Figure 17 illustrates the results of IR analysis of RE impact on the DIII-D divertor shelf where these challenges have been taken into account [141]. Figure 17(a) shows an IR image of the lower divertor shelf of DIII-D during an RE-wall strike. Time decay analysis is used to isolate the RE heat fluence, giving a map of the RE heat fluence, figure 17(b), and removing the plasma line emission. The time history of a single point on the image is shown in figure 17(c). The initial plasma line emission (blue curve) is removed from the analysis. Fitting the resulting time decay (black dashed curve) can give the RE heat fluence. This time decay analysis method cannot accurately separate RE kinetic energy and pitch angle, and future techniques need to be developed to remove this degeneracy. The IR imaging discussed above was done in the 'mid-IR' imaging range of 3–5 μm; it has not been investigated yet to what degree changing imaging wavelength range could benefit RE impact diagnosis. For example, moving to longer wavelengths could reduce sensitivity to plasma line emission but at the cost of reduced frame rate and spatial resolution.

The timescale for RE-wall impact is usually quite short ($\sim$1 ms), which can be faster than the frame rate of the IR imaging, complicating the analysis due to the fast dynamics not being fully resolved. A further interpretation challenge is due to the volumetric nature of the heat deposition, which has to be reconstructed with the aid of modeling, since the diagnostic can only measure the surface temperature.

Calorimetry. Calorimetry in tokamaks is a critical diagnostic technique used to measure the energy deposited on PFCs, where they can directly intercept the plasma or RE beams. Calorimeters are typically designed as thermal sensors embedded in tiles that measure temperature changes and infer energy deposition in the volume. The simplicity of these devices can allow the installation of numerous sensors in a tokamak, providing spatial information on the energy distribution. The use of such systems has been demonstrated on TEXTOR, COMPASS, JET, DIII-D, AUG and TCV, where calorimetry has provided valuable insights into energy deposition and the spatial characteristics of RE beams. Experiments on TEXTOR, COMPASS and DIII-D developed protruding calorimetry probes to make direct measurements of impact energy deposition. In TEXTOR, a typical RE plateau with a current of 100 kA resulted in a deposited energy of 30–35 kJ, which represents a magnetic to kinetic energy conversion of 30% [113]. The deposited energy was found to vary linearly with RE current. Similarly, deposited energies of 2–12 kJ were measured in COMPASS at RE currents in the range 40–130 kA and were found to scale with the loop voltage and amount of injected impurities [102].

In DIII-D experiments, RE impact calorimetry has been performed with intentionally inserted domed graphite limiter heads. These heads were inserted during dedicated RE-forming disruptions using the DIII-D material exposure system (DiMES) which can insert samples into the lower divertor floor of DIII-D [146]. The graphite dome protruded 1 cm above lower divertor floor. A thermocouple is used to measure temperature inside the domed head (forming a calorimeter system), while a shunt resistor and current monitor lead are used to measured current flowing from the limiter head into vessel ground. Dosimeter chips are used to monitor the single-shot HXR fluence distribution inside the limiter. These heads were intentionally struck with high current (500–600 kA) hydrogenic RE plateaus and heat loads of order 1–10 kJ were measured. This large variation was attributed to the toroidal phase of the RE final loss MHD varying from shot to shot. Work on AUG, JET and TCV is on-going within the

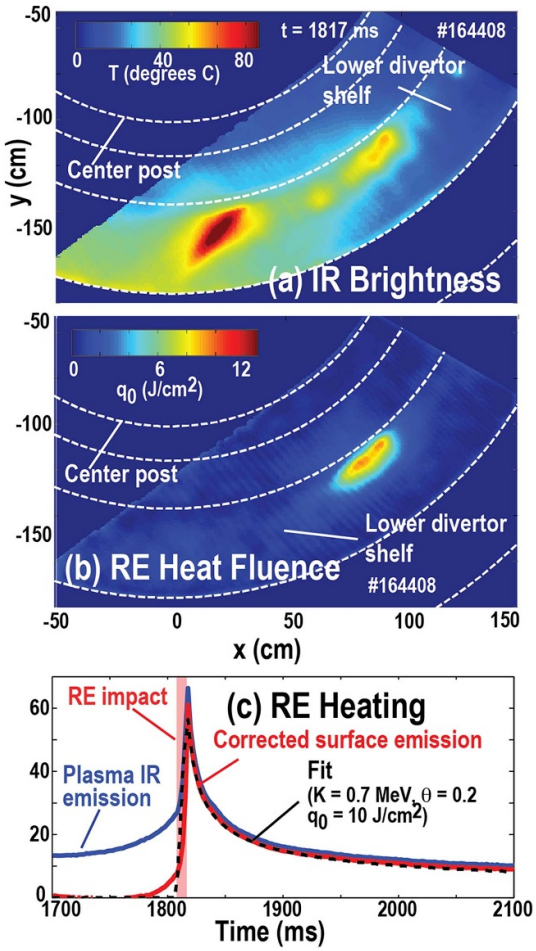

Figure 17. IR image of RE impact on lower divertor shelf of DIII-D (a), RE heat fluence extracted from IR image (b) and time decay analysis of single pixel to remove IR plasma emission and estimate RE impact heat fluence (c). Reprinted from [141], with the permission of AIP Publishing.

RE benign termination database (ITPA MDC-23), where toroidally separated thermocouples embedded in tiles are being compared with IR thermography measurements to infer heat flux and toroidal asymmetries [96, 98].

X-rays at RE impact. As the impact of MeV-range electrons onto a solid surface is accompanied by very intensive bremsstrahlung radiation in the HXR and SXR spectral regions, various detectors of such radiation are instrumental in assessing the time evolution, duration or intensity of the impact and estimating the energy of the RE population. The radiation is also produced during interaction of RE with plasma ions, mainly impurities, however, unless very large impurity densities are reached, the HXR intensities from the RE-PFC interaction are dominating, especially within fast loss events. This radiation is typically measured by uncollimated or partially collimated HXR monitors (HXRMs) and spectrometers based on suitable fast scintillators with a photo-multiplier. $LaBr_3$(Ce) or $CeBr_3$ are the most common scintillation crystals, significantly surpassing e.g. previously favorite NaI(Tl) in scintillation decay time. Such systems are in use at AUG [147], TCV [148, 149], JET [150], COMPASS [151], DIII-D [152], J-TEXT [153] and many other machines. At JET [154], DIII-D [155] and WEST [156], collimated multi-LOS systems are used as well, however these are typically dedicated to measure RE–ion interaction bremsstrahlung and not RE-PFC interaction. The comparison of steady state and termination relative HXR flux together with approximate measurement of toroidal asymmetry of HXR flux during the impact at DIII-D is shown in figure 18.

The HXR spectrometers provide energy resolution via pulse-height analysis and the RE energy may be inferred from the HXR spectra using regularization. This is however an inverse problem based on two subsequent processes, thus only limited information can be retrieved—general shape of the spectra and maximum or average energy with significant error bars. Furthermore, the potential of these methods is significantly suppressed by the high flux at termination leading to pile-ups.

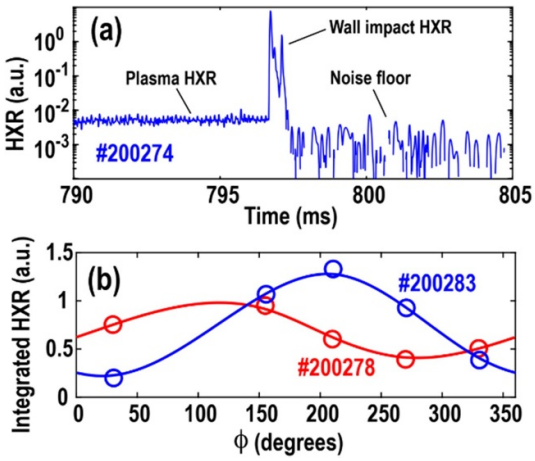

Figure 18. HXR time trace showing steady plasma emission initially and then a huge spike at the main RE impact event (a). Integral over the wall impact spike as a function of outer midplane detector toroidal position with approximate fit (b). The two pulses differ in the phase of applied $n = 1$ magnetic perturbation during RE beam termination, in #200 283 the phase was 180°, in #200 278 it was 60°.

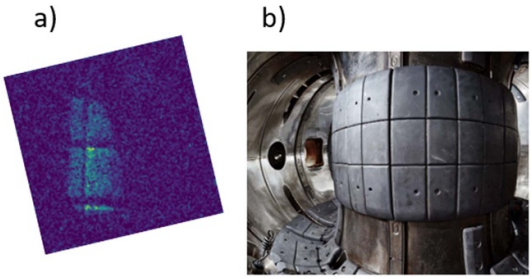

Figure 19. SXR image of start-up REs impacting HFS carbon limiter tiles of COMPASS as recorded by TimPix3 with lead pinhole (a). Interior of the COMPASS vacuum vessel for reference of the HFS tiles layout (b). Reprint with permission from [161].

At COMPASS and Golem [157], also high pixel resolution extended range SXR matrix chips derived from TimePix3 [158] were tested [159–161] for direct imaging of the impact locations, in an extended dynamic range or in a Compton Camera set-up. It is possible to detect the impact of the start-up REs on the high field side tiles, as shown in figure 19), however the small pixels absorb only a minor part of the photon energy for $E_{\mathrm{HXR}} > 50\,\mathrm{keV}$.

The diagnostics systems are subject to challenging design decisions, mainly in terms of collimation and scintillator size, balancing the count rate range and energy range/resolution. The flux of photons at the detector position may vary across more than 10 orders of magnitude depending on the scenario, thus multiple detectors with very different sensitivity are often preferred.

Photo-neutrons. The photo-neutrons as a product of bremsstrahlung-generated x-rays interacting with suitable nuclei can also be used for diagnostics [51]. As photo-neutrons and PFC activation are covered in section 9, we only mention the most important advantages for RE impact diagnostics; (i) existence of energy threshold for given reaction provides energy discrimination for the RE population, (ii) due to the scattering of the neutrons before detection, the measurement of photo-neutrons can be considered less depended on the impact location than HXR detection, which is useful for a global comparison of impact events. The role of photo-neutron detection in comparison with other diagnostic means has been investigated, e.g. in [131].

Cherenkov probes and other direct RE detection methods. The direct detection methods, i.e. those where the energy of REs is fully or partially deposited in the detector volume are very attractive, however their applications are limited. The advantages are precise spatial localization and no intermediate steps in the RE measurement process. The main disadvantage is the risk of fast deterioration of the detector due to exposure to REs. Cherenkov detectors are based on production of Cherenkov radiation in diamond or similar radiator covered by metallic layers to provide energy thresholds for impacting REs. Typically three channels with different energy thresholds in the range of energies 50–300 keV are used. Such

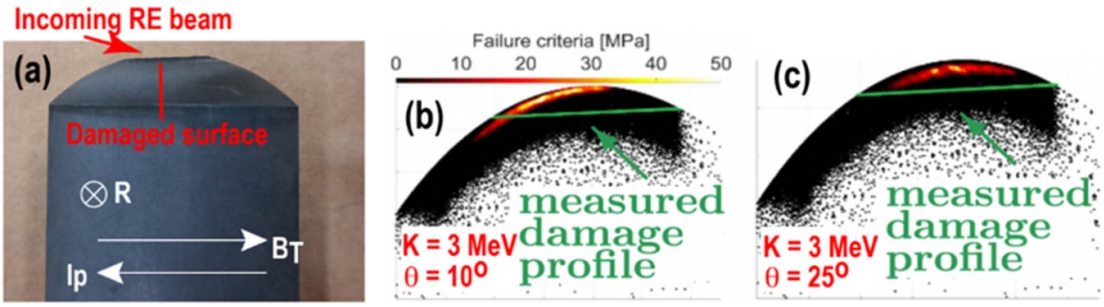

Figure 20. RE impact on graphite limiter as a pitch angle θ_p diagnostics: graphite limiter damage from RE impact (a) and modeling the graphite material failure, (b) and (c) . The model assumed REs with a single initial kinetic energy and pitch, the best matching parameters are $E \approx 3$ MeV and $\theta_p \approx 25°$. Reproduced from [4]. CC BY 4.0.

detectors were applied at FTU [162], COMPASS [163], TCV [164], ISTTOK [165], Tore Supra [166] and other machines. Due to the given range of energy thresholds in hundreds of keV, the Cherenkov detectors are best suited for measuring start-up REs or TQ RE seed losses. Similarly, scintillation detector directly exposed to RE flux or series of probes consisting of conversion layers producing bremsstrahlung and scintillators detecting it are utilized to inspect the properties of RE population directly. Such methods were applied at TEXTOR [111] and concepts developed, e.g. at Golem [167]. Various silicon-based detectors can also be used for direct detection of lower energy RE population [168]. In principle, various electric probes, floating or biased can be also used to detect electrons of high energy. A planar electric probe was embedded in the COMPASS calorimeter [102]. The pitch angle of the RE population can be estimated by the direct detection methods using suitable geometry of the detectors, e.g. adding various collimators or entrance slits that allow only RE with specific pitch angle to reach the detector volume.

Post-impact damage analysis. The impact locations on various PFCs or diagnostics are analyzed by the means of optical microscopy [102, 119] and scanning electron microscopy [119] in both impact surface view and cut through the sample. Various types of damage have been observed after the impact, including craters and re-deposition structures. The analysis of the chemical composition is performed using EDS, x-ray photoelectron spectroscopy (XPS) and other methods to investigate layer transitions in the PFC and oxidation of the impacted surface. Furthermore, the impact pattern on special surface shape evaluated post-mortem can be used together with modeling to investigate the parameters of RE population, e.g. the pitch angle distribution, as shown in figure 20.

Current and future challenges

Challenges common for all the discussed diagnostic groups concern: (i) recognition of distorted signal or signal contributions from different phenomena (e.g. reflections, synchrotron radiation effect on IR and visible range cameras, background HXR radiation) (ii) enhancement of the spatial and temporal resolution (iii) enabling diagnostics performance in harsh environment (radiation hardness), of crucial importance to ITER and other nuclear-grade devices. These challenges are being addressed by modeling and synthetic diagnostics as well as by ever-increasing performance of digitizers and development of novel diagnostics designs. For diagnostics in ITER see section 10.

Concluding remarks

Typically, different machines excel in different diagnostics systems. The progress in commercial detector performance (IR and visible range cameras, scintillators) further pushes the boundaries of RE-PFC interaction diagnostics. The synthetic diagnostics approach applied to combine several different diagnostics methods is the most promising way to increase the relevance and accuracy of physical parameter inference and connection with the modeling.

6. Models for the characteristics of the RE beam prior to the impact

M Hoppe[1], B Breizman[2], V Bandaru[3] and G Pokol[4]

[1] KTH Royal Institute of Technology, Stockholm SE-100 44, Sweden
[2] Institute for Fusion Studies, The University of Texas at Austin, Austin, TX, United States of America
[3] Department of Mechanical Engineering, Indian Institute of Technology Guwahati, Guwahati, Assam, India
[4] Department of Nuclear Techniques, Budapest University of Technology and Economics, 1111 Budapest, Hungary

Characterizing the wall damage caused by REs impact requires detailed knowledge of the RE beam. This involves the beam energy spectrum and the impact angles that depend on the pitch angle distribution before impact. This section summarizes the current status of simulations aimed at providing such a detailed characterization of the RE beam and some of the associated challenges. More comprehensive reviews of RE physics can be found in [38, 169].

Status

The RE beam characteristics prior to impact are determined by the full history of events occurring from the point of initial RE generation up to the impact. Generation of REs requires the parallel electric field $E_{\|}$ to exceed a critical value, E_c, and so REs are normally found in phases where the plasma current changes in time. Of particular concern to reactor-scale tokamaks are REs generated during startup/ramp-up and disruptions, with the latter receiving the most attention in literature. Although the plasma environment during startup and disruptions has some similarities, specialized models tailored to the specific conditions are usually employed. In the modeling of both phases, there is a need to account not only for the kinetics of the REs but also for the evolution of the background plasma and the way in which it is influenced by the REs. In many situations, REs carry a significant fraction of the plasma current and therefore strongly influence the electric field evolution and current-driven MHD instabilities. REs can also impact, or even dominate, the energy balance and ionization rate of the plasma, such that a reliable RE beam model must cover these effects.

Two complementary modeling approaches are used to gain predictive insights. The kinetic approach deals with an equation for the energy and pitch angle distribution function f_e of REs, namely,

$$\frac{\partial f_e}{\partial t} = -eE_{\|}\frac{\partial f_e}{\partial p_{\|}} + \nabla_p \cdot (\boldsymbol{F}_{\mathrm{rad}} f_e) + C_{\mathrm{FP}}[f_e] + C_{\mathrm{ava}}[f_e] + Q_e[f_e]\,. \tag{1}$$

Here, $E_{\|}$ is the electric field component parallel to the magnetic field, and $\boldsymbol{F}_{\mathrm{rad}}$ denotes the reaction-force due to bremsstrahlung [170–172] and synchrotron radiation [99, 173]. The Fokker–Planck collision operator $C_{\mathrm{FP}}[f_e]$ must be relativistic [174, 175], and a test particle approximation is commonly used for the electron–electron operator [176]. In the collision operator, partial ionization effects are essential for RE dynamics [45, 177–179], especially in mitigated disruptions. In contrast to thermal electrons, REs are strongly influenced by large-angle collisions causing the exponential growth [180], as described by an avalanche source term [181, 182] in the collision operator denoted $C_{\mathrm{ava}}[f_e]$ [36, 183, 184]. To describe the effect of wave–particle interactions, a quasi-linear operator $Q_e[f_e]$ is included [185–187].

An analytical solution of equation (1) is feasible under certain conditions, most notably, to assess the RE growth at constant electric field. This includes both the primary Dreicer generation [188–190] and the secondary avalanche generation [191, 192]. While analytical results provide useful estimates of the RE current and show parametric trends, there is also an early self-consistent disruption simulator GO [85, 193, 194] that relaxes some limitations of the analytical estimates [195]. Several codes have been developed for solving equation (1) directly. These include CODE [196, 197], CQL3D [198], DREAM [41], LAPS-RFP [199], LUKE [97], NORSE [200], RAMc [201], and codes in [183, 202, 203]. Modules also exist for codes ASCOT [204], JOREK [205, 206] and Kinetic Orbit REs Code (KORC) [207] to solve equation (1) using orbit-following or particle-in-cell techniques.

The fluid approach, in contrast, does not describe RE pitch angle and parallel momentum, but only the RE density (n_{re}) via a rate equation of the form

$$\frac{\partial n_{\mathrm{re}}}{\partial t} + \nabla \cdot (\boldsymbol{v}_{\mathrm{adv}} n_{\mathrm{re}}) = S_{\mathrm{seed}} + S_{\mathrm{avalanche}}, \tag{2}$$

wherein advective transport and volumetric source terms dictate the RE evolution. Here, $\boldsymbol{v}_{\rm adv}$ involves the parallel advection and cross-field drifts. This evolution equation for $n_{\rm re}$ is EM coupled to the background plasma equations to form a closed set. While less accurate compared to the kinetic approach, the advantage of the fluid approach is in enabling also 3D simulations over long timescales (see section 7) in realistic geometries. An RE fluid model was implemented in JOREK [208], M3D-C1 [209], NIMROD [210], EXTREM [211], GO [85, 193, 194], DREAM [41], among others. These studies enable predictions not only of current driven instabilities with REs, but also address the effects of plasma vertical motion, impurity and deuterium injections, RE beam termination due to stochastization, etc.

The number of REs is typically much smaller than the total number of plasma electrons since most electrons cannot enter the runaway regime when the driving electric field is below approximately 21% of the Dreicer field [188]. However, being much faster than the bulk electrons, REs can carry a significant part of the total plasma current in a tokamak. They can reach relativistic energies if the electric field exceeds the Connor–Hastie field [189], which is smaller than the Dreicer field by the factor T/mc^2. In the relativistic regime, the current density of REs is $en_{\rm re}c$, implying that a RE density of $n_{\rm re} = 2\times10^{16}\,{\rm m}^{-3}$ is sufficient to carry a current density of $1\,{\rm MA\,m}^{-2}$. When the driving field exceeds the Connor–Hastie field, the RE energy gain is not limited by Coulomb collisions, but synchrotron losses and pitch-angle scattering. The scattering rate increases as the pitch-angle distribution narrows during electron acceleration, and synchrotron losses increase accordingly for higher electron energies.

REs are ubiquitous in startup plasmas during electrical breakdown, but their current usually remains small by the time the plasma heats up and becomes a good conductor [38, 212, 213]. They then gradually dissipate because the low loop voltage is unable to support them in the multi-keV range. A sufficiently long time of discharge shut-down in regular operational regimes can easily prevent reoccurrence of REs, but it becomes a clear danger in case of fast emergency shut-down. Copious production of REs can then be powered by the large energy of the poloidal magnetic field [38].

When $E_\parallel \gg E_{\rm c,eff}$, the characteristic time scale of the avalanche growth is typically much shorter than the lifetime of the plasma current [214]. Thus, $E_\parallel$ relaxes quickly to its threshold level when REs start to dominate the current. However, REs cannot last long if $E_\parallel \ll E_{\rm c,eff}$ as Coulomb friction would slow them down. Consequently, $E_\parallel \sim E_{\rm c,eff}$ is required for a long-lasting RE population [215].

RE generation is highly sensitive to the background plasma properties. Consequently, quantitative modeling of REs must cover this aspect [85, 193, 216, 217]. The Dreicer and hot-tail mechanisms of primary RE production depend significantly on the electric field, electron temperature and density [188, 218]. The secondary avalanche mechanism is also sensitive to the ionization state of the plasma [192].

Models for the plasma heat content have similar forms for startup and disruption studies [41, 205, 219–221], with a rate equation for electrons

$$\frac{\partial W_e}{\partial t} = (P_{\rm ohm} + P_{\rm re}) + \sum_i P_{ei,\rm coll} - (P_{\rm line} + P_{\rm rec}) - P_{e,\rm transp}, \tag{3}$$

and equations for each ion and neutral species i

$$\frac{\partial W_i}{\partial t} = \sum_j \left(P_{ij,\rm coll} - P_{ij,cx}\right) - P_{i,\rm transp}. \tag{4}$$

Here, $P_{\rm ohm}$ denotes Ohmic heating, $P_{\rm re}$ collisional heating of the background plasma by REs, $P_{ij,\rm coll}$ collisional thermalization between species i and j, $P_{ij,\rm cx}$ charge exchange processes, $P_{\rm line}$ line radiation losses, $P_{\rm rec}$ radiation losses due to recombination and bremsstrahlung, and $P_{e/i,\rm transp}$ the power loss due to spatial transport. The term $P_{\rm re}$ is often negligible during startup as well as in an early phase of disruptions due to the small RE content. In post-disruption RE termination scenarios, the term $P_{i,\rm transp}$ for neutrals is expected to play an important role [96].

The ion composition of the plasma is governed by a particle balance equation of the form

$$\frac{\partial n_i^{(j)}}{\partial t} = S_{i,\rm ioniz}^{(j)} + S_{i,\rm rec}^{(j)} + S_{i,\rm ioniz,re}^{(j)} + \sum_j S_{ij,\rm cx}^{(j)}, \tag{5}$$

where $n_i^{(j)}$ is the density of charge state j of species i, $S_{i,\rm ioniz}^{(j)}$ and $S_{i,\rm rec}^{(j)}$ are the particle production/destruction rate due to ionization and recombination, $S_{i,\rm ioniz,re}^{(j)}$ is the production rate due to RE impact ionization, and $S_{ij,\rm cx}^{(j)}$ is the production/destruction rate due to charge-exchange processes. In post-disruption RE beam termination scenarios, molecule formation can play an important role in particle

and power balance, in which case the ionization and recombination terms should also be interpreted as molecular association/dissociation rates [94, 219, 222].

Current and future challenges

Multi-scale modeling. REs inherently span across several orders of magnitude in energy. Thermal electrons, with single-digit eV energies, can undergo large-angle collisions with REs and find themselves in the runaway range where they can be accelerated to hundreds of MeV. Simulations must cover electron dynamics across this entire energy range. This is further complicated by the sensitivity to critical energy value, above which electrons accelerate freely, which can vary significantly in a self-consistent simulation. One promising approach to addressing this issue is the fluid-kinetic models in which electrons are divided into different energy regions treated either as a fluid or kinetically [41, 202],

Particle simulations of the RE dynamics, as conducted in, for example, [3, 206] and [140, 223], are primarily limited by the different time scales involved. In particular, disruptions exhibit an evolution in which typically a small (but important) population of seed electrons are generated on the TQ time scale, multiplied by the avalanche mechanism on the longer CQ time scale, and finally relaxed in momentum space on an even longer time scale corresponding to the remainder of the RE beam life time. While time steps in particle codes are limited by either the gyro or guiding-center motion, continuum codes are limited by the time scales over which the various RE generation mechanisms play out. At the beginning of a disruption, this is the ionization time scale for the injected material, which can require sub-microsecond time steps, while later in the disruption, millisecond time steps may be admissible.

Energy balance and impurities. The fraction of the total current carried by REs depends critically on the bulk plasma resistivity and hence temperature. For nominal ITER parameters, a 1 keV electron temperature would allow the bulk to carry the total current at an inductive field lower than the Connor–Hastie field, i.e. below the runaway avalanche threshold. At lower temperatures, REs become a substantial part of the total current. It is worth noting that in a pure hydrogen plasma a sudden drop in electron temperature in the absence of subsequent heat losses would not allow RE build-up as because the stored magnetic energy of the toroidal plasma current reheats bulk electrons faster than RE avalanching [38, 83]. The spike in the inductive field would then be short and benign, as in the plasma startup regime. However, a significant presence of impurities may prevent this reheating. Rapid cooling of bulk electrons during TQ could also result from large electron heat flux to the wall along the stochastic magnetic field lines. The energy balance of the bulk plasma has to be modeled carefully because its ambiguity translates into a high uncertainty in the bulk plasma conductivity and inductive electric field.

Near-threshold dynamics. In situations where the electric field $E_{||}$ is close to the threshold value $E_{c,\mathrm{eff}}$ required for net RE generation [214, 224, 225], several effects can play an important role in shaping the RE distribution. Such a situation arises at the end of disruptions, in the RE plateau, where REs carry the entire current. Since all primary RE generation mechanisms are inefficient in this phase, large-angle (knock-on) collisions determine the growth and decay of the RE current, with a gradual decay for $E_{||} < E_{c,\mathrm{eff}}$ [184, 215]. The time scale of the reduction of the electric field might be determined by the interaction with the wall current, as the wall times in large tokamaks approach or exceed the time scales relevant for RE beam formation. Pitch angle scattering and radiation also play an important role in shaping the distribution function in the near-threshold regime. Pitch angle scattering enhances energy losses due to synchrotron radiation [226]. Synchrotron losses and bremsstrahlung can produce bumps in the RE distribution function [99, 170, 224] when $E > E_{c,\mathrm{eff}}$, which can trigger kinetic instabilities. In disruptions, as well as in certain startup scenarios, the electric field will eventually reduce from a peak value $E_{||} > E_{c,\mathrm{eff}}$ to a sub-threshold value, causing REs to gradually lose energy via radiation. A quantitative description of this effect in reactor-scale tokamaks still remains to be developed.

RE-background interaction. The most significant RE contribution to the plasma conditions is the electrical current close to 100% of the remnant plasma current in a post-disruption plateau. The REs can also affect plasma behavior in other ways. A significant RE population may act as a dominant heat source for the system [227]. Collisions of REs with (partially ionized) atoms can enhance the ionization state of the background plasma [228–230]. Whereas models for these effects, suitable for fluid codes, have been derived, the validity of these models for post-disruption plasmas remains uncertain. In particular, models derived for high-energy weakly collisional REs miss the role of more collisional low-energy REs that could potentially enhance heating and ionization beyond predictions.

Access to benign termination. The benign termination scenario has emerged as a potential technique for safely terminating a RE beam [58, 59]. However, as has been demonstrated experimentally [96], this scenario requires secondary low-Z material injection to bring the neutral pressure to a specific range, where the plasma largely recombines and a final discharge-terminating instability is triggered. While the bounds of this neutral pressure range have been characterized experimentally on specific tokamaks, significant uncertainty remains for reactor-scale tokamaks such as ITER and SPARC. Further modeling is needed accounting for the atomic/molecular physics at play, as well as the complex interaction between REs, cold plasma with neutrals, and tokamak wall [219, 222, 230].

Control via wave–particle interactions. There are conceivable ways to mitigate the RE population via self-excited or externally driven (injected) waves [231, 232]. In the high-frequency range, REs can resonate with the electron plasma waves or whistler waves [186, 233, 234]. Both are difficult to drive from outside by antennas because they are under the cutoff frequencies of dense plasmas and subject to significant collisional damping at low electron temperatures. If attempted to affect the seed REs, such externally launched waves would heat the bulk electrons rather than impact the RE population via wave–particle resonance [235]. A plausible alternative might be to employ radiofrequency (RF) current drive [236] that may prevent RE build-up as the TQ and the resulting drop in Spitzer conductivity would not necessarily entail the high inductive electric field in the presence of RF-current drive. This motivates an effort to model the buildup of REs in the presence of the RF-current drive to assess the potential benefits of the technique for RE control [237].

Among self-excited waves, whistlers receive extensive attention [238–240]. They can enhance pitch-angle scattering of the REs, leading to the enhancement of synchrotron losses. REs excite whistlers via anomalous Doppler resonance, and the RE current must already be substantial to overcome the collisional damping of whistlers. More specifically, the minimum electron temperature for exciting whistlers by the nominal ITER current density of $1\,\mathrm{MA\,m^{-2}}$ is 25 eV [187], well above the expected post-disruption temperature in ITER. In present-day RE flat-top experiments, whistlers are easier to excite because of higher electron temperatures [239, 241] and can indeed enhance RE scattering [43] keeping the RE current at a marginal stability level [242, 243].

Losses during VDE. Disruptions in large tokamaks can involve plasma motion in a VDE, during which REs can scrape against the wall [244–246]. Recent studies found that VDE motion and consequent RE scraping can lead to a substantial loss of REs on open outer flux surfaces reducing the RE current [247–249]. Although initial considerations show some promise, more work is needed to quantify the robustness of this avalanche-reducing mechanism and validate it experimentally. This RE current dependence on the competing processes of RE avalanche and vertical motion translates into sensitivity to impurity content, direction of vertical motion (up or down), rate of current decay, etc. However, scraping induces additional wall loads, potentially negating the benefits of RE mitigation. The scrape-off effect is expected to be beneficial only when it happens while the RE population is small enough not to cause wall damage. In typical ITER upward VDE situations, including scenarios with Neon injection or flush-out, predictions by DINA [245] and JOREK [248] do not show a clear advantage, as the cumulative RE energy dumped onto the PFCs does not change considerably. More work and more accurate models are needed to verify this observation. Work is also needed to quantify the momentum-space distribution of lost REs. Since scraping coincides with the most RE generation-intense phase of a disruption, the momentum distribution of lost REs may deviate significantly from that of confined REs at the end of a disruption.

Radial transport. Radial transport has long been considered attractive as a way to prevent detrimental avalanching. Different forms of radial transport were studied, including externally induced transport via resonant magnetic perturbation (RMP) coils [250, 251], passive asymmetric coils [252–254], MHD instabilities [255, 256], and electron cyclotron waves [232, 235], among others. In support of such studies, work has also been done to relate the RE transport rate to the magnetic stochasticity [257–259]. What remains much less explored is how the naturally present radial transport arises and affects the REs.

Experimental measurements indicate that some radial RE transport is naturally present without external interference [52, 260–262], and simulations show that even moderate radial losses can reduce the number of REs generated in a disruption [259, 263]. To predict the generation of REs accurately, theoretical models for their radial transport should be developed. These can either provide values for advective and convective transport coefficients [258] or be based on developments in chaos theory [264]. To accomplish this, a better understanding of the radial transport physics is needed, specifically if transport in TQ, CQ, and RE plateau, is driven by MHD or turbulence.

Concluding remarks

State-of-the-art RE models have come a long way from early works aimed at estimating the RE number and momentum distribution in steady state. Present-day numerical tools incorporate key physics mechanisms affecting the RE behavior and background plasma self-consistently. Despite such progress, conclusive modeling of the TQ presents an outstanding challenge.

Other major open questions exist for quantitative predictions of RE properties in reactor-scale tokamaks. In particular, techniques for treating highly and moderately relativistic electrons simultaneously are required as the latter may play a crucial role in the near-threshold regime, typical of RE plateaus. Lower energy electrons couple stronger with the background plasma and can conceivably enhance ionization and heating by REs beyond present estimates.

Due to the potentially severe damage caused by even moderate amounts of REs, near-term model development should focus on potential RE avoidance and mitigation techniques, such as wave–particle interactions (including possible benefits from the RF current drive), Deuterium second injection, and RE losses during VDEs. The mechanisms driving radial RE transport in the different disruption phases are still poorly understood and remain crucial for creating robust quantitative RE distribution models.

7. Reduced RE beam dynamics and impact models

P Aleynikov[1], M Beidler[2] and J R Martin-Solis[3]

[1]Max-Planck-Institut für Plasmaphysik, Wendelsteinstraße 1, 17491 Greifswald, Germany
[2]Fusion Energy Division, Oak Ridge National Laboratory, Oak Ridge, TN 37831, United States of America
[3]Universidad Carlos III de Madrid, Avenida de la Universidad 30, 28911 Madrid, Spain

Status

The magnetic energy, $W_{\rm mag}$, of MA RE beams formed during the disruption CQ is typically much larger than the kinetic energy of the REs, $W_{\rm kin}$ (in ITER $W_{\rm kin} \sim$ MJ, whereas $W_{\rm mag} \sim$ hundreds MJ [265, 266]) so that, when the RE current is lost during the termination phase of a disruption, conversion of magnetic energy into RE kinetic energy can occur, which could substantially increase the energy fluxes deposited by the REs in comparison with the kinetic energy gain during the CQ of the disruption. The importance of this issue was first pointed out in [191], and later in [267], and experimental evidence has been reported in several devices [265, 266, 268, 269], showing that a remarkable conversion of magnetic into RE kinetic energy can indeed take place. Here, a summary of lower dimensional models used to characterize the energy balance during a disruption is presented, focusing on the fraction of the magnetic energy of the runaway plasma, which might be transferred to REs. Particle-based kinetic models are also discussed as well as the essential parameters determining the RE impact on the PFCs.

0D/1D fluid models. Simplified 0D/1D fluid models for the termination phase of the disruption have been developed [42, 246, 265] with simplistic RE kinetics, which allow to elucidate the mechanisms that govern the conversion of magnetic into RE kinetic energy, with a view to their evaluations for ITER. All of them include a coupling between models for the plasma current and the RE current evolution.

The 0D model presented in [265] consists of two coupled equations for the plasma current, $I_{\rm p}$, and the current induced in the vessel, $I_{\rm v}$, together with an equation for the evolution of the RE current, $I_{\rm r}$, accounting for the generation of REs by the avalanche mechanism, approximated by [181, 191, 270],

$$\left(\frac{{\rm d}I_{\rm r}}{{\rm d}t}\right)_{\rm avalanche} \approx \frac{e\left(E_{||}-E_{\rm R}\right)I_{\rm r}}{m_e c \ln\Lambda\, a_z}, \tag{6}$$

and the loss of REs during the termination phase, $-I_{\rm r}/\tau_{\rm d}$, with a characteristic loss time, $\tau_{\rm d}$. In equation (6), $E_{\rm R} = n_e e^3 \ln\Lambda / 4\pi\varepsilon_0^2 m_e c^2$ is the critical field for RE generation [181, 189], $a_z \equiv \sqrt{3(5+Z)/\pi}$, and $E_{||} = \eta\left(j_{\rm p} - j_{\rm r}\right)$, where $j_{\rm p.r} = I_{\rm p,r}/\pi a^2 \kappa$, a is the plasma minor radius, κ the plasma elongation, and η the plasma resistivity.

The energy transferred to the REs during the termination phase is estimated:

$$\Delta W_{\rm run} = 2\pi R_o \int I_{\rm r}\left(E_{||}-E_{\rm R}\right){\rm d}t. \tag{7}$$

Comparisons between models and several tokamak experiments (JET [80, 271], DIII-D [268] and FTU [120, 272]) suggest that the same physical model reasonably accounts for observations in present devices [265]. The conversion efficiency is found to be largely determined by the ratio of the RE loss time, $\tau_{\rm d}$, to the resistive time of the residual ohmic plasma, $\tau_{\rm res}$, increasing with $\tau_{\rm d}/\tau_{\rm res}$. The avalanche generation of REs increases the conversion of magnetic energy into RE kinetic energy, particularly for large enough RE currents and long lasting termination phases.

1D models [42, 266] taking into account the evolution of the plasma and RE current density profiles have also been applied, using a simple cylindrical plasma geometry, in which the evolution of the plasma current density ($j_{\rm p}(t,r)$) is calculated solving the current diffusion equation [42], together with an equation for the RE current density ($j_{\rm r}(t,r)$) similar to the 0D model equation. The energy deposited on the REs,

$$\Delta W_{\rm run} = \int_{\rm termination} {\rm d}t' \int j_r\left(E_{||}-E_{\rm R}\right){\rm d}v, \tag{8}$$

is found to increase in comparison with the 0D calculations as the RE current density profile is expected to be more peaked in the plasma center than the pre-disruption current density profile [42, 273], which will enhance significantly the growth of the RE population by avalanche in the plasma center during termination and lead to substantial energy conversion [42].

In ITER, RE beams are expected to be vertically unstable and, hence, when the plasma hits the wall, the scraping-off of the RE plasma occurs and the current is terminated [246]. A simple 0D model which mimics the plasma surrounded by the conducting structures [274], including self-consistently the vertical plasma motion and the generation of REs, has been used for an evaluation of the RE formation and termination during disruptions [246]. The model approximates the plasma–wall system by a set of three parallel thin circular coaxial rings of radius R_0. The bottom and top conductors carry currents I_1, I_2, respectively, and represent the current in the conducting wall, while the middle conductor represents the plasma current, I_p, which can move vertically. The model also includes a static external magnetic field created by two constant circular currents, I_e. Hence, the model consists of three circuit equations for the inductively coupled currents (I_1, I_2, I_p) plus one equation for the RE current which, once the plasma hits the wall, in addition to the avalanche term, as given by equation (6), includes a loss term describing the scraping-off of the beam, $\mathrm{d}I_\mathrm{r}/\mathrm{d}t \approx 2\dot{a}I_\mathrm{r}/a$ [246, 275]. For the vertical plasma motion, the force-free constraint [274], $\xi = (I_1 - I_2)/(I_1 + I_2 + 2I_\mathrm{e})$, is used ($\xi$ is the vertical plasma displacement normalized to a_w, where $2a_\mathrm{w}$ is the distance between the two wall conductors).

During scraping-off, the plasma velocity and electric field can noticeably increase leading to the deposition of a remarkable amount of energy on the REs ($\sim$ hundreds of MJ) [246]. Moreover, during scraping-off, the plasma reaches the $q_a = 2$ limit before the current is terminated. Negligible additional conversion of magnetic into RE kinetic energy is predicted during the RE deconfinement following magnetic fluctuations after $q_a = 2$ is crossed for characteristic deconfinement times lower than 0.1 ms [246], leading to a benign termination of the disruption, whereas larger values of τ_d might result in a stronger energy conversion.

2D fluid models. Axisymmetric 2D plasma evolution models are a powerful and computationally efficient tool for studying vertical plasma motion in tokamaks. Compared to more complex 3D simulations, 2D models offer significantly lower computational costs and allow extensive parametric scans. At the same time, 2D models are able to provide approximate predictions of the strike point locations [10], taking into account the up/down asymmetry and the wall structure. Furthermore, they facilitate the characterization of the linear MHD stability of post-disruption plasma [276], which is important for determining the likelihood of MHD events leading to prompt RE losses to the wall. Additionally, 2D models hold the potential to refine VDE modeling through improved modeling of the halo currents.

To date, five codes capable of 2D plasma motion calculations have been equipped with RE models: DINA [277], TSC [278, 279], JOREK [2, 44, 205], NIMROD [210] and M3D-C1 [280]. Of these, DINA and JOREK have been extensively used to model the impact of REs on PFCs in ITER [2, 10, 248, 281]. Early 2D simulations using DINA confirmed the expected high poloidal peaking factor of the RE strike wetted area, highlighting the importance of 2D models in predicting localized heat loads on PFCs [282].

For upward VDEs in ITER, similar to the 0D model, the 2D calculations show the formation of a RE plateau. The subsequent termination of the RE beam in the 2D simulations occurs mainly by scraping-off of the RE by the wall. Scraping results in RE loss and a simultaneous re-avalanche in the inner region of the plasma close to the edge, resulting in a skin current on the RE current profile [191]. Note that the RE distribution function is expected to be different in the strongly re-avalanching skin layer, where the exponential distribution function is expected [181], and in the inner region, where the electric field is expected to remain close to the avalanche threshold and a non-monotonic distribution function can form [224]. Different distribution functions should lead to different energy dissipation rates, but both DINA [281] and JOREK [2] currently estimate the un-dissipated RE energy using a version of equation (8), which neglects this difference. Both codes predict that up to 100–150 MJ of poloidal magnetic energy is transferred to the REs and deposited on the wall during the scraping-off and the final collapse. This is in general in agreement with 1D models [42]. Note that in the limit of an ideally conducting wall, the force-free constraint [274] implies that the vertical position of the plasma depends solely on the total plasma current. As a result, 'acceleration' of the CQ via high-Z impurity injection has a limited effect on reduction of magnetic energy transfer [281].

Both DINA [281] and JOREK [248] calculations show that downward VDEs in ITER are much faster than upward VDEs due to stronger magnetic field gradients below the X-point. Both models show that wall scraping-off limits avalanche growth, and no significant RE current is formed in low impurity content. For high impurity content, the avalanche is strong enough to form a multi-MA RE current during downward VDEs.

A key advantage of axisymmetric 2D simulations is the ability to perform linear MHD stability analysis during the RE development and the RE beam termination. Such an analysis can help characterize the possible RE losses due to MHD activity and predict the final collapse without performing full 3D simulations [276].

The parameters of the halo currents may significantly impact the dynamics of the VDE in general and the RE beam termination in particular. 2D models have long been employed to analyze halo currents during RE disruptions [244]. Although advances in halo current modeling have been made, such as in [283, 284], the physics fidelity and predictive capabilities of these models have not yet been systematically validated. In particular, while the recent models include a self-consistent treatment of sheath boundary conditions for thermal-plasma regimes, the presence of RE can significantly increase the sheath potential and increase wall erosion and sputtering, thereby modifying the neutral inventory and edge plasma composition—important parameters of the sheath boundary.

Particle-based RE-kinetic models. Particle-based kinetic models operating with 2D axisymmetric EM fields emerge as a powerful tool. These models improve upon those discussed in the previous subsection by tracking individual RE trajectories in 6D phase space, capturing the local effects of EM fields, companion plasma, and impurities. This level of fidelity is indispensable for precisely evaluating wall damage, providing RE energy, pitch angle, and gyrophase, which are essential for characterizing RE impacts on PFCs. In particular, a detailed understanding of the RE beam's interaction with the leading edges of wall facets demands this level of precision. The volumetric energy deposition into PFCs is controlled by the total energy of the REs, as discussed in section 8. Additionally, the deposition is also affected by the angle of incidence into the PFC Θ_{PFC}, which is controlled by the guiding center (GC) angle of incidence θ_{GC} and the pitch angle relative to the magnetic field η according to

$$\sin\Theta_{\mathrm{PFC}} = -\cos\theta_{\mathrm{GC}}\sin\eta\sin\chi + \sin\theta_{\mathrm{GC}}\cos\eta, \tag{9}$$

for instantaneous gyroangle χ. The resulting elliptical, gyro-averaged wetted area will scale as $A_{\mathrm{w}} = \pi r_{\mathrm{L}}^2/\sin\theta_{\mathrm{GC}}$, where the relativistic Larmor radius is $r_{\mathrm{L}} = p\sin\eta/eB$.

EM fields serve as the primary drivers of the RE trajectories, dictating where these particles strike the wall. In axisymmetric configurations, losses typically arise from large drift-orbit effects at high energies or beam scrape-off due to failures in position control. However, the inherent non-uniformity of magnetic fields introduces changes in momentum space. Notably, REs with relatively low energies and perpendicular pitch angles can become trapped within these magnetic structures. Furthermore, the toroidal electric field accelerates REs, influencing their pitch angles. The interplay of plasma and impurity profiles further shapes the RE momentum distribution through collisional and radiative processes, including synchrotron and bremsstrahlung radiation. Collisional friction reduces the total momentum, while pitch-angle scattering broadens the pitch-angle distribution, potentially leading to trapping or detrapping. Partially ionized impurities contribute to small-angle collisional friction, pitch-angle scattering, and avalanche source generation from large-angle collisions.

As a result of RE-PFC interaction (see section 8), ablation of high-Z PFCs, like tungsten (W) or flowing lead–lithium (Pb–Li), introduces a cloud of impurities that significantly influences RE dynamics. The interaction between REs and partially-ionized impurities leads to pitch angle scattering and kinetic energy loss, which are particularly pronounced for high-energy REs. This scattering process directly alters the RE current distribution, subsequently inducing an opposing electric field. The density of these impurities is a critical factor as it determines the extent of the RE distribution change and the rate of avalanche generation by increasing the electron inventory available for large-angle collisions. Additional material modeling is needed to quantify the amount of ablated impurities.

While many particle-based methods exist [114, 250, 285–289], most are primarily applied to non-axisymmetric field systems that will be discussed in section 7. Here, we focus on the work done with the codes KORC [207] and RAMc [201]. KORC offers 6D full-orbit (FO) and 5D guiding-center simulations, leveraging dynamic experimental EM fields, plasma, and impurity profiles. Simulations of DIII-D discharges [223] have revealed RE beam deconfinement before substantial collisional friction energy loss, with pitch-angle scattering dominating during high-Z impurity injection, leading to rapid current evolution and eventual loss of position control. Conversely, simulations of JET pulses [290] demonstrate well-confined RE beams with significant collisional friction losses before position control failure. Subcritical electrons generated by the avalanche operator contribute to significant PFC surface heating, including counter-propagating REs [140]. During final loss events, an increase in the induced toroidal electric field accelerates avalanche growth, but many energetic electrons are generated in deconfined regions. These deconfined REs can be far outside the separatrix, and combined with the challenges of RE beam position control, are an important consideration for PFC beveling design as compared to steady-state scenarios.

RAMc employs 5D guiding-center RE trajectories in dynamic analytic field formulations, which allows for a self-consistent evolution with the kinetic population. It has been shown that toroidal geometry reduces the avalanche growth rate near the beam edge except when the electric field is significantly larger than the critical field [291]. The avalanche source generates trapped REs at the beam edge,

Table 4. Summary of models.

Type	Codes and references
0D/1D fluid	0D [265], 1D [42], 0D+VDE [246]
2D fluid	DINA [277], TSC [278], JOREK [205], NIMROD [210], M3D-C1 [280]
Particle based RE-kinetic	KORC [207], RAMc [201]

which are not sufficiently accelerated by the electric field unless it is significantly larger than critical. High-Z impurities induce an inward Ware pinch [292] and oppose the local avalanche rate decrease near the RE beam edge [293]. The increased fraction of trapped REs from pitch-angle scattering and avalanche generation are Ware pinched. Increased collisionality can also detrap REs in the beam edge, allowing them to be accelerated by the electric field. The increased trapping of REs by the avalanche operator in high-Z impurity RE plateaus, which are insensitive to 3D field transport, can provide a seed to reconstitute the RE beam after an MHD event [294].

The computational demand of particle-based models is substantial. Resolving the gyrofrequency for FO particles or the trajectory of guiding-center particles, both occurring on rapid timescales due to relativistic energies, poses a significant challenge. Moreover, achieving statistically robust results for wall strikes necessitates tracking upwards of 10 million REs [4]. Fortunately, discrete particle calculations are well-suited for GPU hardware, enabling nearly a 100-fold increase in the number of simulated REs compared to traditional CPU-based approaches.

Current and future challenges

Lower-dimensionality models, like those referenced above, are crucial for characterizing the global energy balance during disruptions. These models aim to predict the fraction of magnetic energy channeled into REs and to describe the dissipation mechanisms through which this energy is lost to the wall.

To obtain reliable predictions, there needs to be a stronger coupling between existing EM models for plasma current and position, such as 0D inductively coupled wire models [246, 274] or 2D VDE models [248, 281], and the models for RE kinetics.

Extrapolations to ITER are subject to large uncertainties mainly due to an incomplete understanding of the thermal plasma, the RE beam following the CQ or the instabilities leading to the RE loss. The energy, W_{run}, deposited by the REs on the PFCs has been estimated for the termination of ITER RE plateaus, showing that the magnetic energy converted into RE kinetic energy can be as much as a few hundreds MJ for large RE plateau currents and slow (large τ_{d}) terminations [42, 246, 265, 281].

Note that these results are consistent with observations of benign RE terminations via low-Z injection [58, 59, 96, 137]. Extremely strong MHD activity in such plasmas leads to a very fast deconfinement of the RE population, resulting in negligible conversion of magnetic to RE kinetic energy and a very large wetted area without significant heat loads on the PFCs. A sufficiently clean plasma is required to avoid RE regeneration and energy conversion [58]. More simulations are needed to evaluate RE regeneration in these events in ITER, where larger avalanche rates may change the situation.

Currently, reduced EM models rely on simplistic RE kinetic models, which are inadequate for a reliable characterization of RE energy loss channels. On the other hand, existing detailed kinetic simulations are typically expensive, limiting their application. There is a need to develop plasma evolution models that account for essential features of RE kinetics, such as the significance of subcritical energetic electrons generated by RE avalanche for surface heating [140], or the survival of the trapped RE population for RE current reconstitution after a MHD flush during benign termination of the disruption [294].

Radial RE transport and the background plasma composition play key roles in determining the dominant RE energy loss channels. Thus, refining transport and ambient plasma models are essential for reliable prediction of global energetics of the disruption and the RE beam termination. From this point of view, the development and integration of reduced self-consistent models for MHD-induced transport regarding the loss time scale and deposition width is of interest. Further validation of these reduced models with the experiment would be desirable. Improvements are needed regarding plasma–wall interactions, including the reliable prediction of halo current formation during VDEs and plasma quasi-neutrality issues during large RE losses to the wall, as well as developing a better understanding of what determines the RE wetted area for scrape-off impacts.

Concluding remarks

Reduced models for the energy balance during disruption current terminations have shown to be adequate for the identification of the main mechanisms leading to the conversion of magnetic into RE kinetic energy as well as to get simple estimates of the energy that can be deposited on the PFCs due to the REs. Table 4 presents a summary of the main models herewith discussed. Despite the uncertainties regarding the thermal residual plasma and the RE beam features following the CQ of the disruption, or the processes leading to the loss of the RE plasma, it is expected that in ITER as much as a few hundreds of MJ might be transferred to the REs [42, 246, 265, 281], particularly for slow current terminations. Nevertheless, for a confident assessment of the impact of the RE loads on the PFCs, it turns out to be essential that future reduced-dimensionality disruption models include a number of key physics elements at an appropriate fidelity level: elements of RE kinetics [140, 294], including RE avalanching in strong fields induced during plasma scraping, adequate descriptions of background plasma and radial transport, or effects of plasma–wall interaction such as the halo currents.

8. High fidelity RE beam dynamics and impact models

E Nardon[1], M Hoelzl[2], C Liu[3] and D del-Castillo-Negrete[4]

[1]IRFM, CEA Cadarache, F-13108 Saint-Paul-lez-Durance, France
[2]Max Planck Institute for Plasma Physics, Boltzmannstr. 2, 85748 Garching b. M, Germany
[3]State Key Laboratory of Nuclear Physics and Technology, School of Physics, Peking University, Beijing 100871, People's Republic of China
[4] Institute for Fusion Studies, University of Texas, Austin, Texas, United States of America

Status

There is clear experimental evidence that the 3D nature of the magnetic field plays an important role in a substantial fraction of RE impacts. It might be a key ingredient to access benign terminations on one hand, but also the origin of highly localized depositions. One piece of evidence is the fact that RE impact patterns are typically non-axisymmetric to a degree not explicable by wall asymmetries as has been illustrated in sections 1–3. Another one is that, e.g. in JET [82], the RE beam evolution when approaching termination is typically characterized by sudden drops in the RE current I_{RE} accompanied by discrete bursts of magnetic fluctuations, HXRs and neutrons, with the final impact associated with a relatively low value (often approaching 2) of the safety factor at the edge of the beam q_a, suggesting a key role of MHD instabilities. Note that in these JET cases, as well as in comparable scenarios in DIII-D and AUG, q_a decreases over time down to low values. In other experiments, e.g. on AUG [295], q_a is thought to remain relatively high, and in these cases a steady decay of I_{RE} down to 0 is observed. Another aspect that points to an important role of the 3D nature of the magnetic field is the wetted area by the RE impact that exceeds the one explicable by a 2D scrape-off, in particular in benign termination scenarios.

Accurate simulation of REs in stochastic magnetic fields is also critical for the assessment of RMPs in the control and confinement of REs [296]. In general, understanding the relationship between the stochasticity of the magnetic field and the stochasticity of the RE orbits can be a very nontrivial problem requiring FO computations. For example, as documented in [297], depending on the regime, GC simulations might significantly overestimate RE losses with respect to FO computations. In addition, when the RE Larmor radius is comparable to the island size, GC and FO can exhibit significant differences. A key question related to this is the role of magnetic stochasticity, which could explain such a broadening of the deposition. It is, on the other hand, important to note that a 3D magnetic field structure does not necessarily imply strong stochasticity or broad deposition: it may be that the RE beam gets distorted (i.e. kinks) while the flux surfaces remain topologically nearly intact. Such a distortion, combined with a motion into the wall due, e.g. to a vertical instability, is a hypothesis to explain why the impacts of the RE beam may be so localized in certain cases. On the other hand, significant—and sometimes very strong—magnetic stochasticity may appear, as suggested by numerical simulations discussed below, and could have a key influence on the RE beam impact. One may imagine a deleterious influence of stochasticity in a scenario where a large stochastic region is initially bounded by an annulus of good flux surfaces that gets destroyed over a short period of time, leading to an abrupt loss of all REs, potentially in a localized manner. Such a scenario could lead to rapid loss of confined REs in a narrow flux tube [298], but has not been observed in 3D non-linear simulations so far, which instead suggest that stochasticity grows from the outside in, leading to a relatively broad deposition pattern. Such simulations have, however, focused on benign termination scenarios, and the inside-out formation of stochasticity is not necessarily excluded for other scenarios. A key concept to understand the impact of stochasticity is the magnetic footprint, that is, the region of the wall that is connected to the core of the beam by field lines [299]. This region is bounded by so-called 'manifolds'. Depending on how fast and how large the magnetic footprint grows, the wall surface where REs hit may vary significantly. A possibly important complication is that the orbits of highly energetic electrons may be less stochastic than the field lines themselves due to drift orbit shifts as well as a spatial averaging of the field over the gyro-orbits. Such a decoupling of transport from magnetic topology was described for instance in [206, 257, 258, 300, 301].

RE dynamics in fusion plasmas exhibits a wide range of temporal scales, going from the fast gyro-period, $\sim 10^{-11}$ s, to the observational time scales, $\sim 10^{-3} \ldots 10^{-2}$ s. Overcoming the computational challenges of this scale separation has motivated the development of approximate, perturbative orbit models like the extensively used GC description. Although these approximations have been useful for thermal plasmas, the simulation of the relativistic dynamics of high-energy REs in 3D magnetic fields requires

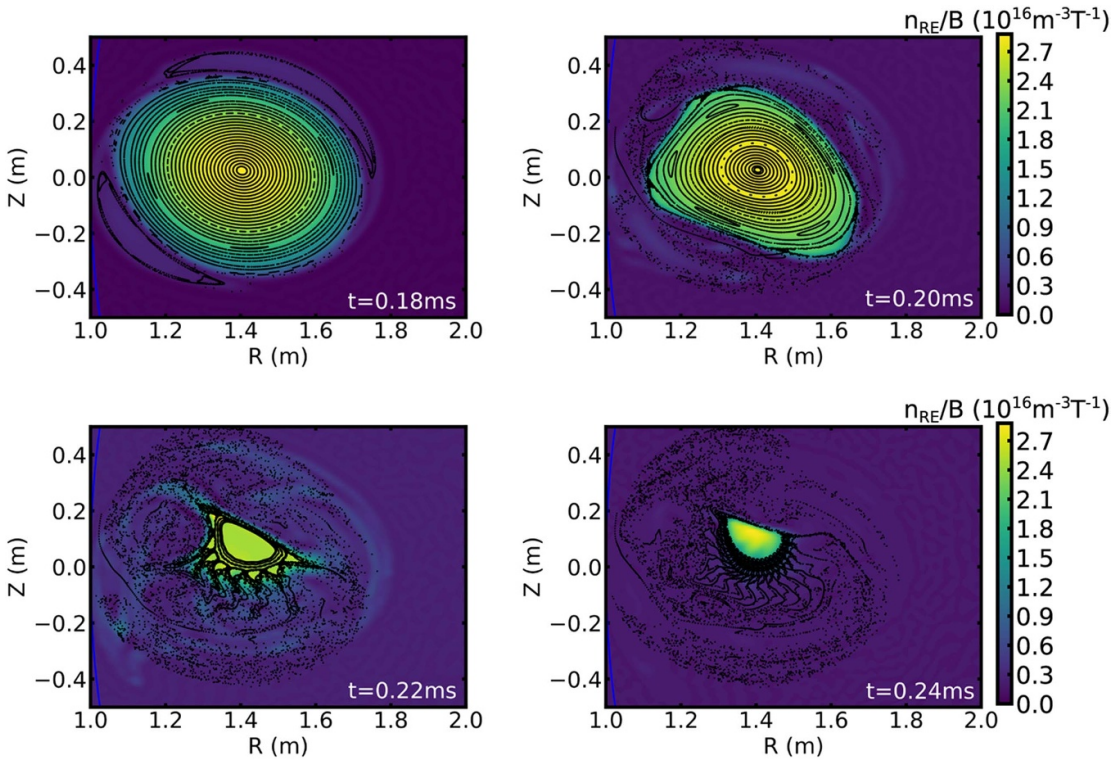

Figure 21. M3D-C1 simulation of a termination in the DIII-D tokamak. The time evolution of the RE density distribution is shown in color along with a Poincaré plot visualizing the dynamically changing magnetic field topology. Reproduced from [209].

the incorporation of FO effects, synchrotron radiation damping effects along with collisions and avalanche sources. Motivated by this need, numerical codes like the KORC have been developed to perform high fidelity simulations of REs using high-performance-computing platforms [207, 223]. Among other uses, FO information is critical for the development of accurate synchrotron emission synthetic diagnostics [302, 303].

The type of instability that develops during the evolution of the RE beam up to its impact on PFCs may vary from case to case. Since they are often related to $q_a \simeq 2$ [59], it appears likely that benign terminations in many DIII-D, JET, TCV and AUG experiments involve an $m = 2$, $n = 1$ resistive external kink mode (m and n being the poloidal and toroidal mode numbers, respectively). Also collapses at larger q_a are observed, which may also be external kink modes but at q values on axis substantially larger than unity. A decrease of q_a with time is necessary to access these scenarios, which could be robust to achieve: RE current is lost in the scrape-off of outer flux surfaces during vertical motion and partly re-induced as Ohmic current. Consequently, I_p reduces less than the cross-section, reducing q_a [304]. Ohmic current is converted back to RE current by avalanching. The physics of such instabilities, in particular for the case where the current is initially carried by REs, has been studied with M3D-C1 [305, 306], including a self-consistently coupled RE fluid model [209]. Figure 21 shows the evolution of the magnetic topology along with the RE density during the burst of MHD activity. Similar observations were made with the JOREK code [205, 307] for ITER [2]. In some JET benign terminations, on the other hand, where synchrotron emission suggests a hollow current profile, the relevant mode appears to be an $m = 4$, $n = 1$ double tearing mode (TM) [308] (the beam's synchrotron emission shows magnetic-island-like patterns before termination [309]). In [303] it was observed that synchrotron emission in 3D stochastic magnetic fields, computed using NIMROD, is strongly influenced by magnetic islands. Also, in the presence of magnetic islands, trapped particles exhibit higher radiation damping than passing particles. In [310] experimental measurements and KORC simulations of synchrotron emission in the presence of a (2/1) mode and magnetic stochasticity were used for current profile reconstructions in post-disruption RE plateau plasmas in DIII-D.

The physics of TMs in the presence of REs has been studied theoretically [311] and numerically with the M3D-C1 [280], NIMROD [210], SCOPE3D [312] and JOREK [206] codes. A key finding is that the growth rate of these modes is essentially determined by the resistivity η and density n_e of the

background plasma. Furthermore, the growth rates follow the $\eta^{3/5}$ scaling up to much higher resistivity values than in a thermal plasma, effectively increasing the growth rates for very cold background plasmas [43, 206, 311, 313]. The same destabilizing effect at high η of the companion plasma is also observed for other MHD modes like resistive internal kinks [44, 211] and is probably quite universal. The reason for the saturation of growth rates at very high values of η is a consequence of the radial extent of the eigenmodes becoming comparable to the plasma minor radius. The presence of REs tends to reduce the radial extent of the mode structures such that this saturation is shifted to higher resistivity values. In addition, the saturated island width is enhanced by the presence of REs for otherwise identical plasma conditions. Additionally, simulations have shown that in highly resistive plasma (like a CQ after substantial high-Z impurity injection), resistive hose instabilities may exhibit higher growth rates than TMs, leading to rapid RE transport and losses [210].

It appears likely that benign RE beam terminations are (at least partly) caused by the very fast growth of large magnetic footprints, the latter being due to a combination of the very high η and low n_e of the background plasma. The very high η and low n_e result from the massive injection of deuterium used to obtain the benign termination, which causes the plasma to cool down and recombine. The fast growth of large magnetic footprints at high η and low n_e is supported by JOREK [2] and M3D-C1 simulations [209]. In these simulations, the magnetic field is strongly stochastic with very short connection lengths to the walls almost throughout the beam volume, leading to a nearly full dumping of the REs onto the wall on the time scale of micro-seconds. Simulations have also been performed with the linear MHD code MARS-F, in which the amplitude of the MHD mode was prescribed based on experimental magnetic measurements for DIII-D cases [289]. During the RE dumping event, the current is transferred to Ohmic current carried by the background plasma with apparently weak RE re-avalanching, as discussed in section 6, but 3D simulations including a fully self-consistent evolution of the background plasma (reheating, re-ionization, etc) have not been performed yet. The fact that modes grow faster at high η and low n_e is in line with the above-mentioned finding from previous works that the modes growth rate is determined by the properties of the background plasma (n_e influences the dynamics via the Alfvén speed). The reason for the growth up to a larger amplitude is less clear. To some extent it may be a direct consequence of the presence of the REs, as shown for saturated TMs analytically [311]. It might also be related to the larger saturation amplitude of TMs at larger η found and explained in [314], although it should be noted that REs are not included in that work. When REs carry the initial current prior to a termination, another mechanism that can come into play is that the radial RE transport associated to the increasing stochasticity may flatten the current density profile and thus reduce the drive for further mode growth. There seems to be evidence for this self-regulation from JOREK simulations conducted using different RE parallel transport models: when the RE parallel transport is mimicked by a relatively slow diffusive transport to save computational costs [308], modes reach a larger amplitude in comparison to other simulations where the RE parallel transport is realistically accounted for by advection at the speed of light [206, 315].

One difference between benign and non-benign RE beam terminations is that the former are typically associated to a single burst of magnetic fluctuations, HXRs and neutrons, while the latter are associated to multiple (smaller) bursts. The origin of this behavior is not fully established, although stronger MHD activity in benign scenarios, causing a faster near-complete loss of the REs is likely to play a central role in many cases. The energy and pitch angle distribution of REs impacting the wall during DIII-D RE termination has been diagnosed and compared with KORC simulations [40], revealing that MHD instabilities can lead not only to a broader wetted area, but also to increased RE pitch angles.

Predictions on RE beam impacts have been made for ITER with JOREK [2, 3] and MARS-F [316] and for EU-DEMO with JOREK [317]. In the case of JOREK, the 3D simulations can be post-processed with kinetic test particles to obtain a load distribution to the realistic 3D wall structures. Figure 22 shows both the loss of REs during a termination event in ITER and the resulting loads to 3D walls from such a calculation. The methodically comparable work on EU-DEMO [317] also assesses the efficiency of sacrificial limiters in protecting the wall from excessive RE loads. The strong 3D field perturbations pose a challenge for first wall protection and will be re-assessed based on ongoing substantial design changes of EU-DEMO. Benign termination in DIII-D and JET was studied in [59] using MARS and KORC to elucidate the necessary levels of $\delta B/B$ to deconfine the full RE population and to estimate the wetted area over which the RE energy distributes during the loss events. In addition to MHD instabilities, plasma waves associated with REs have been observed both during the flattop [239, 241] and disruption phases [318, 319]. Simulation studies have confirmed that these excited waves can induce additional pitch-angle scattering [43] and spatial diffusion [320] of resonant REs, presenting a potential approach for RE mitigation through self-excited or externally launched RF waves. The full-wave code AORSA, in conjunction with KORC, has been used to investigate the phase-space diffusion of REs in the presence of

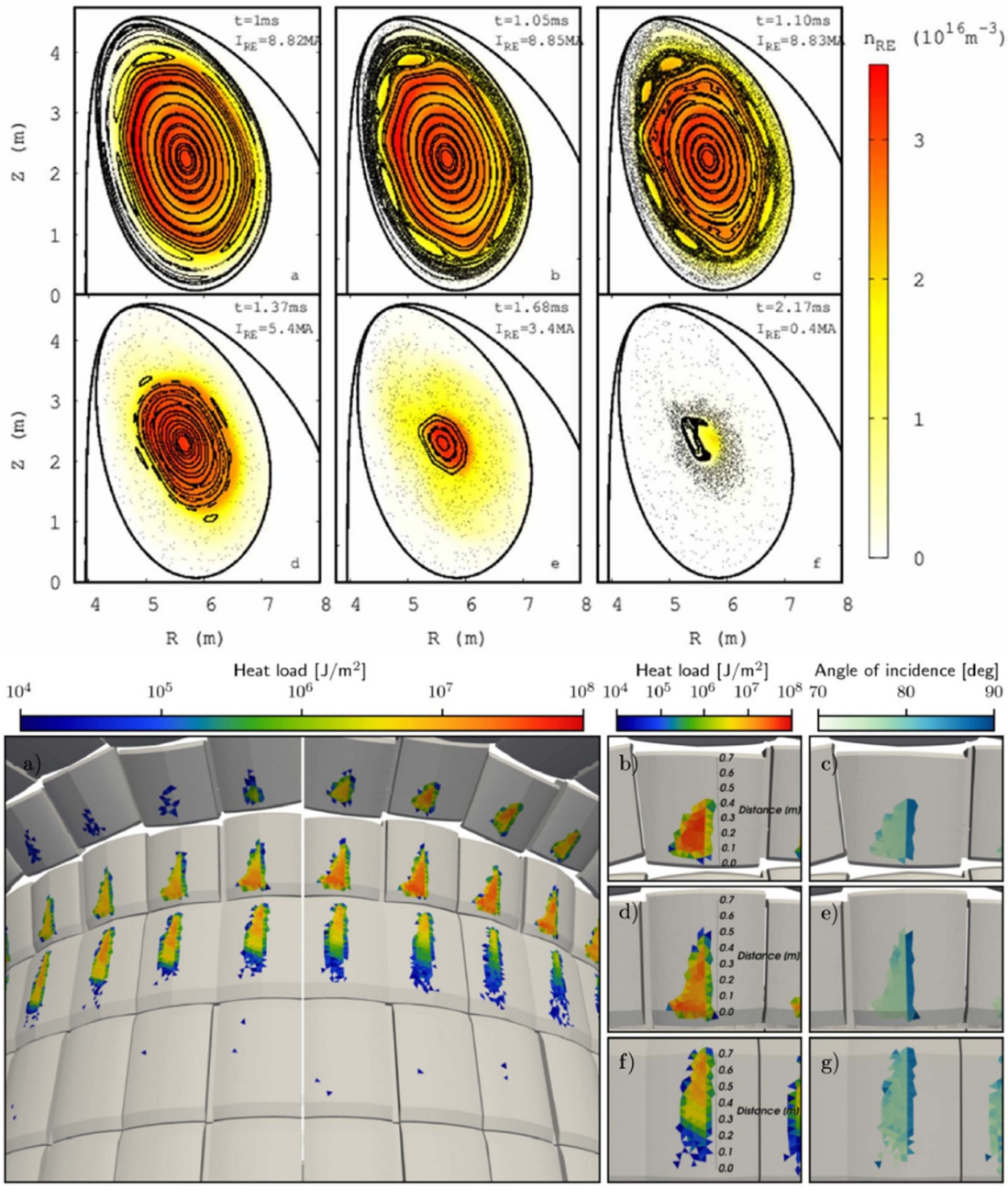

Figure 22. Top: JOREK simulation of a RE beam termination in ITER when the safety factor at the plasma edge has reached a value of $q_a = 2.2$. Reproduced from [2]. CC BY 4.0. Bottom: RE induced wall loads in such a RE termination event in ITER. (a) Overview of tiles hit by REs at the top on the high field side. (b/d/f) Heat load for the tile with the strongest RE load in the top/middle/bottom row of (a). (c/e/g) Average angle of RE incidence corresponding to the tiles of panes (b/d/f). Reproduced from [3]. CC BY 4.0.

these waves. However, whether this diffusion effect can effectively reduce the RE energy impact on PFCs remains an open question.

Particle-based plasma kinetic simulations of REs are time-consuming due to the multiscale dynamical processes involved and the need to follow large ensembles of particles to avoid statistical sampling errors. To overcome some of these computational challenges, [321] proposed a generative artificial intelligence based normalizing-flow method for the efficient computation of hot-tail generation of REs. The proposed method learns the probability distribution function of the final state conditioned to the initial state, such that the model only needs to be trained once and then used to handle arbitrary initial conditions.

Current and future challenges

Currently, the community is developing predictive modeling capabilities to support the design of future machines and/or mitigation strategies in such a way that RE beam impacts remain tolerable. The most effective way is probably to rely on 3D non-linear MHD codes including self-consistent RE models, in combination with realistic RE-wall interaction modeling (section 8). In this area, a number of challenges need to be solved as discussed in the following paragraphs.

Termination simulations need to start from a (relatively) stable state instead of a highly unstable one, as has been done so far. To capture the explosive nature of termination, stabilizing effects may be needed beyond those already included in the models currently existing (similar to how the explosive onset of type-I ELM cycles could only be captured by incorporating stabilizing terms [322]).

The background plasma, which may be weakly ionized at the start of the termination event, needs to be self-consistently described, including its re-ionization and/or re-heating as the REs are lost. Kinetic models may be needed to capture the ballistic nature of neutral particle transport.

Realistic kinetic RE distributions at the start of impact need to be used for termination studies as well as for wall impact calculations, as they can affect the plasma dynamics (see the following two items) and drastically change the wall damage (as explained in section 8). The companion plasma composition and the dynamics of MHD instabilities may affect the RE distribution function and thus directly affect the benign-ness of a termination event.

Since trapped REs could survive a stochastic phase and later act as seed for re-avalanching [294], kinetic treatment is also needed in view of trapping and de-trapping like assessed in the context of 3D MHD dynamics in [323].

The contribution of the REs to the major-radial force balance must be taken into account, as it can affect both the MHD stability and the wall contact point. The Shafranov-like shift of flux surfaces is neglected in the present RE fluid modeling but can be captured in kinetic modeling [206] or, under the assumption of mono-energetic RE beams, also in advanced fluid models [324, 325].

The drift orbit shift of REs needs to be taken into account. Since this deviation of REs from flux surfaces depends on their energy and pitch angle, it may de-correlate the narrow current structures associated with the MHD modes and thus have a direct effect on the stability of the MHD modes as well as the RE deposition and losses.

The effect of the vapor and/or solid debris produced by the impact may need to be taken into account directly in the 3D simulations as it can have direct consequences on re-avalanching and RE distribution functions. This could require future self-consistent coupling of 3D MHD simulations to the wall damage models described in section 8.

The interaction of REs with kinetic instabilities, which are not captured in the MHD framework, should be assessed as well, as they could play an additional role in transport and termination processes or open up alternative ways of mitigation.

Note that we focus on the interaction of REs with material structures here such that RE *mitigation* or *suppression* approaches like passive helical coils or active mitigation measures are not addressed, albeit they are often studied by the same codes and models.

Concluding remarks

There are indications that, both, extremely localized RE depositions causing large damage as well as very broad depositions in case of benign termination scenarios are a result of 3D plasma dynamics. At the same time, REs can have direct consequences on the stability and non-linear saturation of plasma instabilities such that MHD and REs need to be studied self-consistently. Major non-linear MHD codes are establishing hierarchies of models for these dynamics and interpretative as well as predictive simulations are substantially contributing to the advance of the field. Further effects not taken into account yet will require additional developments towards higher fidelity models likely describing REs, neutrals and impurities kinetically. The phase space distribution of REs may directly affect MHD dynamics and determines the volumetric energy deposition of REs in the wall structures, it is thus essential when aiming to assess the RE induced risk for material integrity. The 3D modeling profits from the strong advances regarding the complementary lower-dimensional models (sections 5 and 6) and can provide accurate phase-space resolved deposition patterns for wall damage analysis (section 8).

9. Modeling of thermo-mechanical PFC response under RE impacts

S Ratynskaia[1], P Tolias[1] and V Dimitriou[2]

[1] Space & Plasma Physics, KTH Royal Institute of Technology, Stockholm, SE-100 44, Sweden
[2] Institute of Plasma Physics and Lasers—IPPL, University Research and Innovation Centre, Hellenic Mediterranean University, Rethymno, GR-74150, Greece

Status

As reviewed in sections 1–3, RE-PFC interaction is often an explosive event accompanied by the expulsion of melt or fast solid debris. PFC explosions are triggered by the non-monotonic temperature response, with the beneath-surface maximum implying the build-up of internal stresses which leads to failure, fragmentation and fast material detachment. With the RE wetting characteristics provided, see sections 5–7, modeling of RE-induced PFC damage further requires: (i) MC calculations of electron transport in the PFC to evaluate the energy deposition profile, (ii) continuum mechanics calculations of the thermo-mechanical PFC response to this volumetric heat source.

Energy deposition. The transport of relativistic electrons inside condensed matter is accompanied by momentum losses owing to elastic scattering on the nuclei as well as by energy losses due to the ionization or the excitation of core or valence electrons (electronic stopping) and due to the emission of Bremsstrahlung photons in the field of the nuclei or core electrons (radiative stopping) [326]. Therefore, a particle shower is induced that comprises fast atomic electrons (delta-rays), photons, positrons (via gamma conversion) and neutrons (via photo-nuclear reactions) [327]. The relevant EM and nuclear cross-sections strongly depend on the energy and the atomic number [328, 329]. In W: radiative stopping overcomes electronic stopping for electron energies larger than 10 MeV [330], gamma conversion overcomes Compton scattering, Rayleigh scattering and photo-absorption for photon energies larger than 6 MeV [331], while photonuclear reactions have a 7 MeV photon threshold and 15 MeV maximum [332]. In graphite: Bremsstrahlung losses dominate for electron energies above 100 MeV [330], gamma conversion is the primary photon interaction for photon energies exceeding 30 MeV [331], while photonuclear reactions have a 19 MeV threshold and 22.5 MeV maximum [332].

Within the continuous-slowing down approximation (CSDA), electrons lose energy continuously along their path with a mean energy loss per unit path length given by the stopping power [333]. The CSDA range is the reciprocal of the stopping power and is defined as the average path length traveled by the incident electron until its complete thermalization [333]. It allows to appreciate the volumetric nature of the energy deposition. For typical RE energies from 1 to 50 MeV, the corresponding CSDA ranges vary within 0.04–0.78 cm for W and within 0.28–12.85 cm for C [16]. However, these values do not reflect the characteristic energy deposition depths in any scenario and especially in fusion scenarios due to the facts that: (i) the energy carried by delta electrons and Bremsstrahlung photons is non-locally deposited, (ii) the path length and depth generally differ due to scattering, (iii) the incident angles are generally shallow in tokamaks exacerbating the difference between path-length and depth (see figure 23), (iv) the tabulated CSDA ranges do not consider the effect of the magnetic field on charged particle trajectories.

Approximations of RE deposition as a surface load [2, 3] allow use of heat flux factor thresholds to evaluate whether REs can cause PFC melting [334]. Such critical heat flux factors stem from the analytical solution for heat diffusion in a semi-infinite solid [335]. However, the validity of the surface loading assumption is very limited, e.g. to <1 MeV incident energies for W. Approximations of RE deposition as an exponentially decaying volumetric source with an e-folding length equal to the CSDA range [76, 140, 265] also exploit the availability of exact solutions of the 1D heat diffusion equation. Such analytical temperature profiles have been derived for an exponentially decaying source [335], even including vaporization [336] or convection [337] and have found practical use in laser-solid interactions and medical physics [338]. This exponentially decaying assumption also has strong limitations. Even under the gross simplification that energy is strictly deposited along the straight path of primary electrons (implying that the secondary particle depth ranges are all zero), the Bethe formula does not admit an exponentially decaying solution due to the $\propto \ln E/E$ basic scaling of the electronic stopping power (despite the $\propto E$ basic scaling of the radiative stopping power). In fact, it is known from calorimetry measurements [339] that the energy deposition profiles of MeV electrons in low- and high-Z materials have a well-pronounced maximum, see figure 23. The maximum could reside near the surface, as for low energies and grazing angles, but still the CSDA based exponential decay remains a poor fit, see figure 24.

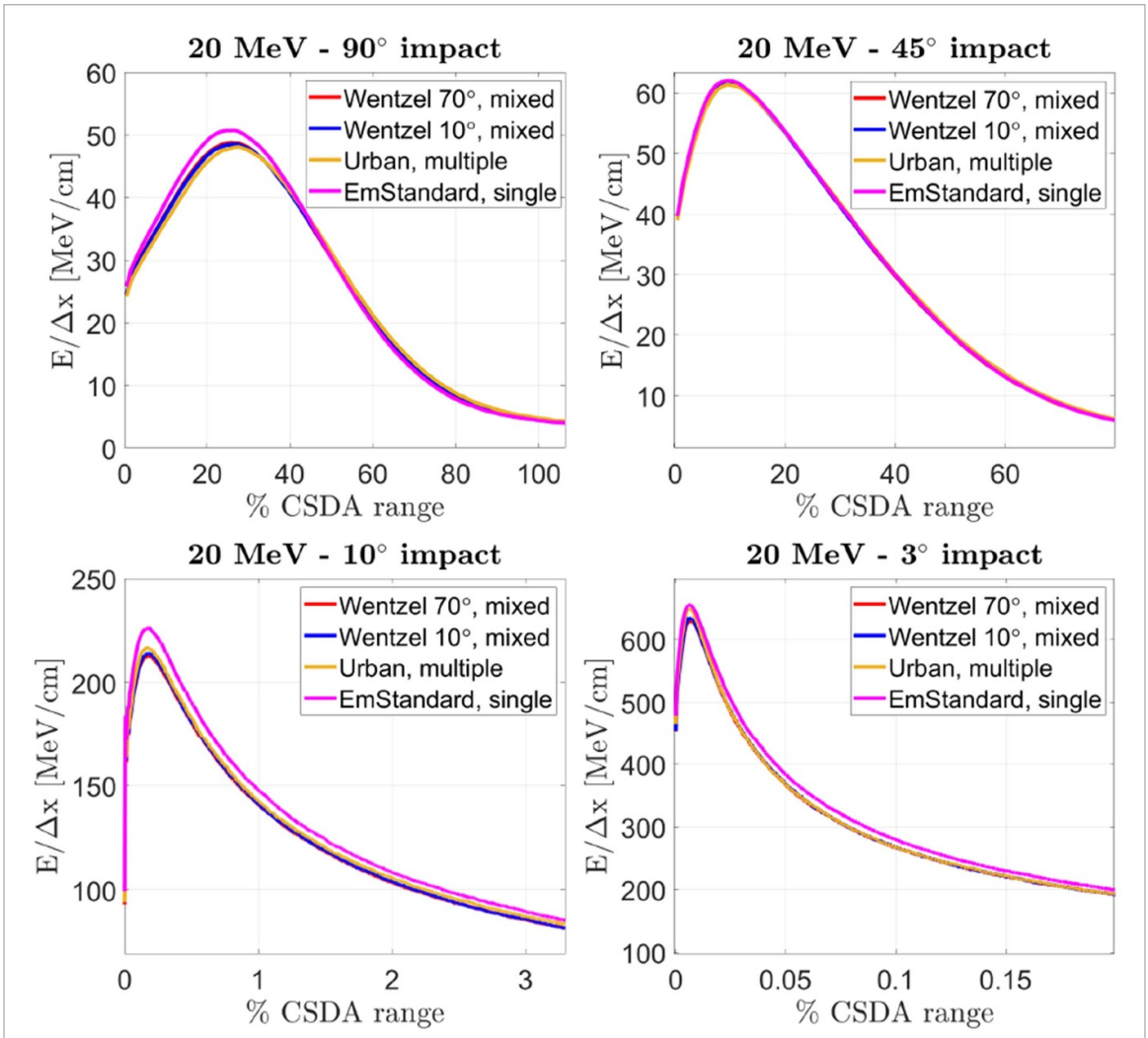

Figure 23. Geant4 results (with various scattering implementations) for the in-depth (plane averaged) energy density profiles of 20 MeV electrons impacting W at normal to shallow angles.

The first MC simulations of RE energy deposition that considered coupling between electron and photon transport can be traced back to the beginning of the 1990s and were performed with early versions of the ITS [340–342], GEANT [343–346] and EGS [347–349] codes. They were followed by MC investigations that are dated back to the 2000s and 2010s with the FLUKA [350, 351] and EGSnrc [352, 353] software packages as well as with the inaccessible ENDEP code [354, 355] or with in-house modules [356]. Nowadays, most MC studies are carried out with recent versions of Geant4 [357–359] or FLUKA [360, 361]; versatile toolkits that offer an extensive selection of differential cross-sections and scattering algorithms. The user's choice determines the accuracy and compute time that depend on the PFC material and RE wetting.

The magnetic field effect on RE energy deposition was pointed out already in the 1990s [341, 344, 348]. The *B*-field presence outside the PFC implies that backscattered electrons can be redeposited during their gyration, thus more energy is absorbed [344, 348]. This is the main effect unless the backscattering yield is negligible, which is the case for normal incidence and energies deep into the MeV range [362, 363]. The *B*-field presence inside the PFC implies that all charged particles are gyrating [344, 348]. This is a secondary effect due to the collision-dominated transport. The *B*-field has been discussed in connection with the impact angles and phase randomization upon wetting [356]. Backscattered electron re-deposition can lead to non-uniform loading even for uniform RE impacts [364].

Thermo-mechanical response. Most investigations have focused on the thermal PFC response by solving the heat diffusion equation, which allows estimates of the instantaneous melt depth, erosion depth due to vaporization and coolant temperature [10]. The latter constitutes a critical safety issue for fusion reactors, since elevated temperatures at the bond interface with the cooling substrate can lead to water leaks. As aforementioned, grazing angles are responsible for shifting the energy deposition maximum

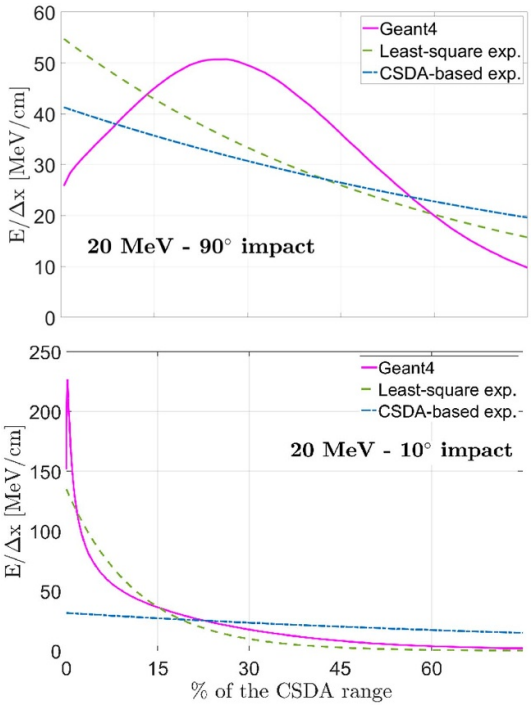

Figure 24. Comparison of Geant4 deposition profiles, for 20 MeV electrons impacting W at normal (90°) and shallow (10°) angles, with a least-square and a CSDA-based exponential decay.

towards the plasma-facing surface. This results to very high energy density values in the vicinity of the free surface and, thus, to very high surface temperatures. Strong vaporization implies that the free surface deformation needs to be accounted for in the heat transfer simulations [336, 352, 364]. At this point, we stress that there are two reasons behind the build-up of the non-monotonic temperature profiles; (i) the non-monotonic energy deposition profiles, which are naturally reflected in the temperature profiles courtesy of the relatively short loading times that limit the smoothing effect of diffusion [119], (ii) the intense surface cooling due to vaporization, which can efficiently reduce the surface temperature [336].

The first investigations beyond the thermal PFC response were recently reported focusing on predictions for the onset of failure in brittle PFCs that do not possess a liquid phase (graphite and boron nitride) [4, 365]. The governing partial differential equations were those of linear one-way coupled thermo-elasticity [366]. In particular, within infinitesimal strain theory, the heat diffusion equation with a volumetric source was coupled to the Navier displacement equation via the thermal expansion term. The mechanical work carried out during thermal expansion was not included in the heat transfer equation [366, 367], being dominated by the RE volumetric heating. The equations were solved with the finite element method (FEM) and the brittle failure predictions were based on the Rankine criterion, which compares principal stresses with ultimate tensile and compressive strengths [368]. A novel KORC—Geant4—FEM workflow was validated against the first controlled RE-induced damage experiment carried out with a graphite sample in DIII-D [40] (see section 3), which provided constraints on the loading time and total energy deposited. This PFC response model was also capable of describing aspects of RE-induced boron-nitride tile damage in WEST, but with less constraints due to the accidental nature of the event [365].

Current and future challenges

Thermophysical and mechanical W properties. Multiphysics modeling of the thermo-mechanical response of W PFCs must consider the hydrodynamic behavior, which requires a multiphase equation of state valid in a wide range of pressures and temperatures as well as the deviatoric behavior which requires a damage criterion and a viscoplastic flow rule that captures the effects of high strain rates, elevated temperatures and strain hardening [369–373]. Tabular equations of state are available for W [374]. Empirical and semi-empirical constitutive models also exist, such as the Johnson–Cook [375] and Zerilli–Armstrong model [376], which feature various material constants whose values are available for

W [377]. The accurate determination of these constants from an ever increasing body of experimental data and the quantification of uncertainty propagation pose a great challenge.

Fracture and fragmentation. It is beneficial to identify the volume patches of the continuum geometry and the exploded fragments. The former can be modeled with traditional FEM, while the latter require sophisticated techniques that overcome mesh limitations.

Finite strain theory is essential for large displacements and strains ($\gtrsim 2\%$) [378]. The Cauchy strain tensor is substituted with the Green–Lagrange strain tensor which contains a second-order term that describes large deformations and rotations but leads to nonlinear partial differential equations. Traditional FEM is a mesh-based approach developed on variational principles and/or weighted residual methods, capable of handling infinitesimal and finite strains [367]. Finite strain FEM, applied for high energy density problems involving explosions, requires iterative solvers like Newton–Raphson due to nonlinearity [367, 378]. Such simulations are limited only by the severe mesh distortions that introduce numerical instabilities. Therefore, mesh adaptivity and updating or remeshing of the discretized domain is essential to capture large deformations and strong gradients. Explicit FEM solvers can accommodate various damage criteria, since flags can be set to trigger failure of an integration point, erosion and element deletion [379–384].

Smoothed particle hydrodynamics (SPHs) is a mesh-free numerical method suitable for highly dynamic problems involving extreme deformations, fragmentation as well as fluid-structure interaction [385]. SPH is based on kernel interpolation and a Lagrangian formulation, but instead of introducing a mesh, it represents the material as a collection of particles that move and interact. The kernel ensures greater contributions from nearest neighbor particles to the reference particle, achieved with a smoothing length. In particular, fluid-structure interaction allows for a better representation of the motion of high-speed debris. However, SPH is sensitive to tensile instability due to kernel approximation errors and requires special treatments like adaptive kernel corrections and artificial viscosity.

The arbitrary Lagrangian Eulerian (ALE) method is a hybrid of the Lagrangian and Eulerian approaches that combines their best features [386, 387]. The mesh partially moves with the material but can also be adjusted to reduce distortion while still tracking material motion. ALE is excellent for fluid-structure interaction, blast & explosion modeling, and high-speed impact problems [387, 388]. However, ALE is computationally expensive due to the Lagrangian mesh motion and remapping and often introduces numerical diffusion during the remapping steps in the Eulerian mesh.

The phase field method (PFM) models fracture by diffusing a crack over a small length scale instead of treating it as a discontinuity [389]. This is achieved with the phase field ϕ that continuously varies from 0 (pristine) to 1 (failed). Intermediate values correspond to a diffuse transition zone, thus eliminating the need to track an explicit crack surface [389]. The $(\boldsymbol{u}, \phi)$ fields are found by minimizing a free energy functional that includes the elastic strain energy and fracture energy. PFM has found limited use in large deformations, since coupling with finite strain theory and damage criteria demands modifications that make it computationally costly. PFM requires fine meshes to resolve the diffuse zones, implicit solvers for the coupled $(\boldsymbol{u}, \phi)$ system, time-stepping schemes for the crack evolution and preconditioning techniques to improve convergence.

Peridynamics theory (PD) is a nonlocal formulation that replaces spatial derivatives with integrals to handle fracture and extreme deformations [390, 391]. The material body is represented as a collection of discrete points, each interacting with other points within a horizon δ through bonds that can stretch or compress under deformation and break when a failure criterion is met [391]. The horizon defines the nonlocal interaction range with larger δ increasing accuracy and the compute time. PD is mesh free and element connectivity is not required, avoiding mesh distortions. However, PD is difficult to implement and to efficiently parallelize.

Coupling between the RE deposition and PFC response. MC simulations calculate the RE energy deposition into a pristine amorphous material at room temperature. As far as the pure thermal PFC response is concerned: (i) the direct effect of elevated temperatures in the stopping power is negligible, since the PFC temperature should be an order of magnitude lower than the electronic Fermi temperature ($\sim$10 eV), (ii) the indirect effect of elevated temperatures in the stopping power through the mass density can locally reach 20% (see the proportionality), which is also rather insignificant, (iii) in the case of strong vaporization, the vapor cloud could have a strong effect on energy deposition, provided that there is significant density depletion due to expansion into vacuum during RE wetting. As far as the thermo-mechanical PFC response is concerned, depending on the deformation scales and the wetting duration: the evolving free surface due to melt motion or fragmentation could affect energy deposition.

Such problems require dynamic coupling between MC and FEM simulations, which is computationally costly.

Coupling between the RE transport and PFC response. Transport of REs into PFCs is accompanied by the ejection of electrons, positrons, photons with a broad energy distribution. In case of strong vaporization, low energy impurity atoms are also emitted. In case of PFC explosions, debris with sizes less than the CSDA range are ejected in the vacuum vessel. It is conceivable that interactions with these products could affect the RE seeding, avalanche or termination phases. An iterative RE impact—RE deposition—PFC response workflow is unrealistic and toy models would need to be developed.

RE-induced stress. In general, RE transport yields a volumetric heat source Q in the heat transfer equation and an external stress term $\nabla \cdot \vec{\sigma}$ in the displacement equation. MC simulations can calculate the cumulative internal stress field generated by the incident electrons and secondary particles. However, the post-processing is complicated and probably also prone to statistical & grid errors. A simplified comparison between the strain contribution from particle momentum transfer and the strain contribution from thermal expansion should precede the development of post-processing routines.

Indirect RE-driven damage. As mentioned in section 3, high-velocity impacts of solid dust on the surrounding wall are a source of de-localized RE-induced damage. The high velocity regime of 0.2–4 $\mathrm{km\,s^{-1}}$ is distinguished by strong plastic deformation, projectile fragmentation, shallow target cratering and near-surface melting of both bodies [392–395], while the hypervelocity regime of $>4\,\mathrm{km\,s^{-1}}$ is characterized by complete dust vaporization, deep crater formation and fast secondary solid ejecta production [396–399]. Such impacts are routinely realized in the laboratory with light gas guns, laser ablation systems and electrostatic accelerators [400]. They share common physics with RE-driven explosions, as evidenced by their reliable modeling with PD [401, 402] or SPH [403, 404]. Given the availability of experimental data, they can be employed to fine-tune and enhance the predictive power of tools that simulate RE-driven explosions.

Surrogate energy deposition profiles. Even when considering only the thermal PFC response, the full workflow is too computationally heavy for scoping studies. It is important to discern whether REs lead to PFC melting without costly code-chains. Energy deposition maps (on a semi-infinite solid) for every tokamak relevant energy, impact angle, magnetic field combination can act as basis states that enable the approximate reconstruction of any realistic RE energy deposition map by superposition. Given the large number of combinations, interpolations are unavoidable. One-dimensional heat conduction solvers can then be coupled with codes that model the RE impact on the vessel wall (see e.g. recent JOREK code calculations [405]) allowing fast estimates and identifying cases of interest for more detailed coupled 3D MC and FEM simulations.

Concluding remarks

Modeling of RE-driven damage in brittle materials with no liquid phase has largely progressed benefiting from controlled RE-impact experiments on graphite carried out in DIII-D. The thermo-elasticity equations supplemented with the maximum normal stress brittle failure criterion have provided an adequate description of the PFC response up to the onset of fragmentation. It is expected that the state-of-the-art of the modeling can be successfully extended to the explosive process by coupling a traditional FEM analysis of the continuum geometry to a more sophisticated analysis of the debris generation (SPH and ALE formulations). Modeling of RE-driven damage in W, which is ductile at elevated temperatures with a stable liquid phase, remains to be addressed. The W compressible hydrodynamic and viscoplastic behavior can be captured by a multiphase equation of state coupled with a multiphysics strength material model. Any progress has been impeded by the absence of controlled RE-impact tokamak experiments on W. The construction of an electron beam material testing facility that replicates RE impacts would speed up the evolution of high fidelity numerical models and the development of innovative wall designs.

The long term goal should be to translate set-ups that are currently incorporated in commercial general purpose MC and FEM software packages to a stand-alone open-source multi-physics code that is dedicated to predictions of RE-driven PFC damage.

10. Neutron production and activation

M Houry[1], *Y Peneliau*[1], *J Eriksson*[2] *and R Villari*[3]

[1] CEA, IRFM, F-13108, Saint-Paul-lez-Durance, France
[2] Department of Physics and Astronomy, Uppsala University, SE-75237 Uppsala, Sweden
[3] Nuclear Department, ENEA, Via E. Fermi 45, 00044 Frascati, Rome, Italy

Status

Neutron production and PFC activation by RE impacts. REs may activate the first wall and divertor components as observed in the tokamaks FT [50], TFR [406], PLT [407]. This might cause a non negligible dose rate in in-vessel components. The activation comes both directly from photonuclear reactions and from neutrons produced by the latter reactions [408]. The doses induced by REs are likely to be subdominant in experiments with significant fusion power. However, in experiments with limited fusion power such as the startup phase of ITER or present small- to medium-sized machines, the dose induced by REs could overcome the dose from fusion neutrons. Neutron production and PFC activation may also be exploited to constrain and validate RE impact models. This section will illustrate these aspects in particular by describing recent and ongoing work on WEST.

RE beams in WEST. During WEST disruptions, RE beams carrying a current exceeding 100 kA and with an energy spectrum extending beyond 10 MeV can be generated. WEST diagnostics allow observing its formation and evolution via e.g. IR tangential imaging of synchrotron radiation and a direct IR view observing the RE crash onto the divertor, see figure 25(a). Moreover, activation of W PFCs has been detected during post mortem analysis, as presented in figure 25(b).

Figure 26 shows key parameters recorded during pulse #58005, where a RE event occurred. The plasma current features a plateau after the start of the disruption, indicating a RE beam duration of about 10 ms. Then the RE beam crashes onto the divertor, causing the current to drop to zero. The neutron rate measurement shows a sharp peak at this moment, indicating nuclear reactions with neutron production. Magnetic diagnostics provide the radial localization of the RE beam (the bottom plot). In this specific case, the measured position of the beam aligns with the impact location shown in figure 25.

Gamma spectroscopy measurement on the W components of the WEST divertor reveals spectral lines that can be attributed to ^{181}W . The spectrum shown in figure 27 clearly displays five peaks around 60 keV, identified as originating from ^{181}W. The formation of this radionuclide, with a half-life of 121 d, can only result from nuclear reactions leading to the transmutation of ^{182}W into ^{181}W, either through photoneutron reactions or $(n, 2n)$ reactions. MC simulations of the measurement configuration with the HPGe detector have been carried out in order to calculate the scaling factor between the W activity in the monoblock and the number of gamma ray counts. Conservatively assuming that the gamma source is homogeneous in the material leads to a possible 50 Bq g^{-1} specific activity for the most activated monoblock for which the gamma rays counts measurement was 10 cts s^{-1}, shown in figure 25(b). Additional spectrometry measurements were conducted to analyze the spatial distribution of ^{181}W within the component. Using shielding screens, gamma spectroscopy was performed in 7 mm depth increments. The results show a clean absence of radioisotopes beyond 7 mm, indicating that REs impact the W component at a shallow incidence angle. Thanks to the spectroscopy conducted on one divertor sector (1×0.5 m^2), providing an activity map, it is observed that RE crashes lead to the formation of a narrow beam, approximately 5 cm in width, which toroidally propagates at a certain radial distance. In WEST, the corresponding activation zone is influenced by the ripple effect and thus appears with a periodic discontinuity.

The activation in W is a 2-step process. The RE impact can produce high energy bremsstrahlung photons due to slowing down of the REs. Then, high energy photons can have photonuclear reactions with the nuclei of the material: (X, n) reactions. The latter are threshold reactions happening above 8 MeV in W, in which photons can produce neutrons as well as W radioactive isotopes as the reaction removes one neutron or more from a stable nucleus. Regarding W isotopes, photonuclear reactions produce two radioisotopes, ^{181}W and ^{185}W, by removing neutrons to the initial stable isotopes. ^{181}W is the most contributing isotope to dose rate because its x-ray decay intensities per disintegration are of the order of dozens of %, whereas x-ray decay intensities of ^{185}W are of the order of 0.01%. However, regarding neutron production, as the photonuclear cross sections and the relative fraction of parent isotopes are similar, they contribute almost equally.

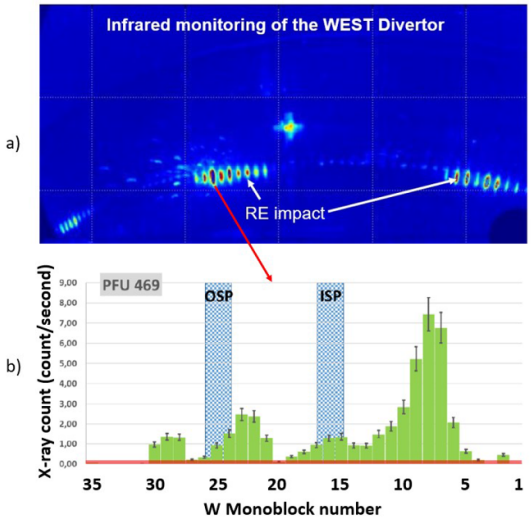

Figure 25. Infrared view of a RE beam impact in WEST for pulse #58005 (a). Post mortem measurement of decay gammas in the monoblocks of the plasma facing unit #469 on the lower divertor of WEST possibly due to multiple impacts (b).

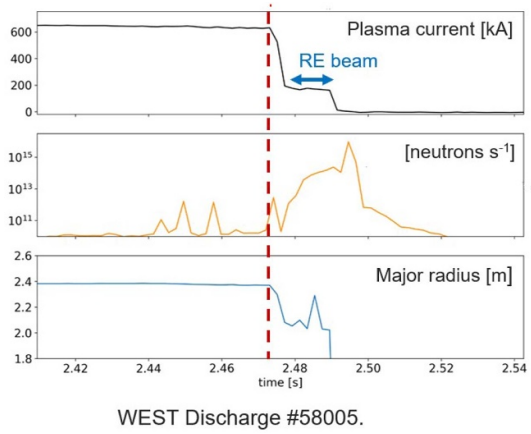

Figure 26. Parameters during disruption of WEST for pulse #58005. Current in the plasma (in kA). Neutrons (D–D and RE) measured in the vacuum vessel thanks to fission chambers (in n s^{-1}). Localization of the electron current in the vacuum vessel (radius in m).

MC simulation of the EM shower. Simulations of PFC activation by RE impacts consist first in simulating electron transport and the EM shower in the material. This is usually performed thanks to specific MC codes like MCNP-6 [409], TRIPOLI-4 [410] and Geant4 [357–359]. These codes simulate the production and transport of bremsstrahlung photons. They can implement the photonuclear reactions in the same simulation, producing neutrons that can themselves be transported and produce activation on one hand, or new secondary photons due to neutron reactions like radiative capture on the other hand. Photonuclear reactions are usually inelastic reactions (γ, n') (also noted as (X, n) in this article) in the energy range of interest. Fission reactions (γ, f) or (at high enough photon energy) neutron multiplicity reactions $(\gamma, 2n)$, $(\gamma, 3n)$ are also possible.

Photonuclear reactions in W. Parametric studies on the incidence energy and angle of the REs help to elucidate the phenomenon of activation. Figure 28 shows the activation rate (i.e. the number of reactions per second and cm^3) due to 12 MeV electrons on a 5 mm mesh for a tangential incidence of the electron (a) and for a normal incidence (b) in bulk W. The activation rate is calculated for a source of 1 e^- s^{-1} and the activation rate ranges from 10^{-5} (red) to 10^{-9} $cm^{-3} \cdot s^{-1}$ (blue) on the figure (logarithmic scale). Both configurations are of interest in a tokamak as REs can crash tangentially on the divertor but also normally on an antenna protection limiter for instance. Other angles should also be considered as the RE pitch angle and shape of the W components in a tokamak can vary. A finer mesh analysis with 0.05 mm large voxels shows that a pile-up phenomenon occurs. The latter is illustrated for 30 MeV electrons and normal incidence in figure 28(c), that presents a refinement of the distribution

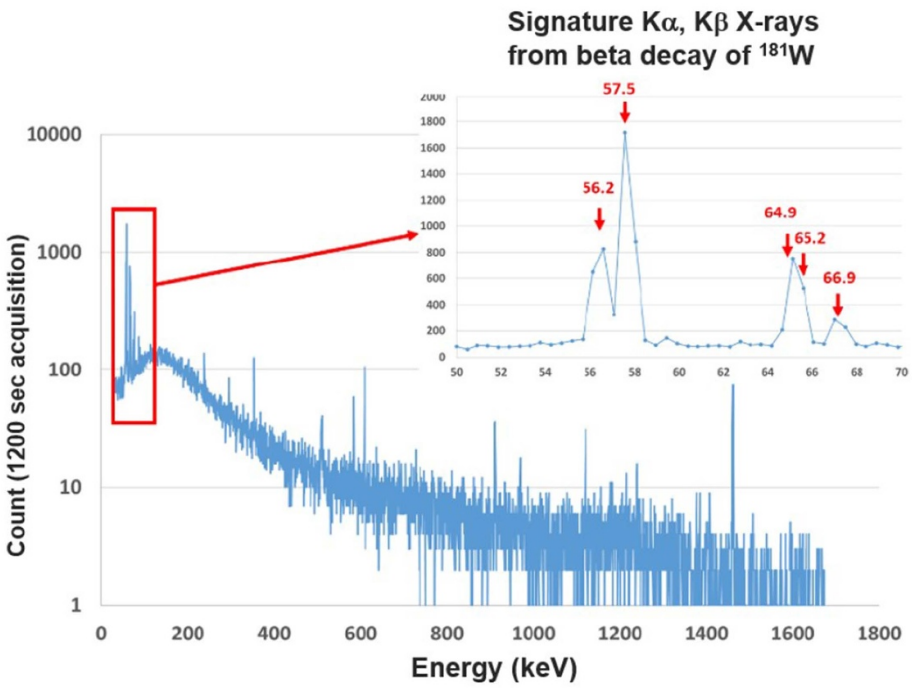

Figure 27. Spectroscopy of the WEST PFCs.

in the most activated voxel of the previous coarse mesh. The electrons produce bremsstrahlung photons in the first layers. The photons contribute to the activation rate in the following layers as well, as long as their energy is high enough to exceed the reaction threshold. When the electron energy loss is significant, the electron cannot produce photons with energy above the threshold, and from layer to layer, the number of photons able to contribute to photonuclear reactions decreases. It should be noted that the refinement of the mesh is important as the W linear attenuation coefficient for 60 keV gammas is 71 cm^{-1} and the gamma flux drops drastically with penetration.

Neutron production. An analytical formula for the (photo)neutron yield was proposed by Jarvis *et al* [51]. In early JET studies with a carbon wall and inconel vacuum vessel, the neutron yield for RE energies of $E_0 \gg 15$ MeV was given as $Y_n = \frac{E_0}{60\times 2.9\times 10^{-3}}$ n/e$^-$ (with E_0 in MeV). For a W wall, recent systematic radiation transport simulations were conducted with GEANT [411]. The energy spectra of photons and neutrons produced in electron collisions were calculated. Photoneutron production in W occurs at photon energies above 8 MeV. Neutron production increases with the electron energy, occurring in the 10–100 MeV range, with a 100 MeV beam generating fast neutrons (average energy 1.3 MeV). High-energy neutrons from these interactions escape the target and may impact tokamak equipment. For electron energies above 20 MeV, many neutrons exit the 10 mm thick W wall in the simulations of [411]. If neutron production occurs in the initial target layers, slowing down and thermalization may cause neutron activation in PFCs.

Activation calculation schemes. Like for standard dose rate calculations based on D1S [412] or R2S [413] schemes, appropriate methodologies can be implemented to calculate activation dose rates. From the electron simulation, it is possible to calculate a photon (γ, n') reaction rate map as it was done in the investigations for the WEST tokamak and the activation of ^{181}W. It is also possible to calculate neutron production maps and neutron production spectra to define photoneutron sources for further neutron simulations. From the activation map, a secondary decay photon source is defined for all the radionuclides (like for ^{181}W here below) from the photon (X, n') activation rate at the end of the beam:

$$S_\gamma(\vec{r}, E_\gamma) = \lambda^{^{181}\mathrm{W}} \times \tau^{^{182}\mathrm{W}(X,n)^{181}\mathrm{W}}(\vec{r}) \times I_{\mathrm{e}^-} \times f(E_\gamma) \tag{10}$$

where $\lambda^{^{181}\mathrm{W}}$ is the decay constant of the radioactive isotope ^{181}W in s^{-1}, $\tau^{^{182}\mathrm{W}(X,n)^{181}\mathrm{W}}$ is the activation dose rate of ^{181}W production in in electron$^{-1}\times\mathrm{cm}^{-3}$, I_{e^-} is the total number of electrons impacting the PFC, and $f(E_\gamma)$ is the X and γ energy distribution in MeV^{-1}.

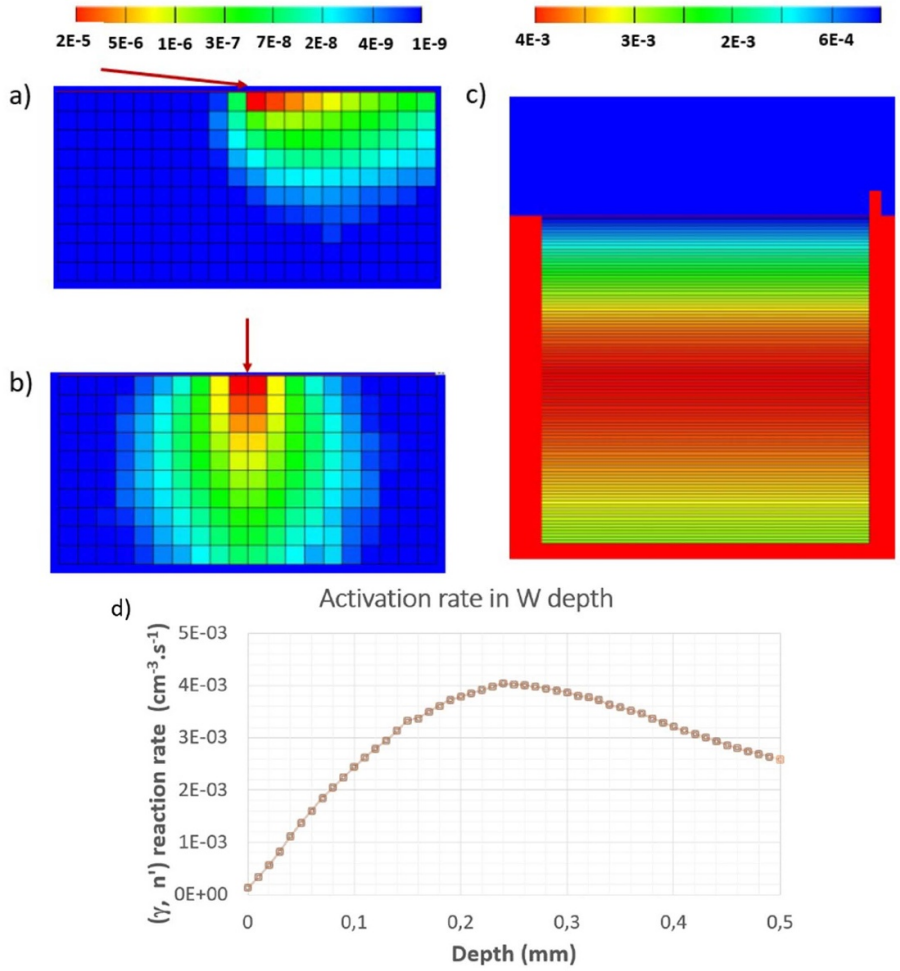

Figure 28. Activation rate map in W for 12 MeV electrons impinging tangentially (a) or normally (b) for a 5 mm voxel size. Activation rate map in W for 30 MeV electrons for a 0.05 mm voxel size in Z axis and 5 mm in other axes (c). Reaction rate profile corresponding to the former activation rate map (d).

Current and future challenges

Extrapolation of W activation by REs to ITER. ITER DD first plasmas during SROs are designed to induce a low dose rate in the vacuum vessel in order to allow hands-on maintenance during the phase of first wall replacement between SRO and DT-1. Thus, the activation of the first wall due to RE beams in the ITER vacuum vessel requires attention. This had already been stated and assessed in the context of the 2016 baseline [414]. The extrapolation from WEST to ITER is not straightforward as the RE beam characteristics differ. The expected RE current will be one to two orders of magnitude larger, and the number of photons produced above the W photonuclear reaction threshold could be significantly higher depending on the RE energy, substantially affecting the contact dose rate. On the contrary, the RE wetted surface is expected to be larger due to the machine size and the mitigation strategy [35, 414]. Thus, the effect on contact dose rate could be one order of magnitude lower. It is also expected that more bremsstrahlung photons will have an energy higher than 25 MeV, where the (γ, n) cross sections significantly drop.

Diagnostics. The neutron rate monitors employed to measure DD and DT neutron emission from tokamaks can also often pick up the signal from photoneutrons, and can thus provide direct evidence of the formation of REs from the plasma (see e.g. figure 26 and [78, 415]). However, even more detailed information about the interaction between REs and PFCs could potentially be available if the energy spectrum of the photo-neutrons could be measured too. This is a challenging task that would require a neutron detector with spectroscopic capabilities, capable of measuring a short burst of photo-neutrons in a significant background of x-rays and gamma-rays. Furthermore, in order to minimize the amount of scattering the photo-neutrons undergo before reaching the detector, the detector would need to view the machine through a suitably positioned diagnostic port and care must be taken to ensure that the

field of view of the detector covers the part of the PFCs where the RE beam is expected to hit. Hence, the first step in order to install a photo-neutron spectrometer on a given machine would be a more detailed modeling/assessment of the expected characteristics (time duration, location, energy range) of the photo-neutron emission, in order to determine more specific design requirements of the spectrometer. Depending on the spatial constraints of the machine, both compact spectrometers—such as scintillators and semiconductor detectors—and more specialized instruments—such as time-of-flight and proton recoil systems—could be considered and evaluated; see e.g. [416] for an overview of different neutron spectroscopy techniques. In experiments where photo-neutrons are the only source of neutron emission (i.e. if the plasma does not contain D or T), the energy spectrum could potentially also be reconstructed from activation measurements [417].

Photonuclear data. Available photonuclear data are ENDF/B-VII [418] or ENDF/B-VIII [419] more recently, JENDL-5 [420], IAEA-PD-2019 [421] and TENDL-2023 [422] data. Some issues arise with these various sources. The first issue is the energy range covered by the evaluation process. ENDF/B-VII or ENDF/B-VIII provide inelastic cross sections in the range 8 MeV–30 MeV only. Other libraries cover the energy range until 200 MeV, but IAEA and JENDL provide production data for the sum of all inelastic reactions, without distinction of (γ, n'), $(\gamma, 2n)$, ... In ITER or larger tokamaks, higher electron energies are expected and thus modeling may lack crucial information for the simulations with ENDF/B series. Moreover, a significant validation effort [423] should undertaken for the isotopes of interest for fusion applications, and mainly for W isotopes due to anticipated use of this material as first wall in reactors.

Accounting for the magnetic field. As discussed in section 8, presence of the magnetic field leads to redeposition of the backscattered electrons due to gyration. It is of utmost importance to take into account this effect and a validation campaign should also be carried out with specific benchmarks.

Specific D1S methodology development. As it was done for neutron activation for the plasma D-T source, similar activation schemes should be developed. The D1S methodology [424, 425] could be applied to photons interacting with the material. Each time a photon has a photonuclear reaction and produces a radioisotope, the code simulates the decay photon production and assesses the subsequent dose rate. Specific libraries are needed in which the production of prompt neutrons due to photonuclear interactions is replaced by decay photon production. The same time factors as the ones used for plasma neutrons are compliant for X or gamma simulations for the specific radioisotopes.

RE dose rate in ITER and further fusion reactors. As stated previously, the assessment of the possible impact of RE activation in ITER is relevant with regard to the operations planned between the SRO phase and the DT-1 phase. The components to be analyzed are mainly the divertor and the first wall, both of which have been made of W since the re-baselining of ITER. Subsequently, depending on the assembly schedule for the more voluminous machines, this work will also be carried out on DEMO or other facilities.

WEST dedicated experiment. A dedicated experiment was conducted at WEST in April 2025 to test the control [426] of the RE beam position on the facility. It opens the opportunity to plan a specific activation and neutron production experiment in a sacrificial component in order to have experimental results for the validation of the complex simulation process of the phenomenon. The measurements will consist in activation foils dosimetry to characterize the neutron flux and potentially to derive the neutron spectrum at different locations, but also in activated components spectrometry and dose rate measurement. The final aim of the experiment is the validation of the MC-based computational methodology.

Concluding remarks

REs and the subsequent photoneutron production not only generate damages to the components but also contribute to their activation. Recent spectrometry analyses on WEST divertor components impacted by RE beams have shown W radionuclide activity. The measurements performed on these components (decay X ray counts) at different locations can serve as experimental data source for obtaining information on the characteristics of the RE beam. The activity and subsequent dose rate in a larger scale fusion reactor are expected to be much lower than the ones due to the direct plasma neutron interactions in the full power D-T pulses. Nevertheless, the phenomenon deserves being further studied as it can be significant enough in the early stages of the reactor operations, before D-T nuclear phase.

11. ITER perspective

F J Artola[1] *and R A Pitts*[1]

[1] ITER Organization, Route de Vinon-sur-Verdon, CS 90 046, 13067 St. Paul Lez Durance Cedex, France

Status

RE impacts at ITER. As discussed in section 6, RE beams in ITER could deposit kinetic energies on the order of tens of MJ and magnetic energies of hundreds of MJ, with typical average RE energies ∼20 MeV. A workflow based on the codes DINA-SMITER-GEANT4-MEMENTO has shown that energy densities of 150–200 kJ per tungsten first wall panel (FWP) apex results in melt depths of 0.5–1.5 mm [10, 364]. Assuming a 9 MA RE beam carries 24 MJ of kinetic energy [2], and neglecting additional magnetic energy conversion (i.e. RE energy is linear with RE current), 200 kJ corresponds to a RE current of 75 kA if all energy were deposited on a single FWP apex. Alternatively, uniform deposition across the 36 FWP apexes in one toroidal row would correspond to a RE current of 2.7 MA.

Figure 29 illustrates the scenario used to provide the RE inputs necessary for the study. The DINA simulation results in a ∼9 MA RE beam formed during an upward CQ, following the conversion of the available magnetic energy into RE kinetic energy during a slow termination event (figure 29(a)). The beam impacts FWP #8 at the top of the vessel, with geometry and field line tracing (via SMITER) used to define the impact location and area (figure 29(d)). The impact area was taken at the time instant corresponding to $q_{95} = 2$, where the beam is expected to terminate after crossing the MHD stability limit. The RE energy distribution is taken as exponential with $E_0 = 15$ MeV (range 1–50 MeV), and the beam width Δ_{RE} (or deposition depth) is fixed at 4 mm, consistent with the Larmor radius at this value of E_0. In addition, all electrons were assumed to strike at 5° grazing angle based on the magnetic field geometry provided by DINA (figure 29(e)). Such inputs were encouraged by a successful study at JET [57], in which the same workflow was applied to pulse #86 801 and the results were qualitatively consistent with the post-mortem RE damage analysis. The assumption on the beam width is consistent with the RE Larmor radius at ITER as minimal possible width. In this respect, it is expected that for RE pitch angle distributions occurring when $E \gg E_c$ [225] and $E \sim E_c$ [224], the average Larmor radius of 20 MeV electrons for full ITER toroidal field operation exceeds 2 mm.

Nevertheless, MHD termination events may lead to considerably larger energy deposition areas as in the case of benign RE termination. To assess this, the study summarized in figure 29 was repeated replacing the DINA-SMITER components by JOREK MHD calculations and RE orbit tracing on the resulting time-varying 3D fields [2, 3]. In this case, the RE deposition area is notably much broader as shown in figure 22. When this input was considered, RE beams with 24 MJ kinetic energy deposited over 1 ms, and a maximum of 1.2 MJ per FWP apex, yield melt and vaporization depths of 1.1 mm and 28 μm respectively [364]. For that case, a mono-energetic distribution considering 26 MeV REs and a single pitch of $v_{\|}/v = 0.99$ were used for the orbit tracing, but RE distributions expected during the avalanche phase were also analyzed [3, 364]. In common with the calculations for the scenario shown in figure 29, these studies also indicate significant heating at the PFC cooling interface layer (CuCrZr) for an 8 mm W armor thickness (which is the nominal thickness chosen for the original Be first wall armor). Too high a temperature at this bond interface constitutes a risk for the initiation of water leaks, which would entail severe cost and operational consequences. Given that ITER RE beams may deposit substantially more energy than assumed in the scenarios modeled thus far, even a handful of such events may not be tolerable.

Most RE impact studies at ITER will take place during the SRO phase, where the disruption mitigation system (DMS) will be commissioned and optimized up to 15 MA before the beginning of fusion power operation. During this phase, an inertially cooled temporary first wall (TFW) will facilitate RE impact studies without the risk of water leaks [10]. However, particular caution is required to avoid RE impact on the divertor, which is actively cooled and will be in place from the beginning of the SRO phase. For the final, actively cooled W FW, the code workflow studies described above have been used to recommend an increased thickness of W armor in specific regions of the main chamber on which the most probable RE impact is expected [10, 364]. There is, however, always a trade-off between the conflicting requirements of stationary and transient power handling and cost/design complexity. Increased armor thickness can be very effective at preserving lifetime if the deposited RE energies are within a certain range. Once these energies are surpassed, the worst affected areas of the FWPs will still never be capable of sustaining many impacts before panel replacement is required. Effective RE avoidance and

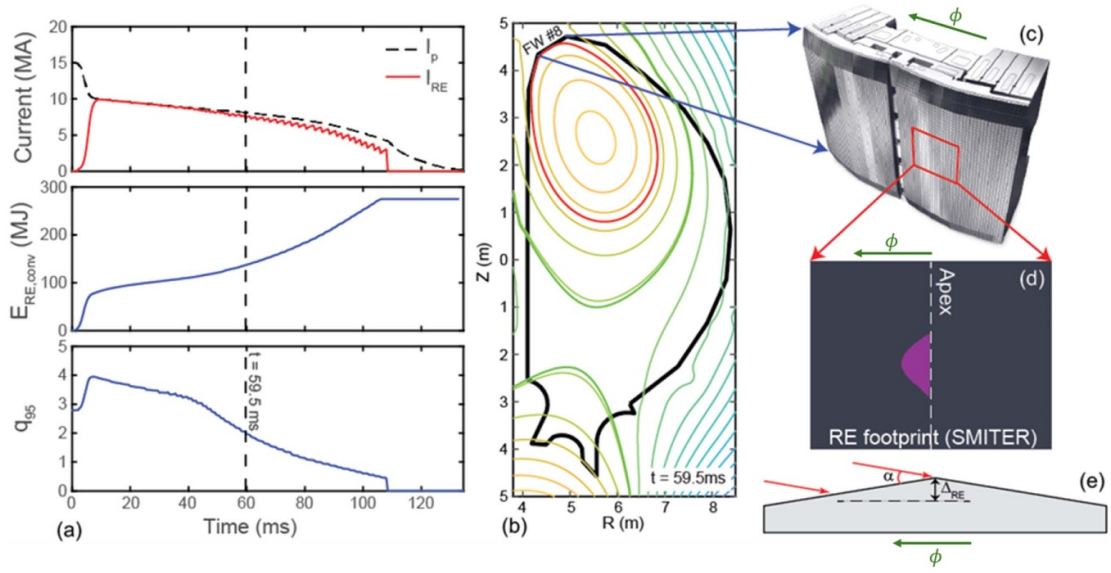

Figure 29. Composite showing the key input parameters for the RE impact simulations performed with the DINA-SMITER-GEANT4 -MEMENTO code workflow: (a) DINA simulation (IMAS disruption database shot 100097, run 1) including RE conversion during an upward-going CQ at 15 MA, showing the RE current and magnetic energy conversion with $q_{95} = 2$ reached at $t = 59.5$ ms; (b) magnetic equilibrium at $q_{95} = 2$ assumed as the instant at which the RE beam is destabilized with impact on FWP #8; (c) blanket module CAD model illustrating the double winged apex structure of the FWP; (d) SMITER field line tracing calculation of the RE beam wetted area for $\Delta_{RE} = 4$ mm; (e) schematic representation of the FWP apex modeled as a simple rooftop with given fixed RE beam impact angle. Green arrows in (c)–(d) represent the toroidal direction. Reproduced from [10].

mitigation strategies will thus always be mandatory on ITER and achieving this is a major component of the re-baselined ITER Research Plan [39].

RE avoidance at ITER. The first line of defense to minimize RE impact is RE avoidance. Its primary challenge in ITER arises from the avalanche generation mechanism, producing seed amplification factors many orders of magnitude higher than those in present tokamaks. The avalanche multiplication scales exponentially with plasma current, following $10^{\alpha_{av} I_p}$ [191], where α_{av} is estimated to be on the order of $1\,\mathrm{MA}^{-1}$ [42, 46]. This implies that each additional MA of I_p-decay can increase the RE current by roughly an order of magnitude. Simulations with JOREK incorporating vertical displacements during the CQ suggest a reduction of the amplification from $\sim 10^{16}$ down to $\sim 10^{10}$ [247]. Although this reduction eases RE avoidance strategies, such an amplification would still amplify tritium and Compton-induced RE seeds (of the order of 10mA [42, 46]) to multi-MA beams.

Achieving electron densities exceeding $3 \times 10^{22}\,\mathrm{m}^{-3}$, required for avalanche suppression, is expected to be unfeasible. Assimilation is limited by pre-disruption thermal energy and by drift effects such as plasmoid motion and the rocket effect [46, 427]. Even if sufficient material were assimilated, strong plasma recombination could lead to excessively short CQ durations, leading to intolerable eddy current loads on the ITER blanket modules. Furthermore, the unfavorable ratio between total (free + bound) and free electrons is expected to enhance, rather than suppress avalanche growth [428].

Given the challenges discussed above, alternative mechanisms for RE loss and deceleration are necessary. As outlined in section 5, whistler waves could potentially deconfine REs; however, their excitation requires post-TQ electron temperatures of at least 25 eV, which may not be achievable in mitigated ITER plasmas. With regard to externally applied magnetic perturbations, the ITER design is now frozen and does not include passive 3D coils for RE de-confinement that have been proposed for other devices [252–254]. The potential use of the existing RMP coils for this purpose was studied in [250], which showed only partial deconfinement. Improved performance may, though, be achievable in later stages of the CQ, when I_p is lower and with optimized RMP configurations. Intrinsic MHD activity during this phase may also lead to significant RE deconfinement. Simulations with JOREK using realistic CQ parameters have shown encouraging results for RE suppression [323, 429], though the post-TQ profiles used in these studies were ad hoc and are currently being revisited. Finally, an alternative mitigation strategy involving the injection of a train of solid fragments to deplete the RE seeds during the CQ has been proposed [430] and is under re-evaluation for application in ITER.

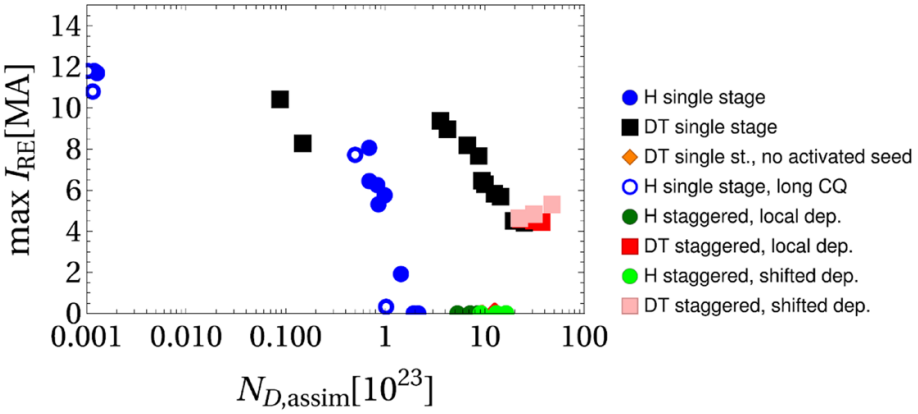

Figure 30. Representative RE current (linear) vs assimilated material (logarithmic). The cases marked with 'H' (hydrogen) correspond to scenarios without activated RE sources (Compton and tritium), while the DT scenarios contain all source (except the orange diamonds). Note that the ITER DMS will inject hydrogen instead of deuterium, as used in these studies. However, isotopic effects are not expected to affect RE generation. Reproduced from [46]. CC BY 4.0.

In view of the current uncertainties in controlling RE losses, the ITER strategy for RE avoidance primarily focuses on suppressing RE seed generation through H injection. Simulations using the DREAM code for various ITER scenarios mitigated by SPI indicate that Dreicer and hot-tail seeds can be sufficiently reduced to achieve full avoidance of RE avalanches if sufficient plasma densification is achieved as shown in figure 30 for an L-mode Hydrogen scenario (blue circles). This suppression is enabled by a two-stage plasma cooling process [46, 431, 432], consisting of an initial dilution phase at nearly constant thermal energy, followed by a rapid radiative collapse. However, the triggering of the TQ in DREAM remains based on an ad hoc criterion, and the associated uncertainties need to be carefully assessed. In addition, the effects of plasmoid and fragment (rocket) drifts must be incorporated more realistically to refine predictions of seed suppression efficacy. While tritium seeds may be suppressed by sufficient plasma densification and the increase of the critical energy beyond 18.6 keV, Compton generated electrons can have energies in the range of MeV [42], and RE avoidance does not therefore seem possible in the absence of CQ transport. As shown in figure 30, even in the best assimilation conditions for nominal DT H-mode plasmas, multi-MA beams are formed.

RE mitigation and termination in ITER. In the event of multi-MA RE beam formation in ITER, vertical control of the plasma is expected to be lost unless more than two-thirds of the pre-disruptive I_p is converted into RE current [433]. For lower RE current fractions, vertical instabilities will result in RE beam impact on the PFCs irrespective of the RE current decay time (see section 6). Given the inherent difficulty of RE position control and ramp-down, the primary strategy to mitigate RE impact is H injection into the RE beam to induce plasma recombination and impurity flush-out. This process facilitates a benign termination through an MHD-triggered collapse, as discussed in section 7. Preliminary studies suggest that a single H ITER-sized pellet could be sufficient to access this benign termination regime for RE impact [222], but its physics basis is not yet fully established. However, achieving compatibility between RE avoidance and RE mitigation remains challenging, particularly due to plasma re-ionization above an upper neutral pressure limit, which may compromise the benignness of the termination [434].

RE relevant diagnostics at ITER. The assessment of RE impact on PFCs at ITER relies on a combination of diagnostics. IR cameras and thermography systems, covering approximately 70% of the divertor and FWP surfaces [435], will provide surface temperature measurements with a time resolution of the order of 1 ms to identify RE deposition patterns. RE energy deposition could be diagnosed with thermocouples installed in the TFW, if present at the impact location. In the event of significant RE impact, post-shot inspections will be performed using the In-Vessel Viewing System, which provides full coverage of the divertor and FWPs with spatial resolution below 3 mm. During the first fusion power operation phase (DT-1), the in-vessel lighting system will also support damage evaluation. Post-mortem inspection opportunities will be available during the decommissioning of the TFW following the SRO phase.

During SRO, the primary diagnostic for RE detection will be the HXRM, which is expected to detect RE currents as low as 10 kA in the 0.1–20 MeV energy range and provide key insights into the RE distribution function up to 100 MeV [436, 437]. Additional RE detection will be attempted using the radial

x-ray camera, as well as ECE and visible/IR cameras, which can capture synchrotron radiation to further characterize the RE distribution (see section 4). Following the SRO phase, the HXRM is unlikely to be operational, and its function will be taken over by gamma-ray spectrometers [438]. RE losses will also be monitored using radial and vertical neutron cameras [439].

Current and future challenges

Given the high risk of RE generation and its potentially severe consequences for ITER, it is essential to quantify the damage caused by RE impact on PFCs. Accurate damage assessments will be critical for defining operational limits and setting RE avoidance and mitigation targets to ensure PFC integrity.

This is necessary to prevent severe PFC damage and/or water leaks due to RE impact that would significantly delay the ITER DT programme because of the required shutdowns for PFC replacement, recommissioning and reconditioning. During the SRO phase, dedicated experiments with controlled RE beams at low plasma current will be conducted to validate predictions of RE impact and mitigation. But, it remains unclear how results from low-current experiments will extrapolate to full-current operation, where intentional RE impacts would likely not be permissible. A key challenge is the development of a low-I_p RE scenario triggered by neon SPI, since such beams have not yet been successfully generated in existing tokamaks using SPI. Instead, they have only been achieved with MGI, a system that will not be available at ITER. If SPI cannot reliably generate such scenarios, the three upper port SPI injectors at ITER may be used for MGI-like injection via enhanced pellet shattering and subsequent gas production. However, since the pellet size is fixed and only three injectors are available, the flexibility in selecting the amount of injected material is limited compared to traditional MGI systems [440, 441].

The general challenges of modeling RE impacts have already been outlined in previous sections, including RE characteristics prior and during the impact (sections 5–7) and the complex thermo-mechanical response of the PFCs (section 8). The multi-physics nature of RE-MHD coupling, especially when impurities, kinetic effects and losses are included, is particularly difficult to model. At ITER, the long CQ duration ($\sim$100 ms), driven by machine size, further complicates the problem by pushing current solvers to prohibitive computational limits; even simplified fluid CQ MHD simulations with today's solvers require millions of core-hours. Development of more efficient and scalable sparse-matrix solvers would be highly beneficial in this respect.

On the materials side, the high RE energy deposition expected at ITER may require the implementation of advanced PFC response workflows capable of capturing phenomena such as fracturing and explosive material failure approaches not yet applied to ITER. If such fragmentation occurs, the reintroduction of PFC debris into the plasma could significantly alter both RE dynamics and MHD behavior, creating feedback loops that complicate impact modeling and prediction. Such RE beam–wall interaction, will probably be very localized, posing even higher complexity for modeling. Finally, evaluating cumulative damage from multiple RE terminations also presents challenges, since evolving surface geometry may strongly influence subsequent energy deposition and failure thresholds.

Due to current uncertainties on RE avoidance and impact at ITER, a stepwise increase in plasma current and magnetic field during SRO will allow robust development of RE control strategies, with controlled RE impacts directed to the inertially cooled TFW using the in-vessel vertical control coils to reduce risk of water leaks on the actively cooled divertor. However, it cannot be ensured that all disruptions will be successfully guided upward [39]. Further analysis is therefore needed to assess RE impact on divertor structures, particularly the outer baffle, which is the most likely impact location.

Dedicated experiments during DT-1 will progressively assess the impact of tritium and Compton-induced RE seeds. Approximately one month of operation has been allocated early in DT-1 to demonstrate that the ITER DMS can effectively mitigate disruptions up to 15 MA in hydrogen–tritium (HT) plasmas, retiring the risk from tritium β-decay seeds before fusion power operation [39]. The influence of Compton seeds will be evaluated through targeted DMS pulses during the staged fusion power ramp-up in the development of DT H-mode plasmas. If efficient thermal and EM load mitigation proves incompatible with RE avoidance at ITER, compromises may be necessary (e.g. such as reducing the injected neon quantity and accepting lower radiated energy fractions) to support RE suppression by limiting the avalanche-enhancing effect of bound electrons from neon. Furthermore, the RE benign termination scheme may not compatible with the quantity of injected material for RE avoidance due to an upper neutral pressure limit.

Concluding remarks

Due to the significant challenges in achieving reliable RE avoidance at ITER, assessing RE impact remains essential for validating models, defining operational limits, and managing disruption budget consumption. Although challenging, continued efforts to develop predictive workflows for RE impact will be critical to define tolerable RE events and refine mitigation strategies. These activities are necessary to prevent excessive component damage, avoid operational delays, and ensure ITER meets its research goals within acceptable RE exposure limits.

12. Future large machines perspective

R Ding[1], *G Pautasso*[2] *and R A Tinguely*[3]

[1] Institute of Plasma Physics, HFIPS, Chinese Academy of Sciences, Hefei 230031, People's Republic of China
[2] Max Planck Institute for Plasma Physics, Boltzmannstrasse 2, 85748 Garching, Germany
[3] Plasma Science and Fusion Center, Massachusetts Institute of Technology, Cambridge, MA, United States of America

In this section, we focus on REs and their impact in future tokamaks, planned or under construction, around the globe, while ITER is discussed separately in section 10. Fast electron populations in stellarators with non-zero toroidal currents [442] or levitated dipoles [443] are outside the scope of this article.

Status

In Asia. The main parameters of the the China Fusion Engineering Test Reactor (CFETR) are major radius $R_0 = 7.2$ m, minor radius $a = 2.2$ m, toroidal magnetic field at major radius $B_0 = 6.5$ T, plasma current $I_p = 13.78$ MA, and fusion power $P_{fus} > 1$ GW [444]. Recent simulation results for a typical plasma discharge in CFETR reveal that a majority of plasma current, I_p, would be converted into RE current during a disruption. The assumed pre-disruption plasma parameters are based on a reference hybrid mode 1 GW scenario, with $I_p = 13.78$ MA and electron density $n_e \sim 9 \times 10^{19}$ m^{-3}. The pre-disruption loop voltage is 25 mV, the characteristic TQ duration is estimated to be 1 ms, the post-disruption electron temperature is $T_e \sim 10$ eV, and the electron density is 10 times the pre-disruption density. $Z_{eff} \sim 4$ is assumed during disruptions, and l_i is the same as in the ITER 15 MA scenario. The majority of the RE seed is provided by the hot-tail mechanism. RE losses are considered as an overall reduction of the hot-tail seeds to a fraction of 0.1%, 1%, and 10%. RE calculations based on these assumptions are shown in figure 31. Almost 75% of the plasma current is converted into RE current during the disruption, with RE seeds of tens of kA leading to ∼10.6 MA of RE current when 90% RE seed loss is considered. However, even with 99.9% loss of the RE seed, the RE current is estimated to be ∼8 MA due to the high avalanche gain.

In Europe. The EU-DEMO fusion power plant is a project aimed at designing a tokamak that can produce a few hundred MWs of electricity, demonstrate reliability and availability, and work with a closed fuel cycle. The EU-DEMO 2018 design [446] foresees a plasma with $R_0 = 9.07$ m, aspect ratio $A = 3.1$, and $I_p = 17.75$ MA. Because of the large current and associated high avalanche gain, the formation of a substantial RE beam is expected in every disruption. The different types of disruptions expected in DEMO are described in [447] and follow the guidelines of the ITER Physics Basis [75].

The study of RE generation in DEMO [448, 449] was adapted from the simulations done for ITER [42]. For the shortest CQs following pure Ar injection for disruption mitigation, a substantial RE current of 13–16 MA forms. For the longest CQs, RE currents up to 15–17 MA are estimated after Ar and Ne injection, due to tritium decay, Compton scattering, and hot-tail mechanisms. The 0D simulations, carried out for deuterium injection up to ∼15 kPa m^3 (into a plasma volume of ∼2500 m^3), suggest that the formation of the RE current due to the tritium and hot-tail RE sources could be very efficiently controlled by injection of a sufficient amount of deuterium ($\geqslant$10 kPa m^3). In contrast, the control of the RE current due to the Compton scattering seed might require a substantially larger amount of deuterium ($\geqslant$20 kPa m^3 corresponding to the so-called 'critical density').

A DMS has not yet been developed for the EU-DEMO. A preliminary study [450] pointed out that RE suppression requires a volume-averaged density increase of the order of 4×10^4 (critical density), which should take place in a time interval of the order of 10 ms. In addition, the density increase must occur in the plasma center where the current density peaks and the toroidal electric field is maximum. It is unlikely that this is physically and technically doable. A RE beam would not be a danger if it were position-controlled to avoid interaction with PFCs and if its current were ramped down by the Ohmic system or by massive impurity injection. It is the interaction of the RE beam with structures and the slowing-down of the RE in the material that cause damage.

The temporal and spatial evolution of the RE interaction with the PFC surface must be known in detail to evaluate the damage. The EU-DEMO first wall protection relies on limiters placed on the wall at specific toroidal and poloidal positions, where a direct contact with the boundary of a disrupting plasma is expected. The engineering design and the integration of the upper limiter have been carried out with some detail in [451–453]. The rationale behind the design choices of the limiter sub-system

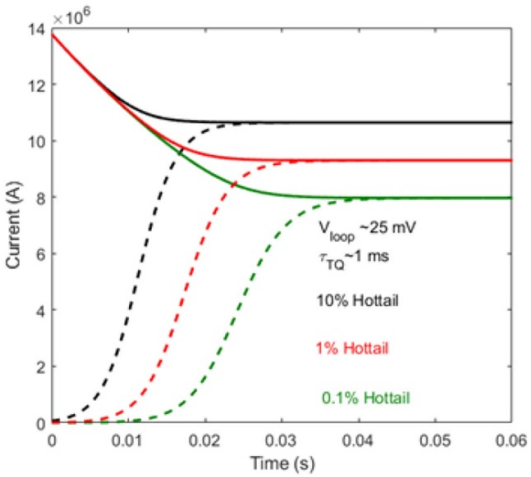

Figure 31. Evolution of plasma current and RE current during CQ phase in CFETR scenarios with $I_p = 13.78$ MA as predicted by simple 0D model [445]. The model considers seeds generated by Diercer mechanism, hot-tail mechanism, moreover, extra seeds provided by pre-disruption non-Maxwellian electrons are directly included in this primary phase, then, REs are multiplied by avalanche phase.

is supported by an extensive assessment workflow, based on neutronics and thermal- hydraulics evaluations, EM studies, and structural assessment, but does not yet include RE impacts.

Several numerical codes and related physics models are required to estimate the RE thermal load on the PFCs and the related damage. The different codes form a workflow, which delivers information needed to design the PFCs. The present workflow consists of (1) preliminary geometry (and material, later on) of the PFCs; (2) codes able to evolve the magnetic equilibrium; (3) a field-line tracing code, if not yet part of the codes above; (4) a RE kinetic model to evolve the RE energy distribution; (5) a RE-PFC interaction model; and (6) a code to simulate the PFC material's temperature evolution and eventual damage.

The codes CarMa0NL [454] and MAXFEA [455] typically provide the 2D evolution of the plasma equilibrium, which identifies the plasma-PFC contact areas and allows to position the limiters and to modify the magnetic equilibrium when needed. These codes have simple halo current recipes to be replaced in the future by more physics-based models. Nevertheless, they do not account for RE generation. The 3D field-line tracing codes PFCflux [456] and SMARDDA [457] calculate the thermal loads due to charged particles. They use as inputs magnetic equilibria, assumptions on power density crossing the separatrix, and the e-folding length for different power channels of the near and far scrape-off layer.

Since the whole equilibrium evolution determines the evolution of the plasma-PFC contact points—i.e. the RE deposition map – time-dependent equilibrium codes must take into account RE generation. The nonlinear MHD JOREK code can evolve the equilibrium with a halo region, while also modeling RE generation and losses. A recent simulation of an EU-DEMO plasma CQ is presented in [317]: Here, a 17 MA RE beam forms after the TQ and undergoes vertical instability. During the upward vertical movement, the beam suffers an MHD instability, and most of the REs are lost along the stochastic field lines, which differs substantially from 2D scrape-off (see section 7 for more details on 3D impact modeling). Particle tracing has been used to evolve the initialized RE markers during the RE beam termination phase and to deposit their energy onto the upper limiter and first wall.

A model for the RE-structure interaction is then required to simulate the RE slowing down and evaluate their deposition in the structure. For this purpose, simpler (stopping-power) or complex and high-fidelity models (e.g. FLUKA) exist. FLUKA was used in [458] for studies of RE damage in EU-DEMO. Recent modeling of monoenergetic RE-PFC interaction with FLUKA is summarized in [315]: Since true RE beams are not mono-energetic (see section 5) and their energy distribution plays a key role in determining the heat deposition profile in the structure (see section 8), the code DREAM [41] has been used to evaluate the RE distribution function. Preliminary results [459] are now available for MC calculations of energy deposition. The recently developed work-flow of [364] can then be used to study eventual RE-induced damage of the EU-DEMO PFCs. Further details on modeling of the RE-PFC interaction are provided in section 8.

Besides the EU-DEMO, other fully superconducting tokamaks are being built or are planned to be built in Europe. These are the Divertor Tokamak Test (DTT, $I_p = 5.5$ MA, $R_0 = 2.19$ m and $a = 0.70$ m) in Italy and the Spherical Tokamak for Energy Production (STEP, $I_p = 20$ MA, $R_0 = 3.6$ m and $a = 2$ m)

in the United Kingdom. The CQ phase of DTT and the likelihood for RE generation and multiplication in early plasma current (up to 2 MA) plasmas were studied using the non-linear MHD code JOREK [460]. The results indicate that in this initial low-current scenario, the RE generation is negligible as long as the impurities injected by the DMS are limited.

Unmitigated RE generation in STEP was modeled using the code DREAM [461], with hot-tail generation found to be the dominant primary generation mechanism and avalanche multiplication of REs found to be extremely high. To mitigate potential RE beams, the STEP concept design already includes multiple SPI (with MGI as another option) systems dedicated to RE beam mitigation. This includes redundancy and assumes repetitive injections during the RE beam plateau to keep conditions prone to benign termination.

In North America. The SPARC tokamak is currently under construction by Commonwealth Fusion Systems (CFSs). High temperature superconducting (HTS) technology [462] enables SPARC's high $B_0 = 12.2\,\mathrm{T}$; high $I_\mathrm{p} = 8.7\,\mathrm{MA}$; and compact size with $R_0 = 1.85\,\mathrm{m}$ and $a = 0.57\,\mathrm{m}$ [463]. The planned highest-performing DT plasma, the 'primary reference discharge' (PRD), expects $T_e > 20\,\mathrm{keV}$ and $P_\mathrm{fus} > 100\,\mathrm{MW}$ [130]. For disruptions, the ITPA database scaling [464] predicts a fastest CQ time of ∼3.2 ms; more on SPARC disruptions, halo currents, thermal and EM loads, and mitigation systems can be found in [254].

RE seeds from the hot electron tail, tritium beta decay, and Compton scattering are expected in SPARC, as well as strong avalanching from the relatively high current. The first DREAM [41] simulations of RE generation [465] in a SPARC PRD disruption, mitigated with Ne MGI, indicated a final electron temperature <10 eV, RE plateau current ∼5.5 MA, and average RE energy ∼8 MeV. However, a sufficiently high deuterium MGI density ($n_\mathrm{D} \gtrsim 10^{22}\,\mathrm{m}^{-3}$) and moderate Ne MGI density ($n_\mathrm{Ne} \lesssim 10^{20}\,\mathrm{m}^{-3}$) could bring the RE current below 1 MA [466][22], and the novel REMC may prevent the beam altogether, depending on the re-formation of magnetic flux surfaces during the CQ and RE confinement therein [467]. However, it is important to note that both MGI and REMC are not machine protection systems for SPARC, which has been designed to be robust to plasma disruptions and REs; instead, they are part of the broader experimental mission to validate and optimize such systems for future tokamak power plants, with upgrades possible.

Yet REs may still cause some damage to the tungsten-based PFCs in SPARC. Since the threshold energy density for W damage is ∼3–5 $\mathrm{MJ\,m^{-2}}$ [76], RE beams with currents >2 MA would likely cause melting to PFCs for wetted areas <1 $\mathrm{m^2}$ [468]. We note that because SPARC discharges will be <10 s in duration and operate at low duty cycle, its PFCs are inertially cooled, i.e. having no cooling channels near the PFCs. This precludes any RE-induced loss-of-coolant accidents. The Heat flux Engineering Analysis Toolkit (HEAT) toolkit [469] has recently added REs to study their losses and impact on CAD PFCs. From realistic VDE simulations from M3D-C1, REs were found to 'scrape off' on PFCs during the vertical motion, and a RE-impact footprint with poloidal extent ∼0.5 m was estimated in HEAT, resulting in a total wetted area >1 $\mathrm{m^2}$, assuming toroidal symmetry [468]. Further HEAT development is ongoing, including RE diffusion and drifts, as well as the coupling of open-source heat transfer software. Planned diagnostics for SPARC early campaigns [470]—such as magnetics, visible and IR imaging and spectroscopy systems, neutron and HXR detectors—will provide insight into RE beam currents, energies, and impacts.

In addition to the total RE beam energy, individual electron energies and impact angles are important parameters defining resulting damage. An initial scoping study of energy deposition and the resulting thermal response was carried out by the Geant4-MEMENTO workflow [364]. A scan in individual RE energy and pitch angle, total RE beam energy, and impact duration was performed for a realistic SPARC VDE (same as above) and a realistic tile geometry, with a cross-section shown in figure 32. The curved tile geometry implies (i) steep impact angles and (ii) that even with a uniform RE source, the loading is nonuniform, with REs depositing more energy in the edge of the tile as clearly visible from figure 32. For the case shown (10 MeV, zero pitch angle REs), 100 kJ of total energy deposited over 1–10 ms leads to ∼1 mm-deep melting at the tile's edge, but negligible vaporization.

Current and future challenges

In Asia. In a power plant like CFETR, disruptions are expected to occur infrequently. This is based on the assumption that well-qualified plasma scenarios and operational procedures will be established and

[22] In SPARC, the *maximum* injection quantities into the vacuum vessel are ∼4 $\mathrm{kPa\,m^3}$ of D_2 and ∼0.8 $\mathrm{kPa\,m^3}$ of Ne per discharge.

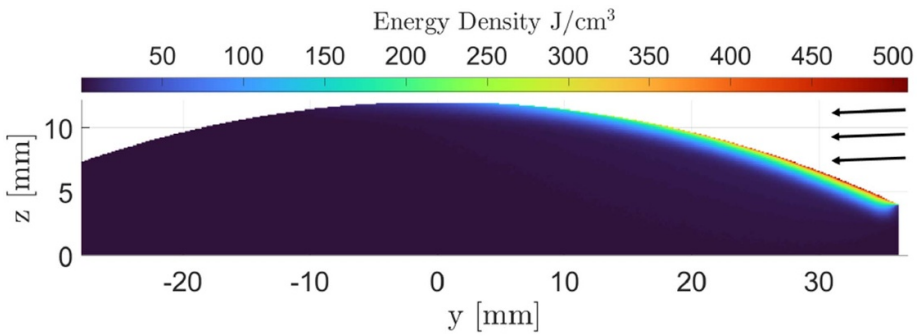

Figure 32. Monte Carlo simulations of RE deposited energy density (normalized to 1 kJ total energy) within a cross-sectional cut of a realistic SPARC plasma facing component. The incoming REs (10 MeV, zero pitch angle) are indicated by black arrows. Magnetic field inclination angle increases from 1° at the tile surface's topmost point to 25° at the edge, with $|B| = 13.6$ T. Calculations are performed with the work-flow of reference [364].

adhered to following experimental campaigns at ITER and other fusion facilities. Yet REs generated during plasma disruptions can cause substantial damage to the wall, not to mention the resulting EM forces. Thus, proper disruption detection, prevention, and mitigation methods are still needed.

Detection involves real-time monitoring of various plasma parameters to identify early signs of instability. Advanced diagnostics and sensors are expected to be used to detect changes in current, density, temperature, and magnetic fields. When a disruption is unavoidable, mitigation techniques are employed to minimize its impact. Shattered pellet injection (SPI), like in ITER, is being considered for CFETR. Other DMSs like MGI or EM particle injector are promising. Disruption detection, prevention and mitigation methods in CFETR have not been decided yet. Tokamaks like ITER will provide more insight about the disruption physics and test the reliability of these methods. Additionally, the current modeling is restricted to the thermal PFC response. The lack of understanding regarding tungsten damage by REs presents challenges in evaluating component damage and impact on plasma operation. More efforts should be directed toward conducting dedicated experiments to gain deeper insights into this phenomenon.

In Europe. The feasibility of a FPP of the tokamak type relies heavily on the solution of the problems caused by the interaction of the REs with the PFCs. It is not known at this point whether the combination of RE mitigation and proper design of sacrificial structures, along with an improved understanding of the functional dependence of the area interaction surface, can lead to acceptable heat load specifications. Disruption mitigation for the EU-DEMO tokamak has not been studied until now essentially because reliable RE avoidance or/and mitigation methods were not available. Some progress has been made in the last years in understanding the mechanisms of the RE benign termination. The method should be investigated further not only experimentally but particularly with numerical modeling tools. There are several phenomena involved in RE benign termination and they are mostly known, because they play a role in other plasma scenarios. However, their numerical implementations are not all contained in a single code. The development of a physics model with predictive capabilities is an ambitious but necessary step to assess the effects of RE-PFC interaction.

In North America. CFS is continuing to develop its electricity-producing ARC tokamak design, which is now planned to be sited in Virginia, USA [471]. From [472], ARC will have tokamak parameters $R_0 \sim 4$ m, $a \sim 1$ m, $B_0 \sim 11.5$ T, and $I_p \sim 10$ MA, producing $P_{fus} \sim 0.5$–1 GW. Due to its increased size, ARC CQ durations are expected to be >3 times longer than SPARC; while stored thermal and magnetic energies are also larger, the resulting disruption fluxes and stresses are—in some ways—balanced by the increased surface area. More details on ARC can be found in upcoming publications of the ARC Physics Basis [473].

REs will have similar generation mechanisms in ARC compared to SPARC, although one new challenge could be the increased level of activation, due to higher fusion power and neutron fluence, and its impact on Compton scattering. Simulations are underway to assess this. In addition, the several MA increase in plasma current from SPARC to ARC could lead to higher avalanching, even by a factor >100. PFCs will also be actively cooled in ARC; while the final design is not yet set, current design iterations are considering wall thicknesses of order ∼15 mm. It needs to be assessed whether REs could melt (or vaporize) a hole into a cooling channel. Furthermore, RE energy deposition into the coolant or into the blanket material, planned to be the liquid molten salt FLiBe, behind PFCs must be assessed. Secondary

particles, such as high energy gamma-rays from bremsstrahlung, may penetrate the blanket and shielding to deposit energy in the HTS coils. A low temperature superconducting (LTS) magnet was quenched before in the Tore-Supra/WEST tokamak after a beam impact [56]; a worst case scenario for SPARC, analyzed with GEANT4, estimated a manageable temperature rise in HTS with a wider operational space than LTS. However, this still must be evaluated for ARC.

Yet the mission of SPARC is to map learnings to ARC, influencing aspects of the design and operation, e.g. PFC geometry or sacrificial limiters. Model validation of SPARC REs will provide more accurate predictions for ARC REs: generation, evolution dynamics, mitigation strategies, PFC impacts and damage. Even sooner, upcoming experiments at an ∼MeV electron accelerator will provide empirical data for benchmarking with codes like MEMENTO and HEAT. While MGI is a baseline DMS for ARC [473], other options could be explored as SPARC upgrades to then install on ARC, e.g. SPI. Furthermore, the REMC physics experiment on SPARC will inform the need for an ARC REMC. However, we note that an important goal of any tokamak-based FPP is a stable, reproducible plasma discharge with ideally fewer disruptions and REs inherently. ARC's planned ability to replace the entire vacuum vessel also allows some flexibility in design iteration as well as its overall robustness to disruption loads and RE impacts [472].

Concluding remarks

Several complex and reliable physical models are required to evaluate the potential damage of REs interacting with PFCs. In spite of the level of detail reached by most of the numerical codes involved, large uncertainties affect the evaluation of the damage because the magnitude of the RE flux is unknown. Limiters and first wall tiles melted by RE beams exist, but much work remains to understand the phenomena responsible for the losses. Therefore, it is presently impossible to describe the plasma conditions leading to RE damages and to specify the largest RE flux expected in a given device. Well diagnosed experiments and dedicated simulations are mandatory in the near future to gather the needed missing information.

Data availability statement

The data cannot be made publicly available upon publication due to legal restrictions preventing unrestricted public distribution. The data that support the findings of this study are available upon reasonable request from the authors.

Acknowledgment

The guest editors (Svetlana Ratynskaia, Matthias Hoelzl, Eric Nardon) and the authors would like to express their gratitude to Alberto Loarte, Fransesco Maviglia, Carlos Paz-Soldan and Hartmut Zohm for their exceptional effort in refereeing this Roadmap article, and for generously sharing their insight into the topic. The identities of the reviewers are disclosed with the explicit consent of both the reviewers and the journal editors.

Some of the work has been performed within the framework of the EUROfusion Consortium, funded by the European Union via the Euratom Research and Training Programme (Grant Agreement No 101052200 - EUROfusion). The views and opinions expressed are however those of the authors only and do not necessarily reflect those of the European Union, the European Commission or the ITER Organization. The European Union, European Commission or ITER Organization cannot be held responsible for them.

R A T acknowledges support by CFS. O F acknowledges support for COMPASS related work by CR-MEYS Projects LM2023045 and 9D22001. J R M S acknowledges support of work related to the Universidad Carlos III de Madrid in section 6 by Ministerio de Ciencia e Innovacion (Spain), Project PID2022-137869OB-I00. For work contributed by E M H, this material is based upon work supported by the U.S. Department of Energy, Office of Science, Office of Fusion Energy Sciences, using the DIII-D National Fusion Facility, a DOE Office of Science user facility, under Awards DE-FC02-04ER54698 and DE-FG02-07ER54917. B B and D d C N acknowledge support from the U.S. Department of Energy under Contract Nos. DE-FG02-04ER-54742 and DESC001683.

S R, M H and E N thank Dr F Leuterer (Max Planck Institute for Plasma Physics, Garching, Germany) for bringing to their attention the evidence of RE-induced damage to antennas in 1983 ASDEX experiments.

Dr M Diez and Dr Y Corre (CEA, Saint-Paul-lez-Durance, France) are gratefully acknowledged for providing damage evidence from WEST presented in sections 2 and 3.

Disclaimer

Appendix A. RE impact diagnostics

Tokamak	IR thermogr.	Calorimetry	HXR/SXR photo-neutrons	Direct	Post-impact/fast cameras
JET	Multiple mid and near IR cameras [137, 474]	Thermocouples (TCs)	3 spectrometers [150], 19 LOS profile monitor [154]		Fast cameras [475], limiter impact analysis [88]
ASDEX Upgrade	Multiple came-ras, real-time [476]	TCs	REGARDS spectrometer [147]		
TCV	Multiple IR cameras, toroidally spaced [96]	TCs [96]	LaBrDORE spectrometer [149]	3 channel Cherenkov detector [164]	
WEST / TORE-SUPRA	IR cameras [477]	TCs, calorimeter planned	HXR Camera [156], SIGARS spectrometer from 2026		
DIII-D	Multiple IR cameras [132, 140, 141]	DiMES [146]	Gamma ray imager [155]	Graphite limiter for pitch angle measurements [4]	Confocal microscopy and other methods [4, 40]
COMPASS	Fast observations of LFS/HFS limi-ter [133]	Dedicated calorimetry head [102]	Uncollimated scintillators [151], SXR pixel detectors [160]	3 channel Cherenkov detector [163]	Microscopy [102]
TEXTOR	Diode with scanning mirrors [478]	Dedicated RE calorimeter [113]	HXR monitors [479]	Scintillator [111]	Metallography and thermogravitmetry [112]
FTU	Diode with scanning mirrors	TCs	Gamma and neutron camera [480, 481]	Cherenkov detector [415]	Fast cameras, SEM, other methods [119, 395]
Other machines	For synch. rad.: J-TEXT [136], EAST [138], HT-7 [482]		ADITYA [483], J-TEXT, Golem [151]	Golem: Si detector [168], scintillator [167]	

Appendix B. List of acronyms

Acronym	Explanation
0D-6D	Zero- to six-dimensional
ALE	Arbitrary Lagrangian Eulerian
ATJ	Private company, acronym unknown
AUG	ASDEX Upgrade
CFC	Carbon fibre composites
CFETR	China Fusion Engineering Test Reactor
CFS	Commonwealth Fusion Systems
CSDA	Continuous-slowing down approximation
DMS	Disruption mitigation system
DMV	Disruption mitigation valve
EDS	Electron dispersive x-ray spectroscopy
ELM	Edge localized mode
EM	Electromagnetic

(Continued.)

(Continued.)

Acronym	Explanation
FEM	Finite element method
FPP	Fusion power plant
FWP	First wall panel
GC	Gyro-center
HFS	High field side
HXR	Hard x-ray
HTS	High temperature superconductor
ILW	so-called ITER like wall (JET)
IR	Infrared
IVIS	In-vessel visual inspection
IVVS	In-Vessel Viewing System (in ITER)
IWGL	Inner wall guard limiter
JET	Joint European Torus
LFS	Low field side
LTS	Low temperature superconductor
MC	Monte Carlo
MGI	Massive gas injection
MHD	Magneto-hydrodynamics
MIT	Massachusetts Institute of Technology
MMI	Massive material injection
PD	Peridynamic theory
PFC	Plasma facing component
PFM	Phase field method
PRD	Primary reference discharge (SPARC)
SPH	Smoothed particle hydrodynamics
RE	Runaway electron
RMP	Resonant magnetic perturbation
SPI	Shattered pellet injection
SRO	Start of research operation (in ITER)
SXR	Soft x-ray
TFW	Temporary first wall (in ITER)
TM	Tearing mode
UDP	Upper dump plate
VDE	Vertical displacement event
XPS	x-ray photoelectron spectroscopy

ORCID iDs

S Ratynskaia 0000-0002-6712-3625
M Hoelzl 0000-0001-7921-9176
E Nardon 0000-0003-0427-2292
P Aleynikov 0009-0002-3037-3679
F J Artola 0000-0001-7962-1093
V Bandaru 0000-0003-4096-1407
M Beidler 0000-0002-7385-3886
B Breizman 0000-0002-7908-6497
D del-Castillo-Negrete 0000-0001-7183-801X
M De Angeli 0000-0002-7779-7842
V Dimitriou 0000-0003-4823-0350
R Ding 0000-0003-2880-9736
J Eriksson 0000-0002-0892-3358
O Ficker 0000-0001-6418-9517
R S Granetz 0000-0002-6560-1881
E Hollmann 0000-0002-6267-6589
M Hoppe 0000-0003-3994-8977
M Houry 0009-0002-5349-6743
I Jepu 0000-0001-8567-3228
H R Koslowski 0000-0002-1571-6269
C Liu 0000-0002-6747-955X

J R Martin-Solis 0000-0003-0458-4405
Y Peneliau 0000-0002-4282-9621
R A Pitts 0000-0001-9455-2698
G I Pokol 0000-0003-1473-0736
C Reux 0000-0002-5327-4326
U Sheikh 0000-0001-6207-2489
S A Silburn 0000-0002-3111-5113
T Tang 0000-0002-2898-7658
R A Tinguely 0000-0002-3711-1834
P Tolias 0000-0001-9632-8104
E Tomesova 0000-0002-0381-9244
R Villari 0000-0001-7972-1676

References

[1] Federici G *et al* 2001 *Nucl. Fusion* **41** 1967–2137
[2] Bandaru V, Hoelzl M, Bergström H, Artola F J, Särkimäki K and Lehnen M 2024 *Nucl. Fusion* **64** 076053
[3] Bergström H, Särkimäki K, Bandaru V, Skyllas M M and Hoelzl M 2024 *Plasma Phys. Control. Fusion* **66** 095001
[4] Ratynskaia S *et al* 2025 *Nucl. Fusion* **65** 024002
[5] The Indirect Drive ICF Collaboration 2024 *Phys. Rev. Lett.* **132** 065102
[6] Maslov M *et al* 2023 *Nucl. Fusion* **63** 112002
[7] Dinklage A *et al* 2025 *Plasma Phys. Control. Fusion* **67** 063701
[8] Pitts R *et al* 2017 *Nucl. Mater. Energy* **12** 60–74
[9] Pitts R *et al* 2019 *Nucl. Mater. Energy* **20** 100696
[10] Pitts R *et al* 2025 *Nucl. Mater. Energy* **42** 101854
[11] Krieger K *et al* 2018 *Nucl. Fusion* **58** 026024
[12] Ratynskaia S, Vignitchouk L and Tolias P 2022 *Plasma Phys. Control. Fusion* **64** 044004
[13] Ratynskaia S, Bortolon A and Krasheninnikov S 2022 *Rev. Mod. Plasma Phys.* **6** 20
[14] Beckers J *et al* 2023 *Phys. Plasmas* **30** 120601
[15] Krieger K *et al* 2025 *Nucl. Fusion* **65** 043001
[16] Berger M J 1992 ESTAR, PSTAR and ASTAR: computer programs for calculating stopping-power and range tables for electrons, protons and helium ions *Technical Report NISTIR* 4999 (National Institute of Standards and Technology)
[17] Coenen J *et al* 2013 *J. Nucl. Mater.* **438** S27–S33
[18] Coenen J W *et al* 2017 *Phys. Scr.* **2017** 014013
[19] Krieger K *et al* 2017 *Phys. Scr.* **2017** 014030
[20] Jepu I *et al* 2019 *Nucl. Fusion* **59** 086009
[21] Corre Y *et al* 2021 *Phys. Scr.* **96** 124057
[22] Corre Y *et al* 2023 *Nucl. Mater. Energy* **37** 101546
[23] Ratynskaia S, Thorén E, Tolias P, Pitts R A, Krieger K, Vignitchouk L and Iglesias D 2020 *Nucl. Fusion* **60** 104001
[24] Ratynskaia S, Thorén E, Tolias P, Pitts R A and Krieger K 2021 *Phys. Scr.* **96** 124009
[25] Thorén E, Ratynskaia S, Tolias P, Pitts R A, Krieger K, Komm M and Balden M 2018 *Nucl. Mater. Energy* **17** 194–9
[26] Thorén E, Ratynskaia S, Tolias P and Pitts R A 2021 *Plasma Phys. Control. Fusion* **63** 035021
[27] Ratynskaia S *et al* 2022 *Nucl. Mater. Energy* **33** 101303
[28] Ratynskaia S *et al* 2024 *Nucl. Fusion* **64** 036012
[29] Paschalidis K, Ratynskaia S, Lucco Castello F and Tolias P 2023 *Nucl. Mater. Energy* **37** 101545
[30] Paschalidis K, Lucco Castello F, Ratynskaia S, Tolias P and Brandt L 2024 *Fusion Eng. Des.* **206** 114603
[31] Coburn J *et al* 2020 *Phys. Scr.* **2020** 014076
[32] Coburn J *et al* 2021 *Nucl. Mater. Energy* **28** 101016
[33] Coburn J *et al* 2021 *Nucl. Fusion* **62** 016001
[34] Paschalidis K, Ratynskaia S, Tolias P and Pitts R 2024 *Nucl. Fusion* **64** 126022
[35] Lehnen M *et al* 2015 *J. Nucl. Mater.* **463** 39–48
[36] Boozer A H 2015 *Phys. Plasmas* **22** 582
[37] Boozer A H 2017 *Nucl. Fusion* **57** 056018
[38] Breizman B N, Aleynikov P, Hollmann E M and Lehnen M 2019 *Nucl. Fusion* **59** 083001
[39] Loarte A *et al* 2025 *Plasma Phys. Control. Fusion* **67** 065023
[40] Hollmann E M *et al* 2025 *Plasma Phys. Control. Fusion* **67** 035020
[41] Hoppe M, Embreus O and Fülöp T 2021 *Comput. Phys. Commun.* **268** 108098
[42] Martin-Solis J R, Loarte A and Lehnen M 2017 *Nucl. Fusion* **57** 066025
[43] Liu C, Hirvijoki E, Fu G-Y, Brennan D P, Bhattacharjee A and Paz-Soldan C 2018 *Phys. Rev. Lett.* **120** 265001
[44] Bandaru V, Hoelzl M, Artola F J, Papp G and Huijsmans G T A 2019 *Phys. Rev. E* **99** 063317
[45] Breizman B and Aleynikov P 2017 *Nucl. Fusion* **57** 125002
[46] Vallhagen O *et al* 2024 *Nucl. Fusion* **64** 086033
[47] Equipe TFR 1975 *Control. Fusion Plasma Phys.* **1** 2
[48] Barber W C and George W D 1959 *Phys. Rev.* **116** 1551–9
[49] Strachan J, Meservey E B, Stodiek W, Naumann R A and Girshick F 1977 *Nucl. Fusion* **17** 140
[50] Maddaluno G and Vannucci A 1987 *J. Nucl. Mater.* **145-147** 697–9
[51] Jarvis O N, Sadler G and Thompson J L 1988 *Nucl. Fusion* **28** 1981
[52] Yoshino R, Tokuda S and Kawano Y 1999 *Nucl. Fusion* **39** 151
[53] Pinkau K *et al* 1983 Annual report 1983 *Technical Report* (Max-Planck-Institut fur Plasmaphysik Garching bei Munchen) (available at: https://pure.mpg.de/rest/items/item_2473350_1/component/file_2473349/content)

[54] Leuterer F *et al* 1985 *Plasma Phys. Control. Fusion* **27** 1399
[55] Nygren R *et al* 1997 *J. Nucl. Mater.* **241–243** 522–7
[56] Torre A, Ciazynski D, Girard S, Lacroix B, Nicollet S, Reux C and Tena M 2019 *IEEE Trans. Appl. Supercond.* **29** 1–5
[57] Chen L, Pitts R and Lehnen M 2021 *5th Asia-Pacific Conf. on Plasma Physics* p MF2-II4
[58] Reux C *et al* 2021 *Phys. Rev. Lett.* **126** 175001
[59] Paz-Soldan C *et al* 2021 *Nucl. Fusion* **61** 116058
[60] Wesson J *et al* 1989 *Nucl. Fusion* **29** 641
[61] Gill R D 1993 *Nucl. Fusion* **33** 1613–25
[62] Keilhacker M and Watkins M L JET Team 1999 *J. Nucl. Mater.* **266-269** 1–13
[63] Litaudon X *et al* 2017 *Nucl. Fusion* **57** 102001
[64] Loarte A *et al* 2007 *Nucl. Fusion* **47** S203
[65] Federici G *et al* 2016 *Fusion Eng. Des.* **109–111** 1464–74
[66] Coad J P, Rubel M and Wu C H 1997 *J. Nucl. Mater.* **241-243** 408–13
[67] Matthews G F *et al* 2007 *Phys. Scr.* **T128** 137–43
[68] Matthews G F *et al* 2011 *Phys. Scr.* **2011** 4001
[69] Matthews G F (JET EFDA Contributors and ASDEX-Upgrade Team) 2013 *J. Nucl. Mater.* **438** S2–S10
[70] Gill R D, Alper B, Baar M D, Hender T C, Johnson M F and Riccardo V (Workprogramme contributors to the E F D A-J E T) 2002 *Nucl. Fusion* **42** 1039–44
[71] Helander P, Eriksson L-G and Andersson F 2002 *Plasma Phys. Control. Fusion* **44** B247–62
[72] Riccardo V *et al* 2010 *Plasma Phys. Control. Fusion* **52** 124018
[73] Plyusnin V V *et al* 2012 *IAEA FEC* p EX/8-05
[74] Gill R D, Alper B, Edwards A W, Ingesson L C, Johnson M F and Ward D J 2000 *Nucl. Fusion* **40** 163
[75] Hender T *et al* 2007 *Nucl. Fusion* **47** S128
[76] Lehnen M *et al* 2009 *J. Nucl. Mater.* **390–391** 740–6
[77] Arnoux G *et al* 2011 *J. Nucl. Mater.* **415** S817–20
[78] Plyusnin V *et al* 2006 *Nucl. Fusion* **46** 277
[79] Bazylev B, Arnoux G, Fundamenski W, Igitkhanov Y and Lehnen M 2011 *J. Nucl. Mater.* **415** S841–4
[80] Harris G R 1990 *JET Joint Undertaking Report* JET-R(90)07
[81] Dietz K J The JET Team 1990 *Plasma Phys. Control. Fusion* **32** 837–52
[82] Reux C *et al* 2015 *Nucl. Fusion* **55** 093013
[83] de Vries P C *et al* 2012 *Plasma Phys. Control. Fusion* **54** 124032
[84] Lehnen M *et al* 2013 *Nucl. Fusion* **53** 093007
[85] Papp G *et al* 2013 *Nucl. Fusion* **53** 123017
[86] Reux C *et al* 2015 *J. Nucl. Mater.* **463** 143–9
[87] Linke J, Du J, Loewenhoff T, Pintsuk G, Spilker B, Steudel I and Wirtz M 2019 *Matter Radiat. Extremes* **4** 056201
[88] Jepu I *et al* 2024 *Nucl. Fusion* **64** 106047
[89] Moon S, Petersson P, Rubel M, Fortuna-Zalesna E, Widdowson A, Jachmich S, Litnovsky A and Alves E 2019 *Nucl. Mater. Energy* **19** 59–66
[90] Rubel M *et al* 2018 *Fusion Eng. Des.* **136** 579–86
[91] Fortuna-Zaleśna E, Grzonka J, Moon S, Rubel M, Petersson P and Widdowson A 2017 *Phys. Scr.* **T170** 014038
[92] Brezinsek S *et al* 2015 *Nucl. Fusion* **55** 063021
[93] Hollmann E *et al* 2011 *Nucl. Fusion* **53** 103026
[94] Hollmann E M *et al* 2020 *Phys. Plasmas* **27** 3299
[95] Decker J *et al* 2022 *Nucl. Fusion* **62** 076038
[96] Sheikh U *et al* 2024 *Plasma Phys. Control. Fusion* **66** 035003
[97] Decker J and Peysson Y 2004 Dke: a fast numerical solver for the 3d drift kinetic equation *Technical Report No.* EUR-CEA-FC-1736
[98] Sheikh U A *et al* 2023 Theory and simulation of disruptions workshop
[99] Decker J, Hirvijoki E, Embreus O, Peysson Y, Stahl A, Pusztai I and Fülöp T 2016 *Plasma Phys. Control. Fusion* **58** 025016
[100] Sheikh U A *et al* 2020 *IAEA Technical Meeting on Plasma Disruptions and Their Mitigation*
[101] Hron M *et al* 2022 *Nucl. Fusion* **62** 042021
[102] Caloud J *et al* 2024 *Rev. Sci. Instrum.* **95** 113512
[103] Mlynar J *et al* 2018 *Plasma Phys. Control. Fusion* **61** 014010
[104] Horacek J *et al* 2015 *J. Nucl. Mater.* **463** 385–8
[105] Kovarik K, Duran I, Stockel J, Seidl J, Adamek J, Spolaore M, Vianello N, Hacek P, Hron M and Panek R 2017 *Rev. Sci. Instrum.* **88** 035106
[106] Bucalossi J *et al* 2022 *Nucl. Fusion* **62** 042007
[107] Reux C, Diez M, Gerardin J and Corre Y 2024 *EPS 2024 Satellite Meeting on Runaway Electron Impacts* (available at: https://epsplasma2024.com/satellite-meeting/)
[108] Neubauer O, Czymek G, Giesen B, Hüttemann P W, Sauer M, Schalt W and Schruff J 2005 *Fusion Sci. Technol.* **47** 76–86
[109] Kohlhass K *et al* 1990 *Fusion Eng. Des.* **13** 261
[110] Hoven H, Koizlik K, Linke J, Nickel H, Wallura E and Kohlhaas W 1989 *J. Nucl. Mater.* **162** 970
[111] Kudyakov T, Finken K H, Jakubowski M, Lehnen M, Xu Y and Willi O 2008 *Rev. Sci. Instrum.* **79** 10F126
[112] Forster M, Finken K H, Lehnen M, Linke J, Schweer B, Thomser C, Willi O and Xu Y 2011 *Nucl. Fusion* **51** 043003
[113] Forster M, Finken K H, Lehnen M, Willi O and Xu Y 2012 *Phys. Plasmas* **19** 052506
[114] Izzo V *et al* 2011 *Nucl. Fusion* **51** 063032
[115] Tinguely R A, Granetz R, Hoppe M and Embréus O 2018 *Nucl. Fusion* **58** 076019
[116] Granetz R S *et al* 2014 *Phys. Plasmas* **21** 072506
[117] Pizzuto A *et al* 2004 *Fusion Sci. Technol.* **45** 422–36
[118] Esposito B *et al* 2016 *Plasma Phys. Control. Fusion* **59** 014044
[119] De Angeli M *et al* 2022 *Nucl. Fusion* **63** 014001
[120] Maddaluno G and Esposito B 1999 *J. Nucl. Mater.* **266-269** 593–7
[121] Vertkov A, Lyublinski I, Zharkov M, Mazzitelli G, Apicella M L and Iafrati M 2017 *Fusion Eng. Des.* **117** 130–4

[122] Reux C *et al* 2021 *Virtual Event 28th IAEA Fusion Energy Conf.* pp 286–1055
[123] Diez M *et al* 2021 *Nucl. Fusion* **61** 106011
[124] Nicollet S, Torre A, Lacroix B, Louzguiti A, Gorit Q and Team W 2022 *Cryogenics* **125** 103493
[125] Houry M, Malard P, Pellissier F-P and Peneliau Y 2024 *Proc. of the 50th EPS Conf. on Plasma Physics*
[126] Guo Z *et al* 2024 *Nucl. Fusion* **64** 076026
[127] Xuan C, Zhu D, Wang Y, Gao B, Fu W, Guo Z, Ding R, Wang B, Zi P and Chen J 2025 *Nucl. Fusion* **65** 046027
[128] Pautasso G *et al* 2016 *Plasma Phys. Control. Fusion* **59** 014046
[129] Heinrich P *et al* 2024 *Nucl. Fusion* **64** 076044
[130] Rodriguez-Fernandez P *et al* 2022 *Nucl. Fusion* **62** 042003
[131] Ficker O *et al* 2023 *29th IAEA Fusion Energy Conf. (FEC 2023)*
[132] Hill D N, Ellis R, Ferguson W, Perkins D E, Petrie T and Baxi C 1988 *Rev. Sci. Instrum.* **59** 1878–80
[133] Vondracek P, Gauthier E, Ficker O, Hron M, Imrisek M and Panek R 2017 *Fusion Eng. Des.* **123** 764–7
[134] Dunn M J, Morgan T W, Genuit J W, Loewenhoff T, Thornton A J and Gibson K J 2020 *Nucl. Mater. Energy* **25** 100832
[135] Finken K, Watkins J G, Rusbüldt D, Corbett W J, Dippel K H, Goebel D M and Moyer R A 1990 *Nucl. Fusion* **30** 859
[136] Tong R H, Chen Z Y, Zhang M, Huang D W, Yan W and Zhuang G 2016 *Rev. Sci. Instrum.* **87** 11E113
[137] Reux C *et al* 2022 *Nucl. Fusion* **64** 034002
[138] Zhang Y, Zhou R, Hu L, Lin S and Yang X 2025 *Fusion Eng. Des.* **211** 114738
[139] Tinguely R A, Rosenthal A M, Silva Sa M, Jean M and Abramovic I 2024 *Rev. Sci. Instrum.* **95** 113503
[140] Beidler M, del-Castillo-Negrete D, Shiraki D, Baylor L R, Hollmann E M and Lasnier C J 2024 *Nucl. Fusion* **64** 076038
[141] Hollmann E M, Commaux N, Eidietis N W, Lasnier C J, Rudakov D L, Shiraki D, Cooper C, Martin-Solis J R, Parks P B and Paz-Soldan C 2017 *Phys. Plasmas* **24** 062505
[142] Delchambre E, Counsell G and Kirk A 2009 *Plasma Phys. Control. Fusion* **51** 055012
[143] Aumeunier M-H, Kočan M, Reichle R and Gauthier E 2017 *Nucl. Mater. Energy* **12** 1265–9
[144] McLean A G, Ahn J-W, Maingi R, Gray T K and Roquemore A L 2012 *Rev. Sci. Instrum.* **83** 053706
[145] Ushiki T, Imazawa R, Murakami H, Shimizu K, Sugie T and Hatae T 2022 *Rev. Sci. Instrum.* **93** 084905
[146] Wong C P C *et al* 2007 *J. Nucl. Mater.* **363–365** 276–81
[147] Dal Molin A *et al* 2023 *Meas. Sci. Technol.* **34** 085501
[148] Simons L *et al* 2023 *5th European Conf. on Plasma Diagnostics*
[149] Simons L, Cerovsky J, Decker J, Duval B P, Ficker O, Hoppe M and Sheikh U 2025 *Rev. Sci. Instrum.* **96** 093501
[150] Tardocchi M *et al* 2008 *Rev. Sci. Instrum.* **79** 10E524
[151] Cerovsky J, Ficker O, Svoboda V, Macusova E, Mlynar J, Caloud J, Weinzettl V and Hron M 2022 *J. Instrum.* **17** C01033
[152] Dal Molin A *et al* 2021 *Rev. Sci. Instrum.* **92** 043517
[153] Ma T K, Chen Z Y, Huang D W, Tong R H, Yan W, Wang S Y, Dai A J and Wang X L 2017 *Nucl. Instrum. Methods Phys. Res. A* **856** 81–85
[154] Rigamonti D *et al* 2018 *Rev. Sci. Instrum.* **89** 10I116
[155] Pace D C, Cooper C M, Taussig D, Eidietis N W, Hollmann E M, Riso V, Van Zeeland M A and Watkins M 2016 *Rev. Sci. Instrum.* **87** 043507
[156] Wongrach K, Mazon D, Morales J, Fleury L, Picha R and Promping J 2021 *AIP Adv.* **11** 085313
[157] Grover O, Kocman J, Odstrcil M, Odstrcil T, Matusu M, Stöckel J, Svoboda V, Vondrasek G and Zara J 2016 *Fusion Eng. Des.* **112** 1038–44
[158] Poikela T *et al* 2014 *J. Instrum.* **9** C05013
[159] Svihra P *et al* 2019 *Fusion Eng. Des.* **146** 316–9
[160] Kulkov S *et al* 2022 *J. Instrum.* **17** 02030
[161] Kulkov S 2025 Semiconductor pixel detectors for nuclear physics and quantum astrometry *PhD Thesis* Czech Technical University Prague
[162] Zebrowski J *et al* 2018 *J. Phys.: Conf. Ser.* **959** 012002
[163] Rabinski M *et al* 2017 *J. Instrum.* **12** C10014
[164] Kwiatkowski R *et al* 2021 *Eur. Phys. J. Plus* **136** 1070
[165] Plyusnin V V *et al* 2008 *Rev. Sci. Instrum.* **79** 10F505
[166] Jakubowski L *et al* 2010 *Rev. Sci. Instrum.* **81** 013504
[167] Dhyani P, Svoboda V, Istokskaia V, Mlynář J, Čeřovský J, Ficker O and Linhart V 2019 *J. Instrum.* **14** C09029
[168] Novotny L *et al* 2020 *J. Instrum.* **15** C07015–07015
[169] Knoepfel H and Spong D 1979 *Nucl. Fusion* **19** 785–829
[170] Bakhtiari M, Kramer G J, Takechi M, Tamai H, Miura Y, Kusama Y and Kamada Y 2005 *Phys. Rev. Lett.* **94** 215003
[171] Fernández-Gómez I, Martín-Solís J R and Sánchez R 2007 *Phys. Plasmas* **14** 6219
[172] Embréus O, Stahl A and Fülöp T 2016 *New J. Phys.* **18** 093023
[173] Andersson F, Helander P and Eriksson L 2001 *Phys. Plasmas* **8** 5221–9
[174] Beliaev S T and Budker G I 1956 *Sov. Phys. Dokl.* **1** 218
[175] Braams B J and Karney C F F 1987 *Phys. Rev. Lett.* **59** 1817–20
[176] Pike O J and Rose S J 2014 *Phys. Rev. E* **89** 053107
[177] Zhogolev V and Konovalov S 2014 *Prob. Atom. Sci. Technol.* **37** 71–88
[178] Hesslow L, Embréus O, Stahl A, DuBois T,, Papp G, Newton S, and Fülöp T 2017 *Phys. Rev. Lett.* **118** 255001
[179] Hesslow L, Embréus O, Hoppe M, DuBois T, Papp G, Rahm M and Fülöp T 2018 *J. Plasma Phys.* **84** 905840605
[180] Sokolov Y A 1979 *JETP Lett.* **29** 244
[181] Rosenbluth M N and Putvinski S V 1997 *Nucl. Fusion* **37** 1355
[182] Chiu S C, Rosenbluth M N, Harvey R W and Chan V S 1998 *Nucl. Fusion* **38** 1711
[183] Aleynikov P *et al* 2014 *Int. Atomic Energy Agency 25th Fusion Energy Conf.* pp 13–18
[184] Embréus O, Stahl A and Fülöp T 2018 *J. Plasma Phys.* **84** 905840102
[185] Parail V and Pogutse O 1978 *Nucl. Fusion* **18** 303–14
[186] Pokol G, Fülöp T and Lisak M 2008 *Plasma Phys. Control. Fusion* **50** 045003
[187] Aleynikov P and Breizman B 2015 *Nucl. Fusion* **55** 043014
[188] Dreicer H 1960 *Phys. Rev.* **117** 329
[189] Connor J and Hastie R 1975 *Nucl. Fusion* **15** 415

[190] Hesslow L, Unnerfelt L, Vallhagen O, Embreus O, Hoppe M, Papp G and Fülöp T 2019 *J. Plasma Phys.* **85** 475850601
[191] Putvinski S, Barabaschi P, Fujisawa N, Putvinskaya N, Rosenbluth M N and Wesley J 1997 *Plasma Phys. Control. Fusion* **39** B157
[192] Hesslow L, Embréus O, Vallhagen O and Fülöp T 2019 *Nucl. Fusion* **59** 084004
[193] Smith H *et al* 2006 *Phys. Plasmas* **13** 8110
[194] Fehér T, Smith H M, Fülöp T and Gál K 2011 *Plasma Phys. Control. Fusion* **53** 035014
[195] Olasz S, Embreus O, Hoppe M, Aradi M, Por D, Jonsson T, Yadikin D and Pokol G I (EU-IM Team) 2021 *Nucl. Fusion* **61** 066010
[196] Landreman M, Stahl A and Fülöp T 2014 *Comput. Phys. Commun.* **185** 847–55
[197] Stahl A, Embréus O, Papp G, Landreman M and Fülöp T 2016 *Nucl. Fusion* **56** 112009
[198] Harvey R W and McCoy M G 1992 *Proc. IAEA TCM on Advances in Sim. and Modeling of Thermonuclear Plasmas* (Montreal) pp 489–526
[199] Guo Z, Mcdevitt C and Tang X 2019 *Phys. Plasmas* **26** 874
[200] Stahl A, Landreman M, Embréus O and Fülöp T 2017 *Comput. Phys. Commun.* **212** 269–79
[201] McDevitt C J, Guo Z and Tang X 2019 *Plasma Phys. Control. Fusion* **61** 054008
[202] Aleynikov P and Breizman B N 2017 *Nucl. Fusion* **57** 046009
[203] Daniel D, Taitano W T and Chacón L 2020 *Comput. Phys. Commun.* **254** 107361
[204] Hirvijoki E, Asunta O, Koskela T, Kurki-Suonio T, Miettunen J, Sipilä S, Snicker A and Äkäslompolo S 2014 *Comput. Phys. Commun.* **185** 1310–21
[205] Hoelzl M *et al* 2021 *Nucl. Fusion* **61** 065001
[206] Bergström H, Liu S-J, Bandaru V and Hoelzl M 2025 *Plasma Phys. Control. Fusion* **67** 035004
[207] Carbajal L, del-Castillo-Negrete D, Spong D, Seal S and Baylor L 2017 *Phys. Plasmas* **24** 81209
[208] Bandaru V, Hoelzl M, Artola F J, Vallhagen O and Lehnen M 2024 *Phys. Plasmas* **31** 082503
[209] Liu C, Zhao C, Jardin S C, Ferraro N M, Paz-Soldan C, Liu Y and Lyons B C 2021 *Plasma Phys. Control. Fusion* **63** 125031
[210] Sainterme A P and Sovinec C R 2024 *Phys. Plasmas* **31** 010701
[211] Matsuyama A, Aiba N and Yagi M 2017 *Nucl. Fusion* **57** 066038
[212] de Vries P and Gribov Y 2019 *Nucl. Fusion* **59** 096043
[213] de Vries P *et al* 2023 *Nucl. Fusion* **63** 086016
[214] Martín-Solís J R, Sánchez R and Esposito B 2010 *Phys. Rev. Lett.* **105** 185002
[215] Breizman B N 2014 *Nucl. Fusion* **54** 072002
[216] Putvinski S *et al* 1997 *J. Nucl. Mater.* **241–243** 316–21
[217] Linder O *et al* 2021 *J. Plasma Phys.* **87** 905870301
[218] Smith H M and Verwichte E 2008 *Phys. Plasmas* **15** 692
[219] Hollmann E *et al* 2019 *Nucl. Fusion* **59** 106014
[220] Kim H, Mineev A, Ricci D, Lee J-W and Na Y-S 2020 *Nucl. Fusion* **60** 126049
[221] Hoppe M, Ekmark I, Berger E and Fülöp T 2022 *J. Plasma Phys.* **88** 905880317
[222] Hollmann E *et al* 2023 *Nucl. Fusion* **63** 036011
[223] Beidler M T, del-Castillo-Negrete D, Baylor L R, Shiraki D and Spong D A 2020 *Phys. Plasmas* **27** 112507
[224] Aleynikov P and Breizman B N 2015 *Phys. Rev. Lett.* **114** 155001
[225] Hesslow L, Embréus O, Wilkie G J, Papp G and Fülöp T 2018 *Plasma Phys. Control. Fusion* **60** 074010
[226] Hoppe M *et al* 2021 *J. Plasma Phys.* **87** 855870102
[227] McDevitt C J, Tang X-Z, Fontes C J, Sharma P and Chung H-K 2023 *Nucl. Fusion* **63** 024001
[228] Garland N A *et al* 2020 *Phys. Plasmas* **27** 3638
[229] Garland N A, Chung H-K, Zammit M C, McDevitt C J, Colgan J, Fontes C J and Tang X-Z 2022 *Phys. Plasmas* **29** 71996
[230] Hoppe M *et al* 2025 *Plasma Phys. Control. Fusion* **67** 045015
[231] Guo Z, McDevitt C J and Tang X 2018 *Phys. Plasmas* **25** 9381
[232] Martín-Solís J, Esposito B, Sánchez R and Granucci G 2004 *Nucl. Fusion* **44** 974–81
[233] Fülöp T, Pokol G, Helander P and Lisak M 2006 *Phys. Plasmas* **13** 062506
[234] Pokol G, Kómár A, Budai A, Stahl A and Fülöp T 2014 *Phys. Plasmas* **21** 102503
[235] Decker J *et al* 2024 *Nucl. Fusion* **64** 106027
[236] Reinke M, Scott S, Granetz R, Hughes J W, Baek S G, Shiraiwa S, Tinguely R A and Wukitch S 2019 *Nucl. Fusion* **59** 066003
[237] Breizman B 2015 Runaway electrons (whitepaper) *Technical Report* (USBPO group)
[238] Fülöp T, Smith H M and Pokol G 2009 *Phys. Plasmas* **16** 2980
[239] Spong D *et al* 2018 *Phys. Rev. Lett.* **120** 155002
[240] Heidbrink W W *et al* 2019 *Plasma Phys. Control. Fusion* **61** 014007
[241] Bin W, Castaldo C, Napoli F, Buratti P, Cardinali A, Selce A and Tudisco O 2022 *Phys. Rev. Lett.* **129** 045002
[242] Breizman B N and Kiramov D I 2023 *Phys. Plasmas* **30** 022301
[243] Breizman B N and Kiramov D I 2023 *Phys. Plasmas* **30** 082105
[244] Tamai H *et al* 2002 *Nucl. Fusion* **42** 290
[245] Lukash V and Khayrutdinov R 2016 Final report IO/15/CT/4300001189 *Technical Report* (ITER)
[246] Martin-Solis J R, Mier J A, Lehnen M and Loarte A 2022 *Nucl. Fusion* **62** 076013
[247] Wang C, Nardon E, Artola F J, Bandaru V and Hoelzl M 2025 *Nucl. Fusion* **65** 016012
[248] Bandaru V, Hoelzl M, Artola F J and Lehnen M 2025 *J. Plasma Phys.* **91** E27
[249] Vallhagen O, Hanebring L, Fülöp T, Hoppe M, Votta L and Pusztai I 2025 *J. Plasma Phys.* **91** E78
[250] Papp G, Drevlak M, Fülöp T, Helander P and Pokol G I 2011 *Plasma Phys. Control. Fusion* **53** 095004
[251] Papp G, Drevlak M, Fülöp T and Helander P 2011 *Nucl. Fusion* **51** 043004
[252] Boozer A H 2011 *Plasma Phys. Control. Fusion* **53** 084002
[253] Smith H M, Boozer A H and Helander P 2013 *Phys. Plasmas* **20** 13255
[254] Sweeney R *et al* 2020 *J. Plasma Phys.* **86** 865860507
[255] Paz-Soldan C, Eidietis N W, Liu Y Q, Shiraki D, Boozer A H, Hollmann E M, Kim C C and Lvovskiy A 2019 *Plasma Phys. Control. Fusion* **61** 054001
[256] Lvovskiy A *et al* 2020 *Nucl. Fusion* **60** 056008
[257] Hauff T and Jenko F 2009 *Phys. Plasmas* **16** 102308
[258] Särkimäki K, Embreus O, Nardon E and Fülöp T 2020 *Nucl. Fusion* **60** 126050
[259] Svensson P, Embreus O, Newton S L, Särkimäki K, Vallhagen O and Fülöp T 2021 *J. Plasma Phys.* **87** 905870207

[260] Myra J R, Catto P J, Wootton A J, Bengtson R D and Wang P W 1992 *Phys. Fluids B* **4** 2092–7
[261] Kwon O, Diamond P H, Wagner F and Fussmann G 1988 *Nucl. Fusion* **28** 1931–43
[262] Esposito B *et al* 1996 *Plasma Phys. Control. Fusion* **38** 2035
[263] Martín-Solís J R 2021 *Phys. Plasmas* **28** 2283
[264] Jánosi D and Károlyi G 2024 *Chaos* **34** 081104
[265] Martín-Solís J R, Loarte A, Hollmann E M, Esposito B and Riccardo V (FTU, DIII-D Teams and JET EFDA Contributors) 2014 *Nucl. Fusion* **54** 083027
[266] Martín-Solís J R, Loarte A and Lehnen M 2015 *Phys. Plasmas* **22** 082503
[267] Riemann J, Smith H M and Helander P 2012 *Phys. Plasmas* **19** 012057
[268] Hollmann E *et al* 2013 *Nucl. Fusion* **53** 083004
[269] Loarte A, Riccardo V, Martin-Solís J R, Paley J, Huber A and Lehnen M 2011 *Nucl. Fusion* **51** 073004
[270] Jayakumar R, Fleischmann H and Zweben S 1993 *Phys. Lett. A* **172** 447
[271] Riccardo V (JET-EFDA-Contributors) 2003 *Plasma Phys. Control. Fusion* **45** A269
[272] Boncagni L *et al* 2013 *Fusion Eng. Des.* **88** 1109–12
[273] Eriksson L-G, Helander P, Andersson F, Anderson D and Lisak M 2004 *Phys. Rev. Lett.* **92** 205004
[274] Kiramov D I and Breizman B N 2017 *Phys. Plasmas* **24** 100702
[275] Lehnen M 2018 Private Communication
[276] Aleynikova K, Huijsmans G T and Aleynikov P 2016 *Plasma Phys. Rep.* **42** 486–94
[277] Khayrutdinov R and Lukash V 1993 *J. Comput. Phys.* **109** 193–201
[278] Jardin S, Pomphrey N and Delucia J 1986 *J. Comput. Phys.* **66** 481–507
[279] Bandyopadhyay I, Singh A, Sugihara M and Jardin S 2012 *Int. Atomic Energy Agency 24th Fusion Energy Conf.*
[280] Zhao C, Liu C, Jardin S C and Ferraro N M 2020 *Nucl. Fusion* **60** 126017
[281] Konovalov S *et al* 2016 *Int. Atomic Energy Agency 26th Fusion Energy Conf.*
[282] Aleynikov P B *et al* 2010 *37th EPS Conf. on Plasma Physics 2010* vol 1 pp 281–4
[283] Kiramov D, Lehnen M, Khayrutdinov R and Lukash V 2016 *Proc. 43rd EPS Conf. Plasma Physics* p 4
[284] Artola F J *et al* 2021 *Plasma Phys. Control. Fusion* **63** 064004
[285] Russo A 1991 *Nucl. Fusion* **31** 117
[286] Heikkinen J, Sipilä S and Pättikangas T 1993 *Comput. Phys. Commun.* **76** 215–30
[287] Guan X, Qin H and Fisch N J 2010 *Phys. Plasmas* **17** 092502
[288] Sommariva C, Nardon E, Beyer P, Hoelzl M, Huijsmans G T A and van Vugt D 2017 *Nucl. Fusion* **58** 016043
[289] Liu Y, Parks P B, Paz-Soldan C, Kim C and Lao L L 2019 *Nucl. Fusion* **59** 126021
[290] Beidler M T *et al* 2021 *Preprint: 2020 IAEA Fusion Energy Conf. (2021)* p TH/1-9
[291] McDevitt C J and Tang X-Z 2019 *Europhys. Lett.* **127** 45001
[292] McDevitt C J, Guo Z and Tang X-Z 2019 *Plasma Phys. Control. Fusion* **61** 024004
[293] Arnaud J S and McDevitt C J 2024 *Phys. Plasmas* **31** 062509
[294] McDevitt C J and Tang X 2023 *Phys. Rev. E* **108** L043201
[295] Pautasso G *et al* 2015 *Proc. 42nd EPS Conf. on Plasma Physics*
[296] Cornille B S, Beidler M T, Munaretto S, Chapman B E, Del-Castillo-Negrete D, Hurst N C, Sarff J S and Sovinec C R 2022 *Phys. Plasmas* **29** 052510
[297] Carbajal L, del Castillo-Negrete D and Martinell J J 2020 *Phys. Plasmas* **27** 032502
[298] Boozer A H and Punjabi A 2016 *Phys. Plasmas* **23** 102513
[299] Abdullaev S 2013 *Magnetic Stochasticity in Magnetically Confined Fusion Plasmas* (Springer)
[300] de Rover M, Cardozo N J L and Montvai A 1996 *Phys. Plasmas* **3** 4478–88
[301] Papp G, Drevlak M, Fülöp T and Pokol G I 2012 *Plasma Phys. Control. Fusion* **54** 125008
[302] Carbajal L and del Castillo-Negrete D 2017 *Plasma Phys. Control. Fusion* **59** 124001
[303] del Castillo-Negrete D, Carbajal L, Spong D and Izzo V 2018 *Phys. Plasmas* **25** 056104
[304] Artola F J, Lackner K, Huijsmans G T A, Hoelzl M, Nardon E and Loarte A 2020 *Phys. Plasmas* **27** 032501
[305] Jardin S, Breslau J and Ferraro N 2007 *J. Comput. Phys.* **226** 2146–74
[306] Ferraro N M *et al* 2016 *Phys. Plasmas* **23** 056114
[307] Huysmans G and Czarny O 2007 *Nucl. Fusion* **47** 659
[308] Bandaru V *et al* 2021 *Plasma Phys. Control. Fusion* **63** 035024
[309] Sommariva C *et al* 2024 *Nucl. Fusion* **64** 106050
[310] Marini C, Hollmann E M, Tang S W, Herfindal J L, Shiraki D, Wilcox R S, del-Castillo-Negrete D, Yang M, Eidietis N and Hoppe M 2024 *Nucl. Fusion* **64** 076039
[311] Helander P, Grasso D, Hastie R J and Perona A 2007 *Phys. Plasmas* **14** 122102
[312] Singh L, Borgogno D, Subba F and Grasso D 2023 *Phys. Plasmas* **30** 122114
[313] Liu S J *et al* 2026 *J. Plasma Phys.* **92** E3
[314] Nardon E, Bandaru V, Hoelzl M, Artola F J and Maget P 2023 *Phys. Plasmas* **30** 092502
[315] Singh L 2025 Impact of runaway electrons generated during disruptions on the first wall of the tokamak reactors *PhD Thesis* (available at: https://iris.polito.it/handle/11583/2996614)
[316] Liu Y, Aleynikova K, Paz-Soldan C, Aleynikov P, Lukash V and Khayrutdinov R 2022 *Nucl. Fusion* **62** 066026
[317] Vannini F *et al* 2025 *Nucl. Fusion* **65** 046006
[318] Lvovskiy A *et al* 2018 *Plasma Phys. Control. Fusion* **60** 124003
[319] Lvovskiy A *et al* 2019 *Nucl. Fusion* **59** 124004
[320] Liu C, Lvovskiy A, Paz-Soldan C, Jardin S C and Bhattacharjee A 2023 *Phys. Rev. Lett.* **131** 085102
[321] Yang M, Wang P, del-Castillo-Negrete D, Cao Y and Zhang G 2024 *SIAM J. Sci. Comput.* **46** C508–33
[322] Cathey A, Hoelzl M, Lackner K, Huijsmans G T A, Dunne M G, Wolfrum E, Pamela S J P, Orain F and Günter S 2020 *Nucl. Fusion* **60** 124007
[323] Särkimäki K, Artola J and Hoelzl M (the JOREK Team) 2022 *Nucl. Fusion* **62** 086033
[324] Bandaru V and Hoelzl M 2023 *Phys. Plasmas* **30** 092508
[325] Yuan L and Hu D 2023 *Chin. Phys. B* **32** 075208
[326] ICRU-Report- 37 1984 Stopping powers for electrons and positrons
[327] Berger M J and Seltzer S M 1970 *Phys. Rev. C* **2** 621–31

[328] Bethe H A and Ashkin J 1953 *Experimental Nuclear Physics* vol I, ed E Segre (Wiley)
[329] Carron N J 2007 *An Introduction to the Passage of Energetic Particles Through Matter* (Taylor & Francis)
[330] Seltzer S M and Berger M J 1986 *At. Data Nucl. Data tables* **35** 345–418
[331] Hubbell J H, Gimm H A and Overbo I 1980 *J. Phys. Chem. Ref. Data* **9** 1023
[332] IAEA-TECDOC-1178 2000 Handbook on photonuclear data for applications: cross-sections and spectra
[333] Fano U 1963 *Annu. Rev. Nucl. Part. Sci.* **13** 1–66
[334] Yu J H, De Temmerman G, Doerner R P, Pitts R A and van den Berg M A 2015 *Nucl. Fusion* **55** 093027
[335] Carslaw H S and Jaeger J C 1959 *Conduction Of Heat In Solids* (Oxford University Press)
[336] Dabby F and Paek U-C 1972 *IEEE J. Quantum Electron.* **8** 106–11
[337] Blackwell B F 1990 *J. Heat Transfer* **112** 567–71
[338] Behling R, Hulme C, Tolias P and Danielsson M 2025 *Med. Phys.* **52** 814–25
[339] Lockwood G J, Ruggles L E, Miller G H and Halbleib J A 1980 SAND79-0414 Report: calorimetric measurement of electron energy deposition in extended media. Theory vs experiment
[340] Gilligan J, Niemer K, Bourham M, Croessmann C, Hankins O, Tallavarjula S, Mohanti R and Orton N 1990 *J. Nucl. Mater.* **176-177** 779–85
[341] Niemer K, Gilligan J and Croessmann C 1991 *[Proc.] The 14th IEEE/NPSS Symp. Fusion Engineering* vol 1 pp 372–6
[342] Halbleib J A and Mehlhorn T A 1984 ITS: the integrated TIGER series of coupled electron/photon Monte Carlo transport codes
[343] Bolt H and Calén H 1991 *J. Nucl. Mater.* **179–181** 360–3
[344] Bartels H-W 1994 *Fus. Eng. Des.* **23** 323
[345] Brun R, *et al* 1985 The GEANT3 electromagnetic shower program and a comparison with the EGS3 code
[346] Brun R *et al* 1987 GEANT 3: user's guide Geant 3.10, Geant 3.11; rev. version (CERN)
[347] Kunugi T *et al* 1992 *Fusion Technol.* **21** 1868–72
[348] Kunugi T 1994 *Fus. Eng. Des.* **23** 329–39
[349] Nelson W R and Rogers D W 1988 *Monte Carlo Transport of Electrons and Photons* (Springer) pp 287–305
[350] Maddaluno G, Maruccia G, Merola M and Rollet S 2003 *J. Nucl. Mater.* **313–316** 651
[351] Ferrari A, Ranft J, Sala P R and Fassò A 2005 Fluka: a multi-particle transport code (program version 2005)
[352] Ward R C and Steiner D 2004 *Fusion Sci. Technol.* **45** 529–48
[353] Krawrakow I and Rogers D W O 2000 The EGSnrc code system: Monte Carlo simulation of electron and photon transport
[354] Bazylev B, Igitkhanov Y, Landman I, Pestchanyi S and Loarte A 2011 *J. Nucl. Mater.* **417** 655–8
[355] Bazylev B, Arnoux G, Brezinsek S, Igitkhanov Y, Lehnen M, Riccardo V and Kiptily V 2013 *J. Nucl. Mater.* **438** S237
[356] Sizyuk V and Hassanein A 2009 *Nucl. Fusion* **49** 095003
[357] Agostinelli S *et al* 2003 *Nucl. Instrum. Meth. Phys. Res. A* **506** 250–303
[358] Allison J *et al* 2006 *IEEE Trans. Nucl. Sci.* **53** 270–8
[359] Allison J *et al* 2016 *Nucl. Instrum. Meth. Phys. Res. A* **835** 186–225
[360] Battistoni G *et al* 2015 *Ann. Nucl. Energy* **82** 10–18
[361] Ahdida C *et al* 2022 *Front. Phys.* **9** 788253
[362] Dressel R W 1966 *Phys. Rev.* **144** 332
[363] Tabata T 1967 *Phys. Rev.* **162** 336
[364] Ratynskaia S *et al* 2026 *Plasma Phys. Control. Fusion* **68** 025024
[365] Rizzi T *et al* 2026 *Nucl. Mater. Energy* **46** 102097
[366] Hetnarski R B and Reza Eslami M 2019 *Thermal Stresses - Advanced Theory and Applications* (Springer Nature)
[367] Fung W C and Tong P 2001 *Classical and Computational Solid Mechanics* (World Scientific Publishing)
[368] Budynas R G 1999 *Advanced Strength and Applied Stress Analysis* (McGraw-Hill)
[369] Scapin M, Peroni L and Dallocchio A 2012 *J. Nucl. Mater.* **420** 463–72
[370] Scapin M, Peroni L, Boccone V and Cerutti F 2014 *Comput. Struct.* **141** 74–83
[371] Kaselouris E, Dimitriou V, Fitilis I, Skoulakis A, Koundourakis G, Clark E L, Bakarezos M, Nikolos I K, Papadogiannis N A and Tatarakis M 2017 *Nat. Commun.* **8** 1713
[372] Kaselouris E, Tamiolakis G, Fitilis I, Skoulakis A, Dimitriou V and Tatarakis M 2021 *Plasma Phys. Control. Fusion* **63** 085010
[373] Scapin M and Peroni L 2022 *Metals* **12** 670
[374] Kerley G I 2003 Equations of State for Be, Ni, W, and Au, Sandia report SAND 2003-3784, October 2003
[375] Johnson G R and Cook W H 1983 A constitutive model and data for metals subjected to large strains, high strain rates and high temperatures
[376] Zerilli F J and Armstrong R W 1987 *Proc. 7th Int. Symp. on Ballistics* (The Hague, April 1983) pp 541–7 *J. Appl. Phys.* **61** 1816–25
[377] Lennon A M and Ramesh K T 2000 *Mater. Sci. Eng.* **A276** 9–21
[378] Belytschko T, Liu W K, Moran B and Elkhodary K 2014 *Nonlinear Finite Elements for Continua and Structures* (Wiley)
[379] Hallquist J O 2006 LS-DYNA Theory Manual
[380] Song J-H, Wang H and Belytschko T 2008 *Comput. Mech.* **42** 239–50
[381] Dimitriou V, Kaselouris E, Orphanos Y, Bakarezos M, Vainos N, Tatarakis M and Papadogiannis N A 2013 *Appl. Phys. Lett.* **103** 114104
[382] Dimitriou V *et al* 2015 *Appl. Phys. A* **118** 739–48
[383] Kaselouris E, Nikolos I K, Orphanos Y, Bakarezos M, Papadogiannis N A, Tatarakis M and Dimitriou V 2016 *Int. J. Damage Mech.* **25** 42–55
[384] Apostolova T *et al* 2021 *Tools for Investigating Electronic Excitation: Experiment and Multi-Scale Modelling* (Universidad Politécnica de Madrid: Instituto de Fusión Nuclear 'Guillermo Velarde')
[385] Liu G and Liu M 2003 *Smoothed Particle Hydrodynamics: a Meshfree Particle Method* (World Scientific)
[386] Messahel R and Souli M 2013 *Comput. Model. Eng. Sci.* **96** 435–55
[387] Richter T 2017 *Lecture Notes in Computational Science and Engineering: Fluid-Structure Interactions* (Springer International Publishing)
[388] Kaselouris E *et al* 2017 *Solid State Phenom.* **261** 339
[389] Wu J-Y *et al* 2020 *Adv. Appl. Mech.* **53** 1–183
[390] Silling S A and Lehoucq R B 2010 *Adv. Appl. Mech.* **44** 73–168
[391] Madenci E and Oterkus E 2014 *Peridynamic Theory and Its Applications* (Springer)
[392] Klinkov S, Kosarev V and Rein M 2005 *Aerospace Sci. Technol.* **9** 582–91

[393] Hassani-Gangaraj M, Veysset D, Nelson K A and Schuh C A 2018 *Scr. Mater.* **145** 9–13
[394] Tolias P, De Angeli M, Ripamonti D, Ratynskaia S, Riva G, Daminelli G and De Angeli M 2023 *Fus. Eng. Des.* **195** 113938
[395] De Angeli M *et al* 2024 *Nucl. Mater. Energy* **41** 101735
[396] Eichhorn G 1976 *Planet. Space Sci.* **24** 771–81
[397] Burchell M J, Cole M J, McDonnell J A M and Zarnecki J C 1999 *Meas. Sci. Technol.* **10** 41
[398] Ratynskaia S, Castaldo C, Rypdal K, Morfill G, de Angelis U, Pericoli-Ridolfini V, Rufoloni A and Giovannozzi E 2008 *Nucl. Fusion* **48** 015006
[399] Fraile A, Dwivedi P, Bonny G and Polcar T 2022 *Nucl. Fusion* **62** 026034
[400] Veysset D, Lee J-H, Hassani M, Kooi S E, Thomas E L and Nelson K A 2021 *Appl. Phys. Rev.* **8** 011319
[401] Amani J, Oterkus E, Areias P, Zi G, Nguyen-Thoi T and Rabczuk T 2016 *Int. J. Impact Eng.* **87** 83
[402] Ren B and Song J 2024 *Surf. Coat. Technol.* **493** 131257
[403] Libersky L D, Randles P W, Carney T C and Dickinson D L 1997 *Int. J. Impact Eng.* **20** 525–32
[404] Remington T P, Owen J, Nakamura A, Miller P and Bruck Syal M 2020 *Earth Space Sci.* **7** e2018EA000474
[405] Artola F *et al* 2024 *Thermal Loads in Unmitigated Disruptions 44th ITPA MDC Meeting*
[406] TFR 1980 *J. Nucl. Mater.* **93–94** 203–9
[407] Barnes C, Stavely J and Strachan J 1981 *Nucl. Fusion* **21** 1469
[408] Sukegawa A M, Okuno K and Tanaka S 2018 *Fusion Eng. Des.* **136** 1653–7
[409] Rising M E *et al* 2023 MCNP® Code Version 6.3.0 Release Notes *Technical Report* LA-UR-22-33103, (Rev. 1 Los Alamos National Laboratory)
[410] Hugot F-X, Jinaphanh A, Jouanne C, Larmier C, Lee Y K, Mancusi D, Petit O, Visonneau T and Zoia A 2024 *EPJ - Nucl. Sci. Technol.* **10** 17
[411] Ataeisereht L, Abdi M R, Pourshahab B and Rasouli C 2023 *Nat. Sci. Rep.* **13** 7
[412] Valenza D, Iida H, Plenteda R and Santoro R T 2001 *Fusion Eng. Des.* **55** 411–8
[413] Chen Y and Fischer U 2002 *Fusion Eng. Des.* **63-64** 107–14
[414] Polovoi A R *et al* 2020 *Int. Atomic Energy Agency 28th Fusion Energy Conf.*
[415] Causa F, Buratti P, Esposito B, Pucella G, Giovannozzi E, Jakubowski L, Malinowski K, Rabinski M, Sadowski M J and Zebrowski J 2015 *Nucl. Fusion* **55** 123021
[416] Ericsson G 2019 *J. Fusion Energy* **38** 330–55
[417] Štancar Z *et al* 2021 *Nucl. Fusion* **61** 126030
[418] Chadwick M *et al* 2011 *Nucl. Data Sheets* **112** 2887–996
[419] Brown D *et al* 2018 *Nucl. Data Sheets* **148** 1–142
[420] Iwamoto O *et al* 2023 *J. Nucl. Sci. Technol.* **60** 1–60
[421] Kawano T *et al* 2020 *Nucl. Data Sheets* **163** 109–62
[422] Koning A, Rochman D, Sublet J-C, Dzysiuk N, Fleming M and van der Marck S 2019 *Nucl. Data Sheets* **155** 1–55
[423] Tuyet T K, Jinaphanh A, Jouanne C, Gérardin F, Lemaire S and Zoia A 2024 *Nucl. Sci. Eng.* **198** 319–35
[424] Sauvan P, Juárez R, Pedroche G, Alguacil J, Catalan J P, Ogando F and Sanz J 2020 *Fusion Eng. Des.* **151** 111399
[425] Villari R, Fischer U, Moro F, Pereslavtsev P, Petrizzi L, Podda S and Serikov A 2014 *Fusion Eng. Des.* **89** 2083–7
[426] Carnevale D *et al* 2018 *Plasma Phys. Control. Fusion* **61** 014036
[427] Jachmich S 2024 *Proc. 50th EPS Conf. on Plasma Physics, (8 July–12 July)*
[428] Vallhagen O, Embreus O, Pusztai I, Hesslow L and Fülöp T 2020 *J. Plasma Phys.* **86** 475860401
[429] Artola F, Loarte A, Hoelzl M, Lehnen M and Schwarz N (JOREK Team) 2022 *Nucl. Fusion* **62** 056023
[430] Nardon E, Matsuyama A, Hu D and Wieschollek F 2021 *Nucl. Fusion* **62** 026003
[431] Nardon E, Hu D, Hoelzl M and Bonfiglio D 2020 *Nucl. Fusion* **60** 126040
[432] Vallhagen O, Pusztai I, Hoppe M, Newton S L and Fülöp T 2022 *Nucl. Fusion* **62** 112004
[433] Lukash V *et al* 2013 *40th EPS Conf. on Plasma Physics* pp 5–167
[434] Sheikh U *et al* 2024 *Third IAEA Technical Meeting on Plasma Disruptions and Their Mitigation, (3 September–6 September)*
[435] Aumeunier M-H *et al* 2024 *Nucl. Fusion* **64** 086044
[436] Pandya S P, Core L, Barnsley R, Rosato J, Reichle R, Lehnen M, Bertalot L and Walsh M 2018 *Phys. Scr.* **93** 115601
[437] Patel A, Pandya S P, Shevelev A E, Khilkevitch E M, Iliasova M, O'Connor R, Tieulent R, Barnsley R and Mokeev A N 2023 *Phys. Scr.* **98** 085604
[438] Nocente M *et al* 2017 *Nucl. Fusion* **57** 076016
[439] Esposito B *et al* 2022 *J. Fusion Energy* **41** 22
[440] Lehnen M 2023 Physics basis and technology development for the iter disruption mitigation system, 29th IAEA Fusion Energy Conference (FEC 2023)
[441] Luce T *et al* 2021 *28th IAEA Fusion Energy Conf.* p –TECH
[442] Helander P, Geiger J and Maaßberg H 2011 *Phys. Plasmas* **18** 092505
[443] Garnier D *et al* 2006 *Fusion Eng. Des.* **81** 2371–80
[444] Zhuang G *et al* 2019 *Nucl. Fusion* **59** 112010
[445] Tang T *et al* 2021 *Nucl. Fusion* **61** 076003
[446] Siccinio M, Graves J P, Kembleton R, Lux H, Maviglia F, Morris A W, Morris J and Zohm H 2022 *Fusion Eng. Des.* **176** 113047
[447] Maviglia F *et al* 2022 *Fusion Eng. Des.* **178** 113125
[448] Martín-Solís J R 2017 *Report on 2017 TS activities on Runaway electrons: Modelling of runaway electron generation and termination in DEMO disruptions* Report IDM reference No. EFDA_D_2N49CW
[449] Martín-Solís J R 2018 *2018 TS activities on Runaway electrons: Modelling (0D and 1D) of runaway electron formation in DEMO disruptions* Report IDM reference No. EFDA_D_2NFCXH
[450] Pautasso G *et al* 2019 *46th EPS Conf. on Plasma Physics* p oster 4.1045
[451] You J *et al* 2022 *Fusion Eng. Des.* **174** 112988
[452] Richiusa M *et al* 2024 *Fusion Eng. Des.* **202** 114329
[453] Richiusa M, Lyytinen J, Sinha A and Spagnuolo G 2025 *Fusion Eng. Des.* **214** 114890
[454] Ramogida G *et al* 2015 *Fusion Eng. Des.* **96-97** 348–52
[455] Lombroni R, Giorgetti F, Calabrò G, Fanelli P and Ramogida G 2021 *Fusion Eng. Des.* **170** 112697
[456] Firdaouss M, Riccardo V, Martin V, Arnoux G and Reux C 2013 *J. Nucl. Mater.* **438** S536–9
[457] Arter W, Surrey E and King D B 2015 *IEEE Trans. Plasma Sci.* **43** 3323–31

[458] Maddaluno G 2019 *Use of the FLUKA code for the evaluation of volumetric loads due to Res (Runaway Electrons)* Report IDM reference No. EFDA_D_123456
[459] Pokol G 2025 *DREAM simulations of runaway electron distributions in EU-DEMO disruptions* Report_DEMO_kinetic_DREAM.docx, EK-FPL/2025-41
[460] Emanuelli E, Vannini F, Hoelzl M *et al* 2026 *Fusion Eng. Des.* **223** 115588
[461] Fil A, Henden L, Newton S, Hoppe M and Vallhagen O 2024 *Nucl. Fusion* **64** 106049
[462] Hartwig Z S *et al* 2024 *IEEE Trans. Appl. Supercond.* **34** 1–16
[463] Creely A J *et al* 2020 *J. Plasma Phys.* **86** 865860502
[464] Eidietis N *et al* 2015 *Nucl. Fusion* **55** 063030
[465] Tinguely R A *et al* 2021 *Nucl. Fusion* **61** 124003
[466] Ekmark I *et al* 2025 Runaway electron generation in disruptions mitigated by deuterium and noble gas injection in SPARC *J Plasma Phys.* **91** E82
[467] Tinguely R A *et al* 2023 *Plasma Phys. Control. Fusion* **65** 034002
[468] Feyrer A, Looby T, Sweeney R and Tinguely R 2024 *Bull. Am. Phys. Soc. 66th Annual Meeting of the APS Division of Plasma Physics (Atlanta, Georgia, USA 7–11 October 2024)* NP12.00112 : Implementation of a runaway electron module in HEAT
[469] Looby T *et al* 2022 *Fusion Sci. Technol.* **78** 10–27
[470] Reinke M L *et al* 2024 *Rev. Sci. Instrum.* **95** 103518
[471] Commonwealth Fusion Systems 2024 Commonwealth fusion systems to build world's first commercial fusion power plant in Virginia (available at: https://cfs.energy/news-and-media/commonwealth-fusion-systems-to-build-worlds-first-commercial-fusion-power-plant-in-virginia)
[472] Hillesheim J *et al* 2024 *Bull. Am. Phys. Soc. 66th Annual Meeting of the APS Division of Plasma Physics* (Atlanta, Georgia, USA, 7–11 October 2024) TO06.00002 : ARC physics basis progress
[473] Hillesheim J *et al* 2025 Overview of the physics basis for the ARC fusion power plant *J. Plasma Phys.*, submitted
[474] Balboa I *et al* 2023 *Plasma Phys. Control. Fusion* **65** 064005
[475] Losada U *et al* 2020 *Nucl. Mater. Energy* **25** 100837
[476] Sieglin B, Faitsch M, Herrmann A, Brucker B, Eich T, Kammerloher L and Martinov S 2015 *Rev. Sci. Instrum.* **86** 113502
[477] Courtois X *et al* 2014 *Fusion Eng. Des.* **89** 2472–6
[478] Jaspers R, Grewe T, Finken K H, Krämer-Flecken A, Lopes Cardozo N J, Mank G and Waidmann G 1995 *J. Nucl. Mater.* **220–222** 682–7
[479] Wongrach K, Finken K H, Abdullaev S S, Willi O, Zeng L and Xu Y 2015 *Nucl. Fusion* **55** 053008
[480] Pucella G *et al* 2019 *Nucl. Fusion* **59** 112015
[481] Marocco D, Esposito B, Riva M, Belli F, Podda S and Panaccione L 2015 *Fusion Eng. Des.* **96–97** 852–5
[482] Chen Z Y *et al* 2006 *Rev. Sci. Instrum.* **77** 013502
[483] Purohit S *et al* 2020 *J. Instrum.* **15** 08015